Design and Implementation of a Sargassum Floating Offshore Barrier for Coastal Protection

Multidisciplinary Project (CEGM3000)

Jaap van den Berg, Stephan van Eps, Bram Posma, Otto Schultze, Justus van der Wulp

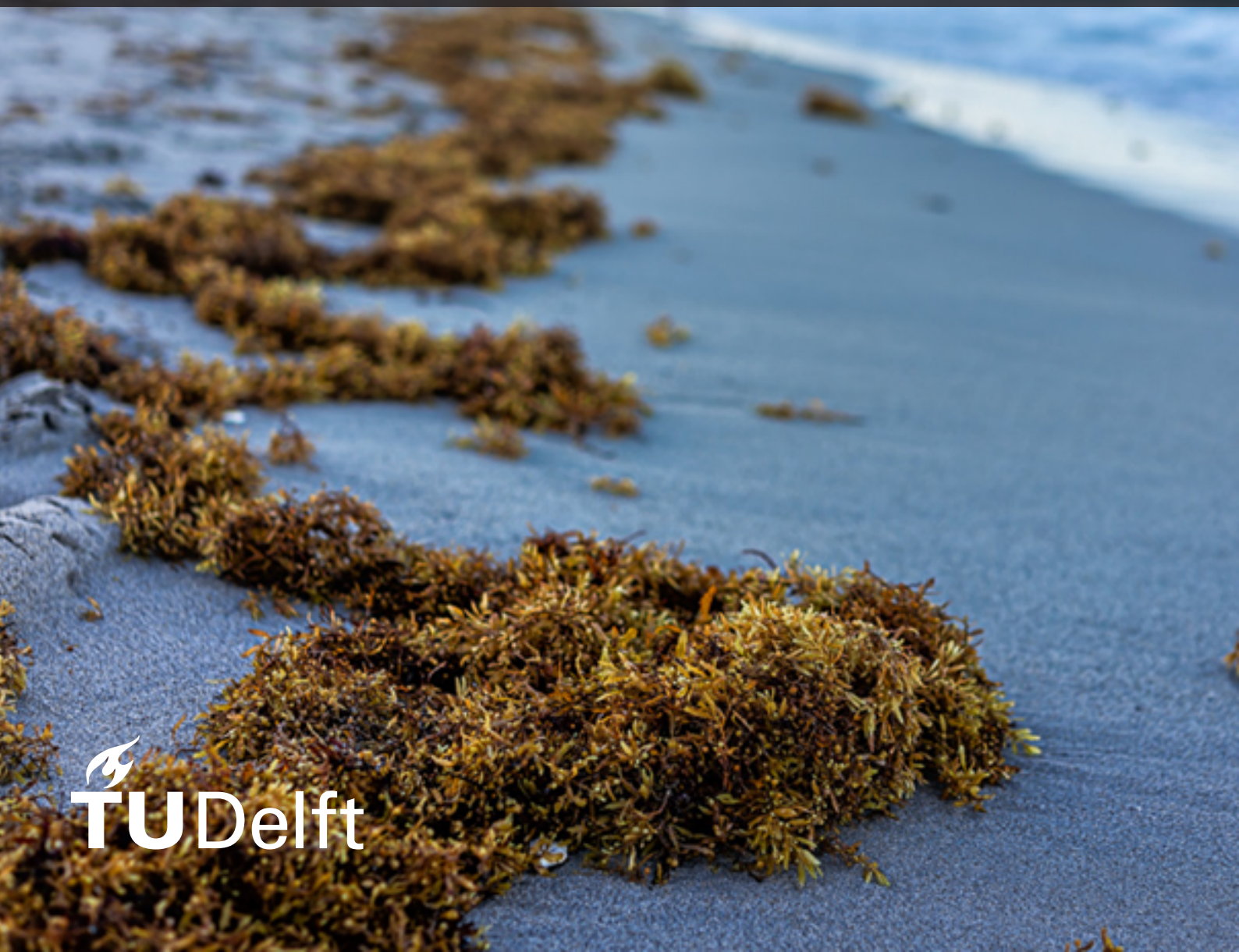

TU Delft

Design and Implementation of a Sargassum Floating Offshore Barrier for Coastal Protection

by

Jaap van den Berg, Stephan van Eps, Bram Posma, Otto Schultze, Justus van der Wulp

Group: MP365

Student Number	Student Name
4753801	Jaap van den Berg
4844343	Stephan van Eps
4849671	Bram Posma
4897986	Otto Schultze
5009790	Justus van der Wulp

Instructors: dr. J.A. Garcia, ir. J. Hoving, dr. I.M. Tapia,
Project Duration: September 2024, November 2024

Cover: [13]

Preface

When we started this research, we learned about the ecological impact of sargassum arrivals to the Yucatán coastal area. We were excited to contribute to research to find a solution to this problem. However, during our field trip, we realized our good intentions might not help the local Yucatecan people. Big hotels can afford barriers to protect their beaches, but public beaches remain unprotected. Thankfully, we spoke to many people who shared their insights. They explained why public research on sargassum barriers is important. This motivated us throughout the project.

First, we want to thank Ismael Mariño Tapia for being a great professor and an even better host and friend. When we arrived in Merida, we were warmly welcomed, shown around the campus and even took us to a cenote. We could not wish for a warmer welcome. We also want to thank Jaime Arriaga Garcia for being our supervisor from the TU Delft and are grateful for letting us stay in his house near the university. His support didn't stop there. When we wanted to climb the Nevado de Toluca volcano, we were invited to stay with his parents in Toluca. Without Jaime, this whole project would not be possible and we would not have such a majestic experience of Mexico. We want to thank Jeroen Hoving for being the second supervisor of this project and assessing our report and presentation. And a big thank you to Deltares for providing us with Delft3D, which was essential for our project.

This project has helped us develop both research and personal skills. Working as a diverse team, each member shared their unique expertise, allowing us to learn from each other's knowledge, values, and beliefs. It pushed us to adapt and better understand each other's challenges, which we then helped to solve together. Living and working closely in Mexico for 10 weeks was an unforgettable experience. Alongside professional growth, we also became close friends, creating everlasting friendships. This unique way of working and living together has been an unforgettable experience.

Moving to a country none of us had visited before gave us the unique opportunity to immerse ourselves in Mexican culture. From day one, we were warmly welcomed by the Yucatecan people, whose kindness and hospitality made us feel at home immediately. We quickly grew to love food, the laid-back mentality, and the genuine good intentions of everyone we encountered, making our time in Mexico even more memorable.

Lastly, we want to thank Raul for putting a smile on our faces all the early mornings.

Abstract

The Mexican government and hotel industry have implemented various methods to remove sargassum from the coast, including mechanical removal and floating barriers. However, the barriers are often designed without considering relevant Metocean data or calculations, making them potentially ineffective. This study investigates the optimal placement and design parameters for floating barriers, focusing on redirecting sargassum offshore along highly impacted regions of the Yucatán coast, specifically in Puerto Morelos. The research integrates hydrodynamic analysis, barrier designs, and structural modelling to identify critical factors influencing barrier performance. The aim of this research is to establish a comprehensive framework for positioning sargassum-catching barriers along coastlines, adaptable to any location.

The hydrodynamic analysis reveals that barrier placement and orientation are crucial for effective sargassum redirection. Results highlight the southern and northern reefs of the reef lagoon of Puerto Morelos as optimal locations for barrier endpoints, enhancing natural flushing potential while minimising coastal accumulation. Design, structural, and material analyses favour a Type II barrier design with an indirect anchoring system, which provides durability with minimal ecological impact. The preferred materials, including HDPE, PVC, and galvanized steel cables, were selected for their resilience in marine conditions.

A finite element model was employed to analyse internal forces within the barrier and its mooring system. Assumptions regarding barrier cross-sectional shape, drag coefficient, and mooring lines were validated within theoretical expectations, though resource limitations prevented empirical testing. Ultimately, this framework serves as a foundation for future improvements and field applications, with recommendations for further empirical validation to refine design parameters and enhance overall barrier performance.

Nomenclature

Abbreviations

Abbreviation	Definition
CDF	Cumulative Distribution Function
EVA	Extreme Value Analysis
FEM	Finite Element Method
HDPE	High-Density Polyethylene
LDPE	Low-Density Polyethylene
LLDPE	Linear Low-Density Polyethylene
MHKiT	Marine and Hydrokinetic Toolkit
MRL	Mean Residual Time
MSE	Mean Squared Error
PDF	Probability Density Function
PE	Polyethene
PMMA	Polymethyl methacrylate
POT	Peak Over Threshold
PP	Polypropylene
pPVC	plasticised PVC
PU	Polyutherane
PVC	Polyvinylchloride
SAMMO	Servicio Académico de Monitoreo Meteorológico y Oceanográfico
TOI	Time Of Interest
uPVC	unmodified PVC
UV	Ultraviolet

Symbols

Symbol	Definition	Unit
A	Cross-sectional area	$[\mathrm{m}^2]$
$a_n(f)$	Amplitude for the n-th frequency component	$[\mathrm{m}]$
C	Damping coefficient	$0.01 \cdot EA$
C_d	Drag coefficient	[-]
C_I	Inertia coefficient, $C_I = 1 + C_m$	[-]
C_m	Mass coefficient	[-]
C_u	Damping factor in longitudinal direction	$[\mathrm{kg/s \cdot m}]$
C_v	Damping factor in transverse direction	$[\mathrm{kg/s \cdot m}]$
D	Diameter of structure or height of submerged barrier	$[\mathrm{m}]$
D_{b1o}	Outside diameter of buoys of barrier	$[\mathrm{m}]$
D_{b1i}	Inside diameter of buoys of barrier	$[\mathrm{m}]$
D_{b2o}	Outside diameter of anchoring buoys	$[\mathrm{m}]$
D_{b2i}	Inside diameter of anchoring buoys	$[\mathrm{m}]$
D_{bo}	Outside diameter buoy	$[\mathrm{m}]$
D_{bi}	Inside diameter buoy	$[\mathrm{m}]$
D_{cable}	Diameter of cable in barrier	$[\mathrm{cm}]$
D_m	Diameter of mooring line	$[\mathrm{m}]$
$D_{mooring}$	Diameter of mooring line	$[\mathrm{cm}]$
D_t	Diameter of the tension cables	$[\mathrm{m}]$
D_{upper}	Height of barrier above water surface	$[\mathrm{m}]$
d	Water depth	$[\mathrm{m}]$
d_0	Average still-water depth	$[\mathrm{m}]$
d_s	Depth to which sargassum extends	$[\mathrm{m}]$
dt	Time step in solver	$[\mathrm{s}]$
E	Young's modulus	$[\mathrm{N/m}^2]$

Symbol	Definition	Unit
EA	Axial stiffness	[N]
$F_{AM}(t)$	Inertia force (added mass)	[N]
$F_D(t)$	Drag force due to viscous effects	[N]
F_G, net	Self-weight of net structure	[N]
F_G, t	Self-weight of tension cables	[N]
F_h	Maximal tension in mooring lines	[N]
$F_S(t)$	Sargassum force	[N/m]
f_n	Frequency of n-th component	[Hz]
$f_u(x,t)$	External force in longitudinal direction	[N/m]
$f_v(x,t)$	External force in transverse direction	[N/m]
g	Gravitational constant	[m/s^2]
H_{max}	Maximal water level	[m]
H_s	Significant wave height	[m]
k_n	Wave number corresponding to f_n	[-]
$k_geometry$	Stiffness mooring lines from geometry	[N/m]
$k_material$	Stiffness mooring lines from material	[N/m]
L	Length barrier segment	[m]
l	Distance between mooring lines	[m]
l_m	Maximal length of mooring lines	[m]
m_s	Mass of sargassum	[kg/m^3]
N	Newton	[kg $\cdot$ m/s^2]
n	Number of buoys between mooring lines	[-]
ns	Number of time steps	[-]
s	Distance between buoys	[m]
$S(f)$	Energy per unit frequency	[m^2/Hz]
$S_n(f)$	Spectral density	[m^2/Hz]
T	Tension	[N]
T_p	Peak wave period	[s]
t_s	Thickness of accumulated sargassum	[m]
T_z	Zero crossing period	[s] u
Wave particle velocity	[m/s]	
u_{wind}	Wind magnitude	[m/s]
$u(x,t)$	Longitudinal displacement	[m]
U	Current speed	[m/s]
V_b	Volume of buoy material	[m^3]
V_p	Volume of polymer in buoy	[m^3]
v	Offset in y-direction	[m]
$v(x,t)$	Transverse displacement	[m]
X	Horizontal distance between anchoring points	[m]
$\dot{u}(t)$	Wave-induced acceleration	[m/s^2]
Δf	Frequency resolution	[Hz]
$\eta(t,x)$	Wave elevation	[m]
γ_b	Breaking parameter	[-]
ϕ_n	Phase shift, randomised for initial wave position	[rad]
ρ	Density	[kg/m^3]
ρ_b	Density of buoy material	[kg/m^3]
ρ_m	Density of mooring line	[kg/m^3]
ρ_{net}	Density of net structure	[kg/m^3]
ρ_p	Density of polymer in buoy	[kg/m^3]
ρ_s	Density of sargassum	[kg/m^3]
ρ_t	Density of tension cables	[kg/m^3]
ρ_w	Density of seawater	[kg/m^3]
ω_n	Angular frequency, $\omega_n = 2\pi f_n$	[rad/s]

List of Figures

List of Tables

Contents

1 Introduction

A significant population of algae, known as *sargassum* spp. (sargassum), thrives off the coast of Brazil. Since 2011, the amount of these sargassum mats increased significantly in the North Atlantic equatorial recirculation region. These algae are carried by ocean currents through the Caribbean Sea and eventually accumulate on the beaches of the Yucatán Peninsula, as depicted Figure 1.1. These algae deplete oxygen and block sunlight in the water, leading to the partial or total mortality of near-shore corals and seagrass meadows. The recovery of these impacted corals and seagrass meadows can take years or even decades. In cases of massive sargassum influxes, these changes could become permanent. This also results in a decrease in the local fish population [67]. Additionally, the influx of sargassum diminishes the appeal of Mexican beaches for tourism. This poses a considerable challenge for the inhabitants of Yucatán, as their livelihoods heavily rely on fishing and tourism [40].

Figure 1.1: Sargassum accumulation at the Yucatán Peninsula coastline (Mexico).[71]

1.1. Problem statement

The Mexican government and the hotel industry have begun implementing various methods to remove sargassum from the coast through trial and error. One approach involves mechanically removing sargassum from the beaches, though this is labour-intensive and results in the loss of valuable sand. Another method is deploying floating barriers in the ocean to capture or redirect sargassum before it reaches the shore. However, these barriers are often designed without considering relevant Metocean data or calculations, making them potentially ineffective.

To address this, it is essential to study the effects of varying wave forces, ocean currents, and sargassum behaviour in open waters to determine the optimal barrier placement and design. The goal of this research is to identify the critical factors for developing an effective model to simulate the behaviour of a floating sargassum barrier, both hydrodynamically and structurally, to improve the current barriers. This should help local governments, NGOs, and companies realising the construction of a barrier more easily.

The scope of this research does not include designing a barrier that captures all incoming sargassum along the Yucatán coast. The barriers currently in use are no match for the tremendous volumes of incoming sargassum and are mostly installed in front of high-end hotels that can afford them. Designing a barrier that extends across the entire Yucatán peninsula is neither realistic nor financially feasible. Therefore, the focus is on specific regions that are highly vulnerable to the negative effects of sargassum.

1.2. Approach

For this project, Puerto Morelos has been chosen as the initial focus area for developing the model. This location has been heavily impacted by the arrival and beaching of sargassum in recent years, making it a well-studied site for such phenomena.

To achieve the goal of the project, the work is divided into several key phases:

1. **Hydrodynamic flow analysis:** The first step involves analysing the hydrodynamic flow conditions in Puerto Morelos. This analysis is essential for determining the optimal position of the barrier and understanding how trapped sargassum behaves. The results help to identify the best location for the barrier and determine the hydrodynamic conditions at the barrier.

2. **Barrier design research:** Once the optimal position is identified, the next phase focuses on researching the most effective design for a sargassum barrier. This design research, combined with environmental data and data from the hydrodynamic flow analysis, provides the necessary input for the structural model.

3. **Structural modelling:** The final phase involves developing a structural model to calculate the forces acting on the barrier. Using the environmental conditions and design parameters, the model gives insights into the stresses within the barrier.

The project results in a model-based solution for a floating sargassum barrier that gives insight into the stresses that occur in the structure due to the conditions at Puerto Morelos.

1.3. Research questions

To successfully implement the approach outlined in Section 1.2, each phase addresses specific research questions. These questions are detailed in the following subsections.

1.3.1. Hydrodynamic flow analysis

The main research question for the hydrodynamic flow analysis phase is:

- How does the position of the floating barrier influence the movement of sargassum at the coast of Puerto Morelos?

To address this question, the following sub-questions are explored:

- How does sargassum behave under the existing flow conditions in the bay of Puerto Morelos?
- What is the optimal position and shape of a floating sargassum barrier along the coast of Puerto Morelos, based on sargassum flow conditions?
- How will the barrier affect the movement of sargassum within the Puerto Morelos reef lagoon?

1.3.2. Barrier design research

The main research question for the barrier design research phase is:

- How can a floating barrier be optimally designed and constructed to effectively capture sargassum alongside the Puerto Morelos coast while minimising environmental impact?

To address this question, the following sub-questions are explored:

- What types of barriers are currently in use, and which type would be most suitable for Puerto Morelos?
- What are the materials used for constructing a floating barrier that can withstand challenging marine conditions, such as saltwater and UV exposure?
- What additional practical considerations are important for designing an effective floating sargassum barrier tailored to the specific conditions at Puerto Morelos?

1.3.3. Structural modelling

The main research question for the structural model is:

- How can a general structural model be developed and implemented for a floating sargassum-catching barrier?

To address this question, the following sub-questions are answered.

- How should the model be defined?
- What are the relevant input variables?
- What are the relevant boundary conditions?
- What are the relevant design criteria that need to be determined?
- How is the model implemented for the Puerto Morelos situation?
- What are the resulting stresses in the barrier and its mooring lines?

1.4. Structure of the report

First, the hydrodynamic model and its settings and methodology are introduced in Chapter 2. Next, a hydrodynamic flow analysis is conducted in Chapter 3, required to find the optimal barrier position. Chapter 4 outlines the key factors influencing the performance of existing barriers. By analysing these factors, this chapter provides a framework for designing a floating barrier suited to the conditions at Puerto Morelos.Chapter 5 introduces the structural model and provides a detailed explanation of the process for determining the forces acting on the barrier. In Chapter 6, the model is implemented using input parameters from Chapter 3 and Chapter 4, with the resulting stresses and unity checks presented. Chapter 7 goes into detail about certain unexpected results from the structural model. Then, in Chapter 8, the validation of the results and the limitations of this study are discussed. Finally, Chapter 9 concludes the report, and Chapter 10 provides suggestions for practical implementations, as well as recommendations for further research.

2
Hydrodynamic model settings and methodology

This chapter outlines the method used to model flow, sargassum displacements and the barrier within the reef lagoon. The software used for modelling these systems is Delft3D. An in-depth analysis is provided of the settings used for the simulation in Delft3D and the relevant conditions for the flow models are explained. First, in Section 2.1 the geographic location is demonstrated with an explanation of why this is the chosen research area for this project. For the design of an effective floating barrier at this reef lagoon site, the modelling scope has been narrowed down to five hydrodynamic conditions. In Section 2.2 the most significant conditions are discussed and applied to the model. Section 2.3 explains how sargassum is modelled in Delft3D, based on its physical properties. Finally, Section 2.4 elaborates on how the floating barrier is modelled in Delft3D. Once the model is defined, the arrival of sargassum and the influence of flushing is analysed in Chapter 3. The analysis in the next chapter answers the research questions about hydrodynamic flow, modelled with the settings described in this chapter.

2.1. Geographic location and grid extent

The research area stretches from the south of Puerto Morelos up to Caracol (8.5 x 6.4 km). The area contains large parts of the Puerto Morelos Reef National Park. The corresponding bathymetry is shown in Figure 2.1 (I). The coordinates of the edges of the grid are provided in Figure 2.1 (II). The southern boundary of the grid contains part of the south channel. The northern boundary is set just beyond a large opening in the reef called Boca Grande. This opening plays a key role in the flow and flushing within the area. Boca Grande and the south channel are marked in Figure 2.1 (I). These openings allow water exchange between the lagoon and the open sea, influencing the hydrodynamic conditions by facilitating the inflow of ocean currents and promoting the water flushing within the lagoon.

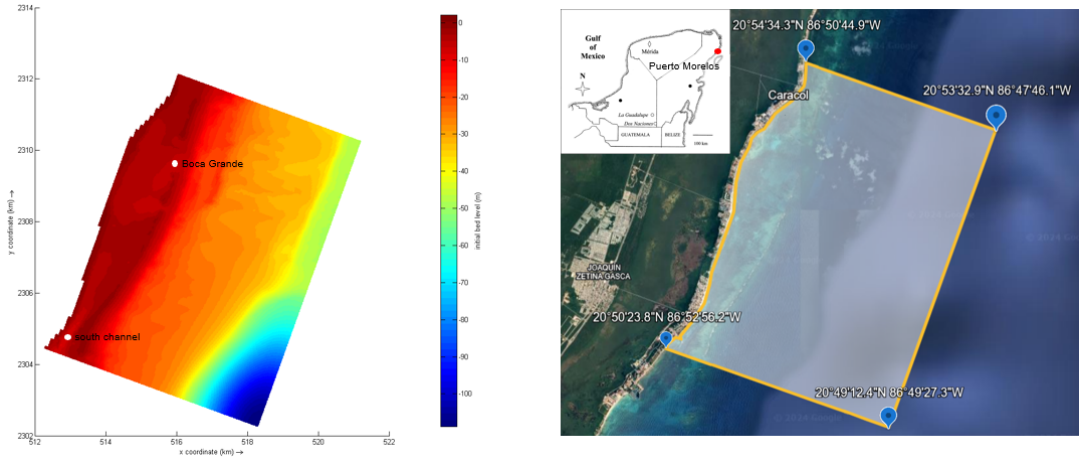

Figure 2.1: The bathymetry of the research area (I), and the corresponding aerial view of the location of Puerto Morelos, Yucatán (II).[30]

The grid resolution has been optimised to ensure an accurate representation of these hydrodynamic processes while maintaining computational efficiency. The resolution and timestep are set to provide a Courant number below 10, which is essential for numerical stability in the model. For the used grid, the maximum Courant number is 8.7 for a timestep of dt = 3 s and thus sufficient. A lower Courant number ensures that the time step is sufficiently small relative to the grid spacing, preventing numerical errors and ensuring accurate flow simulations [41]. Reducing the spatial extent of the model in this way helps to save computational time while ensuring that the key flow dynamics are still represented. Grid resolution and dimensions are defined in Table 2.1.

Table 2.1: Grid resolution and timestep in Delft3D.

M-direction	N-direction	timestep
233	309	3 s
8527 m	6416 m	

2.2. Hydrodynamic conditions

The hydrodynamic conditions serve as the input for the Delft3D model, providing the necessary boundary conditions for the simulation. Waves, wind and tides are identified as the key parameters influencing the system. These parameters differ between the conditions, creating differences in flow and wave heights. For the Puerto Morelos case, five distinct hydrodynamic conditions are considered relevant. The first three relate to the varying arrival conditions of sargassum, while winter conditions are analysed separately due to the increased frequency of northerly storms during this season. Finally, an extreme value analysis (EVA) is conducted on data from the past ten years to identify conditions that would generate the highest forces on the floating barrier. Additionally, due to the geostrophic response to the current variability along the Yucatán coast, seawater levels fluctuate throughout the year. The methodology for selecting the water level input, influenced by tidal effects and geostrophic phenomena, is discussed in Section 2.2.4. Table 2.2 provides an overview of the five hydrodynamic conditions, including the representative tidal range.

2.2.1. Arrival based conditions

In 2021, Jantien Rutten et al. published research on the beaching and natural removal dynamics of sargassum in the Puerto Morelos reef lagoon. [61] This research analysed the arrival of sargassum along with the hydrodynamic conditions using a 5.2-year data set. The results, as shown in Figure Figure 2.2, present the wind and wave conditions related to the arrival of sargassum. The arrivals are distinguished into three different classes: small, medium and large. These classifications are based on visual estimations of the size and number of the sargassum mats. The first three design conditions for this project are derived from the results of this research. The dominant significant wave height, wave direction, wind speed and direction for classes 1 to 3 are used to investigate the flow conditions within the reef lagoon during periods of high sargassum arrival intensity. Peak arrivals were found to occur in July during the study period. The conditions are specified in Table 2.2.

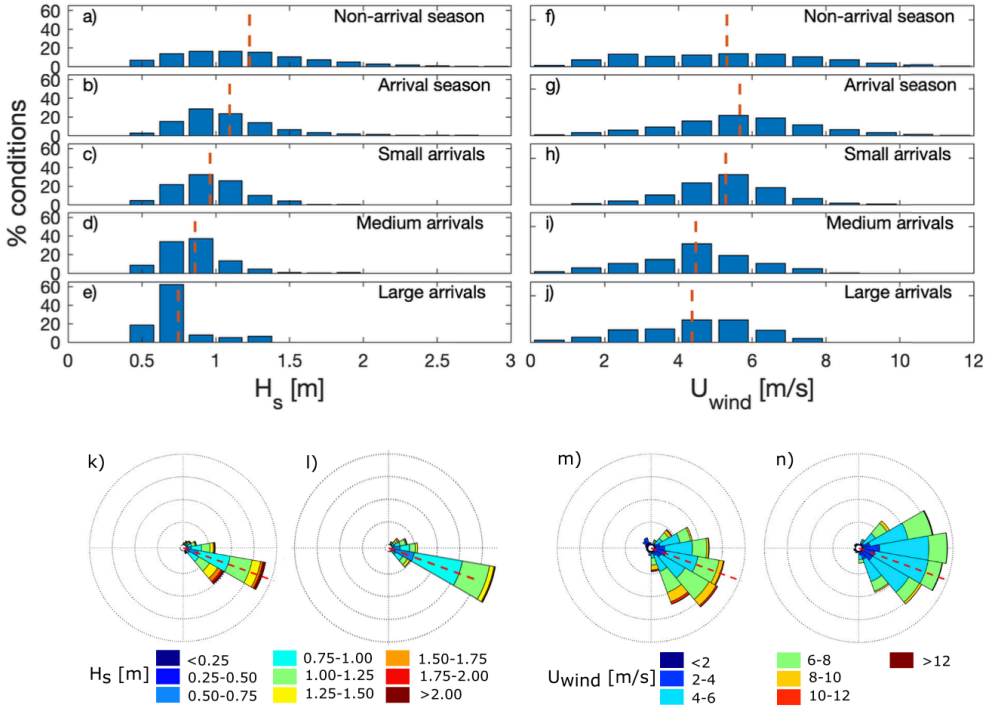

Figure 2.2: Research results for the three distinct arrival conditions of sargassum at Puerto Morelos (September 2015 – November 2020).[61]

2.2.2. Winter storm condition

Furthermore, time series analyses of sargassum beaching events revealed different periods of maximum sargassum coverage, with notable peaks from July to October 2018 and others in January and February 2019 [69]. To gain a broad understanding of how flow conditions differ between summer and winter times, average wave and wind conditions from January to February are also used as model inputs. This approach allows for modelling sargassum arrival behaviour during winter conditions, to investigate the flushing behaviour of the reef during these winter conditions. In Figure 2.3, only the wave rose is shown based on a 10-year time series including January and February data. The time series is further described in Section 2.2.3. From this result, it can be seen that the average wave direction is from the east, just as conditions 1 to 3. However, to investigate how the reef circulation behaves during northern conditions, which happens primarily from November to February during stormy conditions [59], only the values with north/north-east (0°- 45°) direction are considered, as demonstrated in Figure 2.4. The mean values of the significant wave height H_s and wind magnitude u_{wind} are used as model input. The results are given in Table 2.2. It is interesting to observe that waves coming from the northern direction exhibit a shorter peak period. This can be explained by

the local influence of wind on these waves, in contrast to the eastern waves, which display a swell wave character due to their distant origin from the Caribbean.

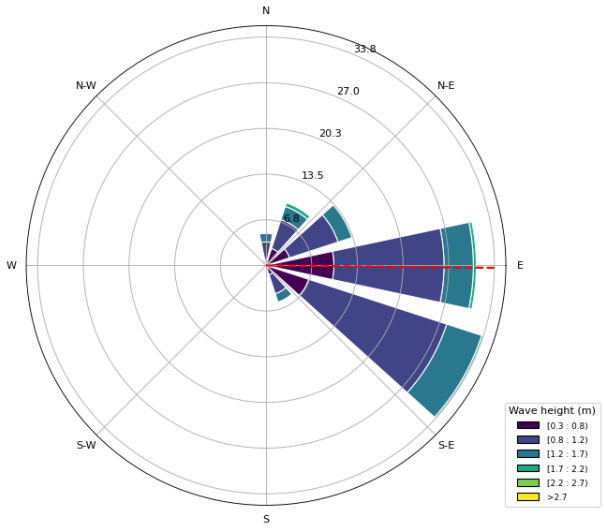

Figure 2.3: Wave rose based on all January and February data from a 10-year time series at Puerto Morelos.[1]

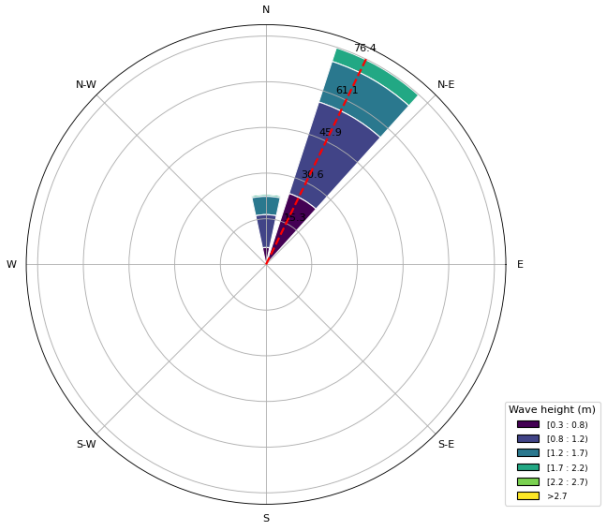

Figure 2.4: Wave rose based on all NE-directed data from November to February from a 10-year time series at Puerto Morelos.[1]

2.2.3. Extreme value condition

Lastly, it is crucial to determine the flow conditions during extreme weather events. The barrier must be designed to withstand storm conditions, especially since the Yucatán region is prone to storms and hurricanes. To achieve this, an EVA is conducted based on a 10-year dataset (2014 to 2023) from the nearest node (21.0°N, 86.5°W) of the ERA5 hindcast.[1] Onsite wind speed and wind direction data, with 4-hour resolution, is also obtained from Copernicus. The results are shown in Figure 2.5 and Figure 2.6. The wind and wave conditions derived from the EVA represent storm conditions.

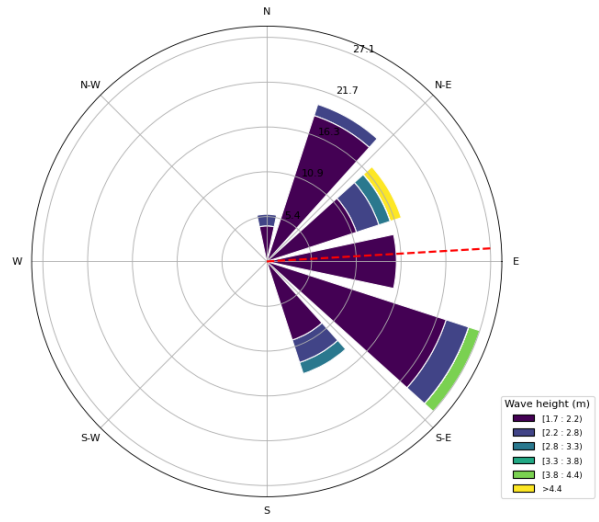

Figure 2.5: Wave rose of the 10-year time series at Puerto Morelos.[1]

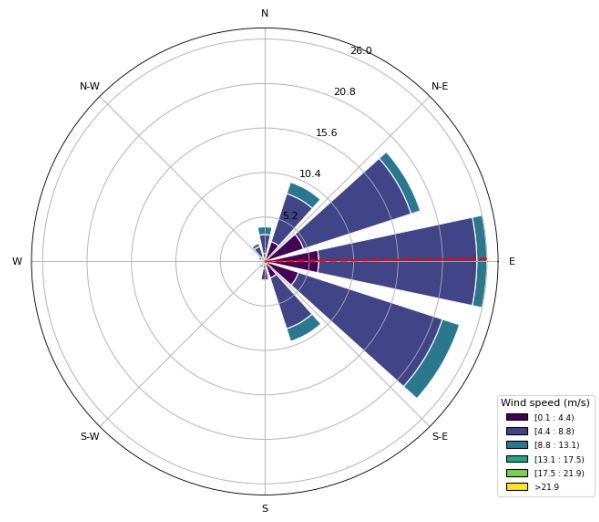

Figure 2.6: Wind rose of the 10-year time series at Puerto Morelos.[1]

The significant wave height, H_s, and wave period, T_p, not only describe the important wave characteristics but are also used as input for the forces on the modelled barrier, as explained in Section 6.2. First, an EVA on the significant wave heights of combined wind waves and swell data from the beginning of 2014 until the end of 2023 is conducted to obtain H_s. Ten years of data is a sufficient time range to get a representative design value for the significant wave height and the design wave period, as the design life of the barrier is 10 years as well. This is discussed in Section 4.1.5. In this EVA, the Peak Over Threshold (POT) method is used to identify the extreme values within the dataset. In Table 2.2 the results of the EVA are displayed. Appendix B explains the methodology for receiving the EVA results in detail.

Table 2.2: Input parameters for all hydrodynamic conditions

Condition	H_s [m]	u_{wind} [m/s]	Wave direction	Wind direction	T_p [s]	Tidal range [m]
1. Small arrival	0.95	5.27	110°	107°	7	0.315
2. Medium arrival	0.85	4.47	110°	107°	7	0.315
3. Large arrival	0.75	4.36	110°	107°	7	0.315
4. Winter conditions	1.03	8.11	26.0°	11.1°	4.7	0.337
5. Extreme values	2.91	17.5	86.3°	50.6°	13	0.174

With this approach, the conditions have been narrowed down to five distinct settings: settings 1 to 3 are relevant for high-intensity sargassum arrival under varying conditions, 4 is used to analyse flushing under northern storms and setting 5 is used to model extreme conditions, ensuring the barrier design remains stable during storm periods.

2.2.4. Tidal settings

An additional hydrodynamic aspect that must be considered is the Yucátan current. At a regional scale, the circulation along the east coast of the Yucatán Peninsula is characterised by the Yucatán Current, which flows northward parallel to the edge of the continental shelf and is a precursor to the Loop Current, which later becomes the Gulf Stream. At the Cozumel channel, the current has a strength of 0.6 $\mathrm{m/s}$.[9] As Puerto Morelos is closer to shore and not at the tight cross-section of the channel, a current with a strength of 0.5 $\mathrm{m/s}$ is used at the outer edge of the southern grid. From where the reef starts the current is linearly interpolated from 0 $\mathrm{m/s}$ until it reaches 0.5 $\mathrm{m/s}$.

Besides the input of the Yucatán current at the southeastern boundary, it also influences the water levels imposed at the eastern boundary. The reef lagoon of Puerto Morelos exhibits a microtidal regime with a tidal range of 0.4 m.[52] As seen in Figure 2.7, the effect of the geostrophic reaction on the Yucatán current, is visible through a low-frequency water level variability on top of the tidal regime. The data shows how the water levels vary between spring and neap tides during higher and lower water conditions. For running the conditions, 1 to 5, mentioned in Section 2.2.1 and Section 2.2.2 respectively. It is necessary to determine which tidal condition applied at the eastern boundary is most relevant to answer the research question effectively. The water levels imposed at the eastern boundary have a direct effect on the location of breaking, which in turn influences the set-up and therefore the extent of the flushing phenomenon. To answer the research question, the model should be tested under conditions where the lagoon is least capable of flushing. This model condition is the most critical, as other settings have higher flushing potential. To investigate this, the tidal regime is divided into four settings; spring tide high water level, neap tide high water level, spring tide low water level and neap tide low water level.

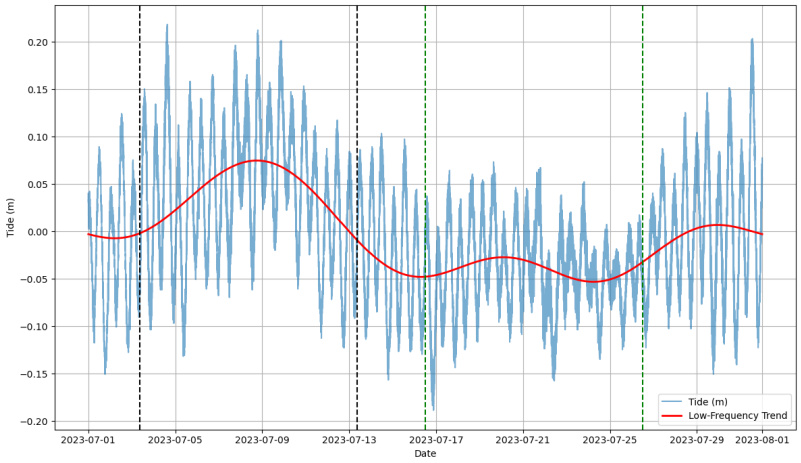

Figure 2.7: Water level fluctuation in July 2023 in front of the Puerto Morelos coast.

The four water level settings are imposed at the eastern boundary, with condition 1 (small sargassum arrival) as the reference run. Model inputs are defined as shown in Table 2.2. The local tide data are obtained at a frequency of 60 seconds from the records of the Meteorological and Oceanographic Academic Service (Servicio Académico de Monitoreo Meteorológico y Oceanográfico (SAMMO)) of UNAM in Puerto Morelos.[68] To find the corresponding tidal input of interest, the focus is placed on water velocities located at the opening channel of Boca Grande. In Figure 2.8 (I) and (II), and Figure 2.9 the 4 tidal conditions are demonstrated. The results are summed up in Table 2.3.

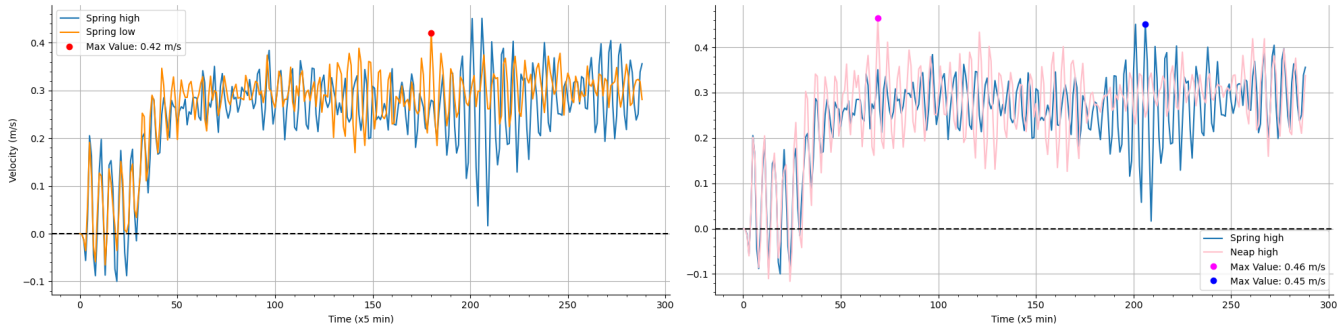

Figure 2.8: Depth-averaged velocity at Boca Grande during spring tide at high water versus low water (I), and during spring versus neap tide at high water (II).

Table 2.3: Tidal parameters for spring and neap tides in July 2023

Tide	Date	Tidal range [m]	Max velocity [$\mathrm{m/s}$]	Mean velocity [$\mathrm{m/s}$]
Spring tide high water	04-07-2023	0.315	0.45 at 17:10	0.25
Neap tide high water	15-07-2023	0.174	0.46 at 05:45	0.26
Spring tide low water	16-07-2023	0.226	0.42 at 15:00	0.27
Neap tide low water	25-07-2023	0.134	0.43 at 15:35	0.30

Figure 2.9: Depth-averaged velocity at Boca Grande during spring tide at low water versus neap tide at low water

The results show the depth-averaged velocities during a 24-hour simulation. The first two hours of the time series are not representative, as the waves start at 02:00 in the model. The results listed above, show that under spring tide at high water, the overall outflow is the least powerful. For model conditions 1 to 3, this tidal regime is used as input. For the winter condition the spring tide at high water is used as well, but then obtained from the January time series. For the EVA however, the highest velocities are mostly significant. Velocities give, as described in Section 6.1, the highest forces on the barrier. Therefore, neap tide at high waters is used as model input at the eastern boundary.

Finally, to make a good comparison between the model outcomes of the first three hydrodynamic conditions, for every run the moment when the outflow at Boca Grande is at its maximum, is used as the 'Time of Interest' (TOI). This can be seen in Figure 3.2 in Section 3.1.1.

2.2.5. Assumptions and other settings

The other required parameters in the model are listed below:

- Gravitational acceleration g: 9.81 $\mathrm{m/s^2}$
- Water density ρ: 1022 $\mathrm{kg/m^3}$ [17]
- Wind drag coefficients A, B, C respectively: 0.0008 at 10 $\mathrm{m/s}$, 0.0024 at 40 $\mathrm{m/s}$, 0.0020 at 100 $\mathrm{m/s}$ [21]

Furthermore, in addition to the eastern boundary where tidal input is applied and the southeastern boundary where the Yucatán current is set, two other boundaries are also defined within the model. In the southwest, from the coast to the reef a current is added, linearly interpolated starting from 0 and decreasing to -0.1 $\mathrm{m/s}$. This boundary ensures the possible outflow of water from the reef lagoon at the southern gate. A Neumann boundary condition is applied at the northern boundary.

Lastly, this study aims to investigate the upper-surface horizontal flow patterns around the reef lagoon. Therefore temperature and salinity are taken as constants within the model. Other hydrodynamic parameters consistent across all runs include a directional spreading for waves of 4 [-]. Wave breaking in the model can occur due to white capping and depth-induced breaking, with a breaking parameter (γ_b) of 0.73 [-].

2.3. Modelling of sargassum

In this section, the approach of modelling sargassum in Delft3D is given and further assumptions are clarified. In Section 2.3.1 the physical properties of sargassum are explained. This is required to decide which model setting would best imitate sargassum movement behaviour, further discussed in Section 2.3.2.

2.3.1. Sargassum properties

Determining the density of sargassum is challenging because it is an organism with variable distribution and growth patterns. Its chemical composition and concentrations fluctuate throughout sargassum mats, influenced by environmental factors such as ocean currents, light, and nutrient availability. Wang et al. (2018) measured the area density of sargassum through field and laboratory experiments. While biomass density varied across different testing locations, the average biomass density is 3.34 ± 1.34 $\mathrm{kg/m^2}$, with a relative uncertainty of about 12%.[70]

Sargassum contains gas-filled structures called pneumatocysts, primarily filled with oxygen. These structures provide buoyancy, allowing the plant to float on the ocean surface [51]. As a result, sargassum is influenced mainly by surface currents in free-moving water bodies.

To model sargassum in Delft3D, a mass per volume measurement in cubic meters is required. Sargassum mats can reach a thickness of up to 70 cm in ocean waters [5], though not all particles extend to this depth. Based on field observations in Puerto Morelos conducted by the project team, an average mat thickness of 25 cm is assumed for this research. With this assumption, the density of sargassum is estimated to be 13.36 $\mathrm{kg/m^3}$.

In surface waves, fluid particles follow an orbital motion, but their net horizontal displacement is not zero. This wave-induced drift, known as Stokes drift, always occurs in the direction of wave propagation. A particle at the top of its orbit, beneath the wave crest, moves slightly faster forward than it does backwards under the wave trough. The mean drift velocity is proportional to the square of the wave height, making it a second-order effect. Floating sargassum moves with both the Stokes drift and tidal currents. Additionally, research has shown that wind significantly influences sargassum movement. Incorporating wind data into ocean current models greatly improves the accuracy of sargassum transport predictions.[56]

2.3.2. Modelling options

With the main physical characteristics of sargassum determined, the next step is to model it realistically in Delft3D. Two methods are considered for this: drogues and tracers. Table 2.4 compares both methods against the characteristics of sargassum.

Table 2.4: Sargassum properties compared with modelling methods.

Property	Drogue	Tracer
Mass	No	Yes
Floating	Yes	Possible
Wind	Indirect	Direct
Cohesion	No	Possible
Complexity	Simple	Complex

To evaluate whether the characteristics of the two methods align with the expected behaviour, both drogues and tracers are tested in Delft3D. First, the results in Table 2.4 are discussed. Neither methods directly provide an option that accounts for mass, which can be derived from the density. For example, the Moon Palace resort data shows that the maximum volume of sargassum arriving on a single day in 2024 was 1183 $\mathrm{m^3}$, corresponding to nearly 16 tons of biomass.[50]

In Delft3D, less mass is used to simplify and speed up the simulations. The particle tracking function allows a maximum of 1000 particles, meaning that each particle would represent 16 kg, which would be too heavy for accurate modelling. Instead, each particle is set to represent a 1 $\mathrm{m^2}$ sargassum mat, giving a weight of 3.34 kg per particle.

Both methods include a floating option, but only the tracer is directly influenced by wind. Figure 2.10 compares the movement of GPS-tracked sargassum with tracers modelled in Delft3D under different wind drag coefficients. The results show that a wind drag coefficient of 3% provides the closest match to the observed movement of the sargas-

sum. In contrast, when a zero wind drag coefficient is applied, as in the drogue method, the modelled sargassum significantly deviates from real-world behaviour. Therefore, a wind drag coefficient of 3% is used in this project.

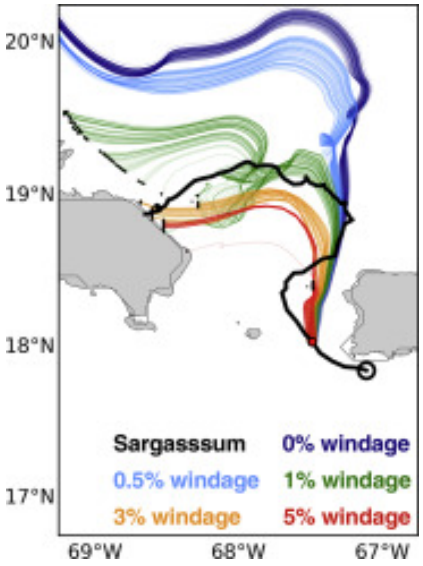

Figure 2.10: Track of GPS-followed sargassum versus tracers with different wind drag coefficients.[57]

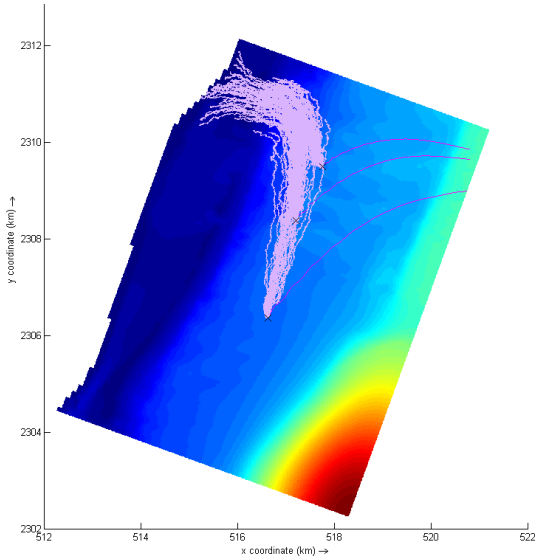

Figure 2.11: Drogue (purple) versus particle tracking (pink) offshore at Puerto Morelos.

Cohesion of sargassum is another property that must be considered. In the case of a tracer, this can be modelled by adjusting the horizontal diffusion parameters. In the Delft3D model, default settings are used for these parameters, as the exact diffusion properties of the sargassum are unknown. The determination of these parameters is beyond the scope of this project. One important aspect is that drogues are simpler model devices as they do not require many parameters. This makes them easier to implement and reduces computational time compared to tracers. Both modelling options were tested in the reference run under tidal conditions. In Figure 2.11, the movement tracks of a drogue and single particles are compared. It can be concluded from the figure that drogues do not perform as expected, largely due to the absence of wind drag in their calculations. As a result, particle tracking, specifically using tracers, is the method used to model the sargassum for the analysis in Chapter 3.

2.3.3. Placement location of drifters

Within the Puerto Morelos reef lagoon, there exist three gate channels where the outflow of water can occur as part of the recirculation flow. In Figure 2.12 these are indicated as big gate (Boca Grande), medium gate and small gate. To investigate the capability of the reef lagoon to redirect sargassum particles back to the ocean currents under different conditions, drifters are released at the following locations:

- South west: to test the ability of flushing if sargassum arrives from the south.
- North west: to test the ability of flushing if sargassum arrives from the north.
- East of big gate: to test the ability of flushing
- East of medium gate: to test the ability of flushing
- East of small gate: to test the ability of flushing
- East of the reefs north, medium and small to investigate how sargassum is influenced by the recirculatory flow patterns when entering the reef

Additionally, observation points are added in specific grid cells to collect hydrodynamic results from an Eulerian frame of reference. The locations of the observation points and drifter release locations can be seen in Figure 2.12.

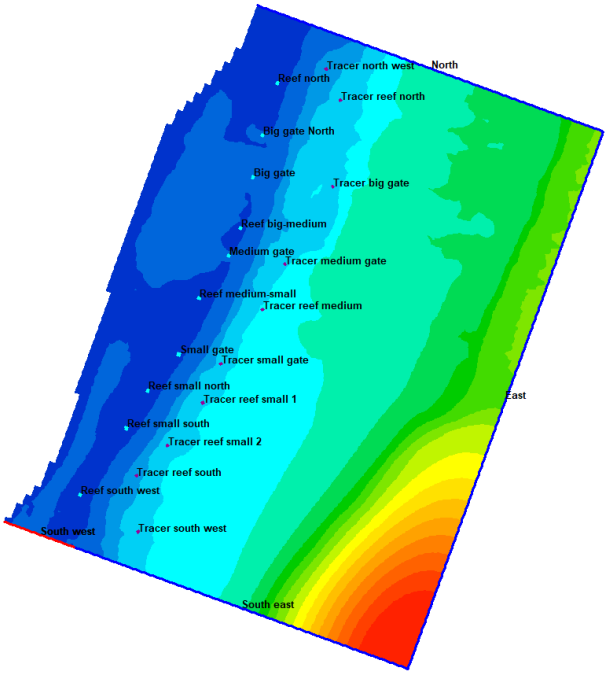

Figure 2.12: Observation points and release location of tracers in front of the coast of Puerto Morelos

2.4. Modelling of a floating barrier

To investigate how an implemented floating barrier affects the hydrodynamic flow patterns around the reef, which in turn affect the pathways of sargassum, a floating barrier has to be modelled in Delft3D. The barrier consists of three components: a buoy, a mesh grid net and mooring lines. In Delft3D there are several methods to implement a barrier or floating structure in the model. For this research, the buoy and the mesh grid are the dominant structural elements influencing the flow and the accumulation of sargassum. Delft3D offers two different techniques to represent these elements. A porous plate can simulate the mesh, while the buoy can be modelled as a floating barrier extending over several layers.

A porous plate in Delft3D is a partially transparent structure covering some or multiple layers in the vertical but with a very thin thickness compared to the grid size. For the porous plate, the inputs required, in addition to the mesh locations, are the number of layers through which the plate extends and the coefficient of friction for quadratic friction. This coefficient is a calibration parameter that provides an estimate of how much water flows through the barrier. It can be adjusted to accurately describe the flow behaviour upstream and downstream of the gate. As in this research no barrier is tested in the laboratory nor flow around an existing structure is monitored, this method is outside the scope of the project. However, to investigate the behaviour of sargassum when trapped in front of a barrier, the use of a floating structure provides a suitable alternative to model this.

The introduction of a floating barrier affects the incoming waves. As waves approach the breakwater, some wave energy is reflected, while the remainder is transmitted. This results in a reduced wave height behind the floating barrier, which reduces the amount of radiation stresses when waves break at the front side of the reef. Wave attenuation caused by the breakwater thus leads to a reduced set-up, which decreases the force of the outflow. The functioning of the breakwater is illustrated in Figure 2.13. However, this process only applies if the breakwater is placed before the waves break on the reef, at off-shore located waters. In this project, where the focus is on designing a floating breakwater within the reef lagoon, the reduction in wave set-up is negligible. Therefore in Section 3.2, the absence of a floating barrier in the model is expected to have no significant large-scale impact on the hydrodynamic conditions in the reef lagoon.

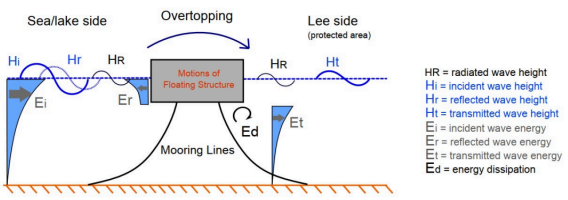

Figure 2.13: Interaction between floating breakwater and incoming waves.[12]

3 Hydrodynamic analysis

To design a floating barrier that effectively captures or redirects sargassum back into the ocean currents, a thorough analysis of the flow conditions and the impact of the flow on the barrier is required. This chapter aims to determine whether it is possible to shape a floating barrier in the Puerto Morelos reef lagoon in a way that increases the chances of flushing. This chapter utilises the Delft3D modelling software to better understand the circulation currents within the reef lagoon. In Section 3.1, the results of the summer and winter conditions are investigated based on the model output. Along with the results of the modelled sargassum behaviour under these conditions, an analysis is conducted to determine the optimal location for a floating barrier. This is discussed in Section 3.2. In Section 3.3 the impact of the floating barrier on flow behaviour and sargassum transport is modelled and discussed. The chapter concludes with the modelled output from the EVA. Based on the optimised barrier location, the required results for the structural part are defined.

3.1. Modelling results of various conditions

In the following subsections, the flow patterns within the reef lagoon under different conditions are analysed. Especially the flow behaviour at the three gates mentioned in Section 2.3.3 are highlighted. Other interesting patterns are brought forward as well. This is done to distinguish which condition is most relevant to analyse flushing conditions and which are the main in and outflow regions of the lagoon. All figures have magnitude colour maps set to the same value range, facilitating visual comparability. The figures also contain vectors pointing in the directions of the currents. Note that all figures are displayed on a large scale in Appendix C, for a more clear observation.

3.1.1. Hydrodynamic results based on Delft3D

In the first four conditions, the presence of the Yucatán current is evident. Due to the bathymetry, it can be seen that the current bends to the east. At every timestep, the current velocities induced by waves, tides and wind are directed to the northeast direction at the eastern border. Based on these results, at all times the Yucatán current consistently dominates over the wave- and wind-induced currents outside of the reef region shown in Figure 3.1.

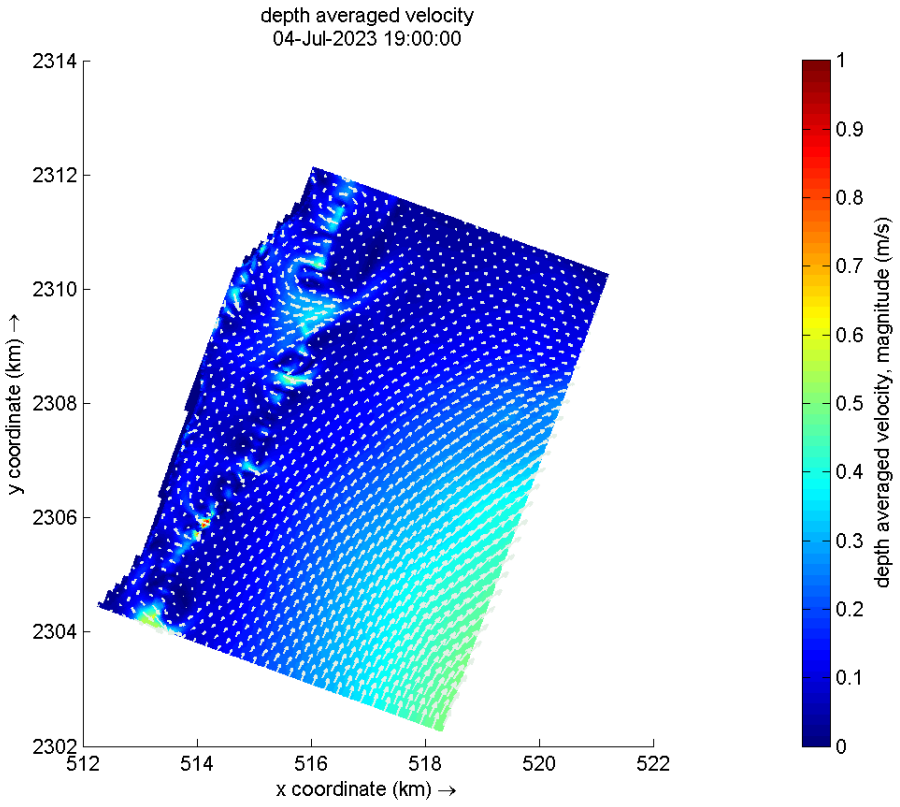

Figure 3.1: Depth-averaged velocity vectors during condition 3 at 19:00, during a 24-hour run Delft3D.

All summer conditions are subject to the same tidal forcing, thus wave height and wind magnitude are the dominant influences on the currents within the reef. In Figure 3.2 and Figure 3.3, the flow patterns outside of the big gate (Boca Grande) are shown when the outflow is at its maximum, for all three summer conditions. For winter conditions a stabilisation of the currents is observed after approximately 8 hours. This situation is most interesting as this gives the most realistic flushing scenario for condition 4. For all simulations, the wave input starts after two hours, so the values until 02:00 are not representative.

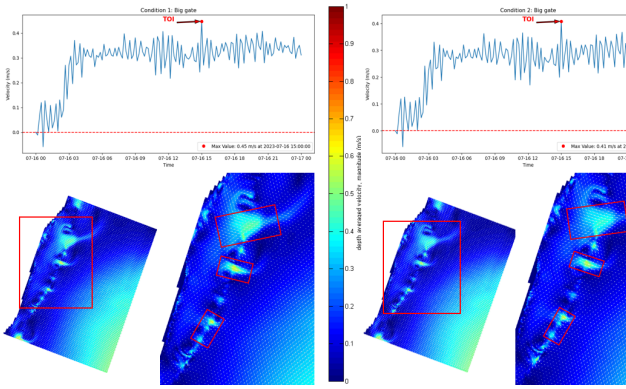

Figure 3.2: Outflow conditions 1 (left) and 2 (right) at TOI, 24-hour run Delft3D.

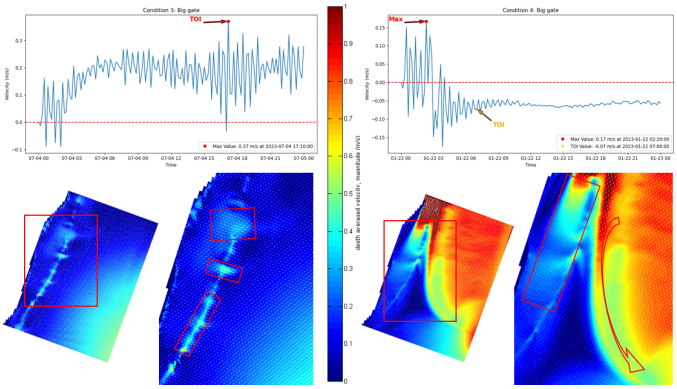

Figure 3.3: Outflow conditions 3 (left) and 4 (right) at TOI, 24-hour run Delft3D.

With the obtained results from the Delft3D models, the flow for all 4 conditions can be analysed. The objective is to identify all the circulation patterns and outflow locations of the reef, as they are relevantly influencing the behaviour of sargassum. These phenomena could lead to flushing within the reef, which clears the sargassum and thus no barrier is required at those locations. The current velocities in Figure 3.2 and Figure 3.3 (left), observed in the middle of Boca Grande, show that in all three summer conditions, at all times the flow is eastward directed. The time instant before the TOI in condition 3 is the only moment that no outflow in the big gate occurs, because of the great oscillation in that moment. The constant outflow indicates a well-working flushing behaviour of the reef lagoon system around the big gate. In Table 3.1, the percentage of depth-averaged velocities flowing towards the east, an indication of outflow is demonstrated. From these results, it becomes visible that the reef has two main outflow zones. These are at observation locations medium gate and small gate. The main inflow is at the reef locations. The highest velocities, up to 0.8 $\mathrm{m/s}$, were found along the reef crests, where the sharp depth change and wave breaking generated currents directed transversely across the reef. Based on the time series, constant outflow occurs at all three gates for conditions 1 and 2. The small gate in condition 3 has an outflow of 94.7% of the time, which is also contributing to flushing. The fourth condition is analysed further in Section 3.1.2, as this is not a standard sargassum arrival condition with wind and flow coming from the northeast. With the help of Table 3.1 it can be concluded that the total outflow is the least in condition 3. The condition where the weakest flushing occurs is the high sargassum arrival scenario, making this the most critical condition in terms of sargassum retention and flushing capability. This condition is taken to analyse circulation patterns and is decisive for the decision of barrier placement from now on.

Table 3.1: Outflow in percentages across all different observation points

Location	Condition 1	Condition 2	Condition 3	Condition 4
Big gate	100.00	100.00	98.48	3.79
Medium gate	99.24	99.24	98.48	97.73
Small gate	99.24	99.24	94.70	96.21
Big gate north	96.97	93.94	75.76	3.03
Reef north	3.79	3.79	9.09	98.48
Reef big-medium	18.94	21.97	30.30	96.97
Reef medium-small	4.55	6.06	16.67	94.70
Reef small north	53.03	49.24	53.03	93.94
Reef small south	63.64	68.94	33.33	51.52
Reef south-west	7.58	5.30	15.91	48.48
Total average	54.70	54.77	52.58	68.49

The combination of in and outflow in the reef creates circulation patterns, known as gyres. Three main gyres can be observed in Figure 3.4, where the main circulation regions of the reef are highlighted. The outflow of the big gate creates an anti-clockwise gyre with the inflow of reef north and a clockwise gyre with the reefs south of the big gate. The southwest outflow location of the reef creates an anti-clockwise gyre induced by a high inflow coming from the

reef in the south (red coloured patches in ”Flow circulation reef south”). The small and medium gates also create small gyres in the middle of the reef. The impact of all the gyres is analysed in Section 3.1.2 in which sargassum is released to demonstrate the flow of the particles. Together with this analysis, the location of the barrier is determined.

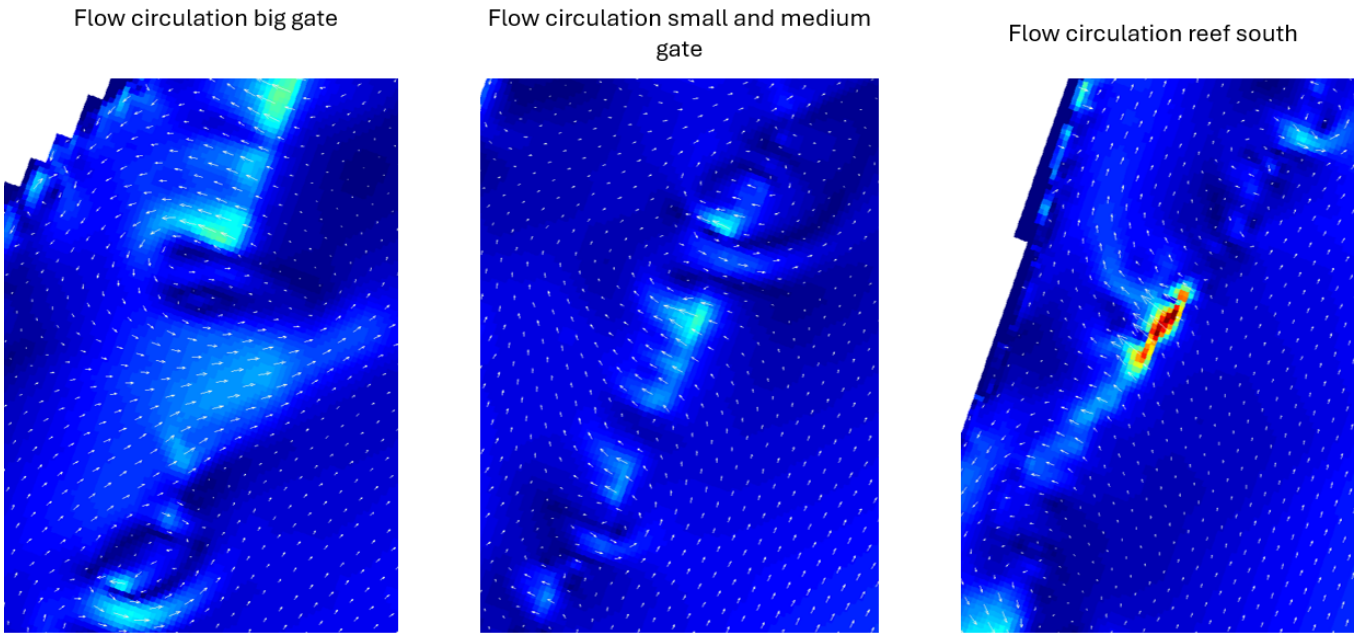

Figure 3.4: Detailed flow patterns of the upper layer (first 20% of water column) for condition 3.

Besides the capability of the lagoon for flushing, it is important to investigate the flow behaviour within the reef and in front of the reef in the y-direction (north/south). Within the reef are multiple segments where circulation patterns occur which can be seen in Figure 3.4. If sargassum would directly flow along with these currents it is moved toward the gates and pushed outside of the reef. For the y-directed currents, it is interesting to see that at all observation locations, the direction is different. In front of the reefs in the south and between the gates, water is pushed towards the north, while at the reef in the north, it is directed to the south. Nonetheless, it is clear to see that at all locations there is a component in y-direction that could have the ability to move the sargassum along a barrier. Overall, the dominant flow within the lagoon is directed north-northeast. The narrowing of the lagoon at latitude 2311000 intensifies the current, which exits the lagoon at the big gate. This forms circulation gyres and together with the outflows, enhances the flushing phenomenon. Whether the flushing effect is strong enough to keep sargassum out of the reef, is tested in Section 3.1.2.

3.1.2. Sargassum behaviour based on Delft3D

First, the sargassum is released at the locations specified in Section 2.3 for conditions 1 to 4. At each location, 100 particles are released in a six-hour run to investigate from which points the particles enter the reef and where they are flushed back offshore. Once offshore, the particles are carried away by the Yucatán Current. Conditions 1 to 3 show similar distribution patterns, with condition 1 exhibiting the most intense flushing magnitude. However condition 4 shows entirely different distributions, as it is the only condition with waves and wind coming from the northeast. For condition 4 two important findings need to be highlighted based on the results in Figure 3.5. First, the Yucatán current loses strength as it moves from south to north, and as discussed with the help of Figure 3.1, the current still bends off to the east due to the bathymetry. Additionally, it can be seen that particles released at the northern boundary just at the edge of the reef, have no chance of entering the reef until they reach the southern reef. From the release point ”Tracer reef small 2” southward, the water currents push the sargassum toward the coast. The combination of these findings indicates that, on one hand, sargassum drifts out to sea starting east of the large gate, while the remaining particles accumulate at the critical point south of ”Tracer reef small 2.”

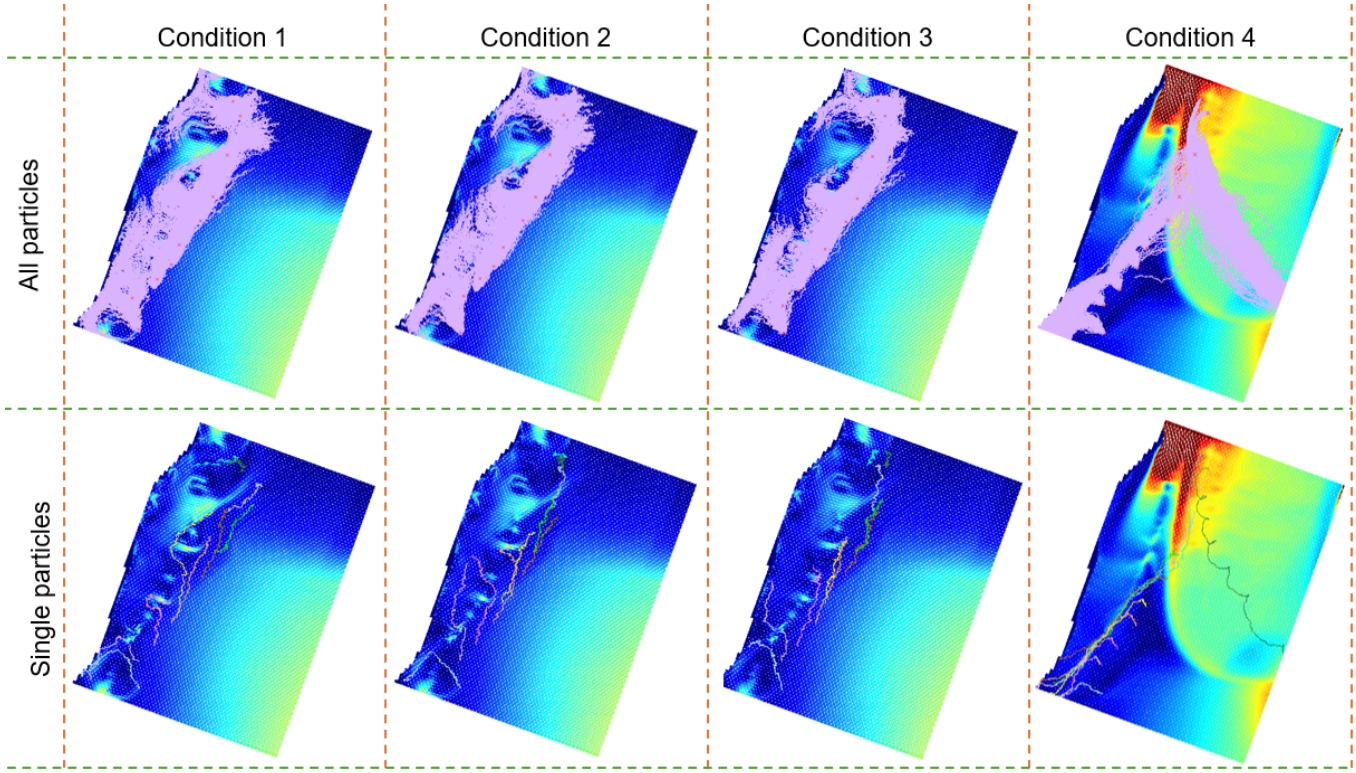

Figure 3.5: Particle tracking for conditions 1 to 4 at Puerto Morelos for 5 hours.

Based on the results of all particles and individual particles for conditions 1 to 3, it can be concluded that sargassum enters two main regions; at the reef north of Boca Grande and at multiple locations of the reef south of the medium gate. The small gate contributes little to the flushing process. While it does flush a few particles, the waves just north of the small gate push them back into the lagoon. In all three conditions, however, the big gate stands out as the dominant flushing point, with no particles being able to pass through the opening towards the coast. To further analyse the behaviour of the sargassum in the middle of the reef around the medium and small gates, an eight-hour run is carried out using the settings from condition 3. The results, shown in Figure 3.6, clearly demonstrate that the outflow in the small and medium gates helps the particles to flow towards the large gate where they are flushed out of the lagoon. This indicates that the primary areas where the sargassum reaches the shore without being flushed away are the reefs to the south and north. Further details are provided in Section 3.2.

3.2. Optimal Placement of Floating Barrier

For the optimal location and orientation of the barrier the following four aspects need to be taken into account: flushing areas, circulation patterns, flow along the barrier and wave dissipation due to the reef. The first two factors determine effective regions where a barrier is not needed as the natural hydrodynamics of the lagoon can redirect sargassum back to the sea itself. These regions have been thoroughly analysed in Section 3.1.

The placement of the barrier is primarily determined by the flushing dynamics under condition 3, as well as the regions where sargassum inflow occurs. The analysis in the previous section has shown that the inflow areas are predominantly located in the shallow parts of the reef. The circulation patterns show that at multiple locations sargassum is immediately discharged back into the open sea through the natural gates in the reef. These flushing areas are critical to consider when planning the barrier location, as they inherently manage the outflow of the sargassum. Therefore, placing the barrier in these areas would be ineffective as the natural hydrodynamic forces already prevent sargassum from reaching the shore in all three inflow conditions. Consequently, the barrier should be placed outside the active flushing areas, all three gates and the south channel, to avoid interfering with these natural processes, while ensuring that the sargassum influx is effectively blocked. According to the results, this requires the placement of a barrier along the southern reef and the northern reef, extending up to the flushing areas. These regions extend from the south channel up to the small gate for the southern barrier and from the big gate northwards until the northern boundary for the northern barrier, both indicated in Figure 3.6 (II).

In addition to the reef lagoon flow patterns, the third factor influencing the location and orientation of the barrier is the flow directed along the barrier. For a barrier designed to enhance the chance of redirecting sargassum back to the sea, at all locations of the barrier the flow needs to be directed to one of the flushing ends. If this is not the case, accumulation of sargassum can occur. Accumulation of sargassum at one specific point has two setbacks. First,

it creates extra structural load on the barrier at a specific point in the barrier chain. Secondly, when sargassum is trapped at a single position, over time it loses its buoyancy and thus sinks underneath the barrier ending up in the reef lagoon. [51] To prevent sargassum from accumulating along the barrier, the orientation of the barrier needs to be adjusted. The objective is to orientate the barrier in a way which effectively pushes sargassum to the ends where flushing occurs. Further analysis of the optimal orientation is given in Section 3.3.

The fourth factor influencing the placement of the barrier is the hydrodynamic forcing. An optimal barrier design is presented in Section 4.5, followed by a structural analysis in Chapter 6. The forces acting on the sargassum barrier are primarily determined by H_s and T_p. For a more detailed discussion of dynamic forcing, refer to Section 5.3. At this stage, it is important to note that higher values of H_s and T_p results in greater forces on the barrier. From the eastern boundary, the waves undergo shoaling as they approach the reef, where water depth decreases and the waves eventually break. Due to this process, the wave energy dissipates on the reef, leading to a reduction in H_s and T_p behind the reef. Consequently, to minimize the dynamic forces on the barrier, it is preferable to construct it within the lagoon, where the wave energy has already been significantly reduced. For condition 3, the location where wave breaking occurs can be seen in Figure 3.6 (II), where the map colour changes from red to green at the location of the reef.

Based on the results of the sargassum flow patterns, the overall circulation in the reef lagoon and the breaking region, two barriers are selected for testing as shown in Figure 3.6 (II). The sargassum that reaches the shore is concentrated in the southern and northern parts of the reef. The circulation initiated by the large gate is visible in Figure 3.6 (I), with all particle paths shown. The inflow and flushing of the reef are illustrated by several individual particle trajectories in the right panel (II) of Figure 3.6. The green lines represent particles that are flushed out and do not reach the coast, while the red lines represent sargassum particles that reach the coast of Puerto Morelos. The green line moving through the middle illustrates flushing through the middle gate. The red bars in the figure mark the optimal barrier locations, in which H_s is low due to wave breaking. Positioning the barriers in these areas blocks the inflow that would otherwise reach the shore, without impeding any flushing currents. The barrier is oriented parallel to the reef from which the sargassum arrives, with its ends positioned next to a flushing area. This orientation ensures that sargassum is redirected back into the sea as it flows along the barrier. In Section 3.3 a further analysis is done to check whether sargassum can move toward the flushing areas along the barrier accordingly.

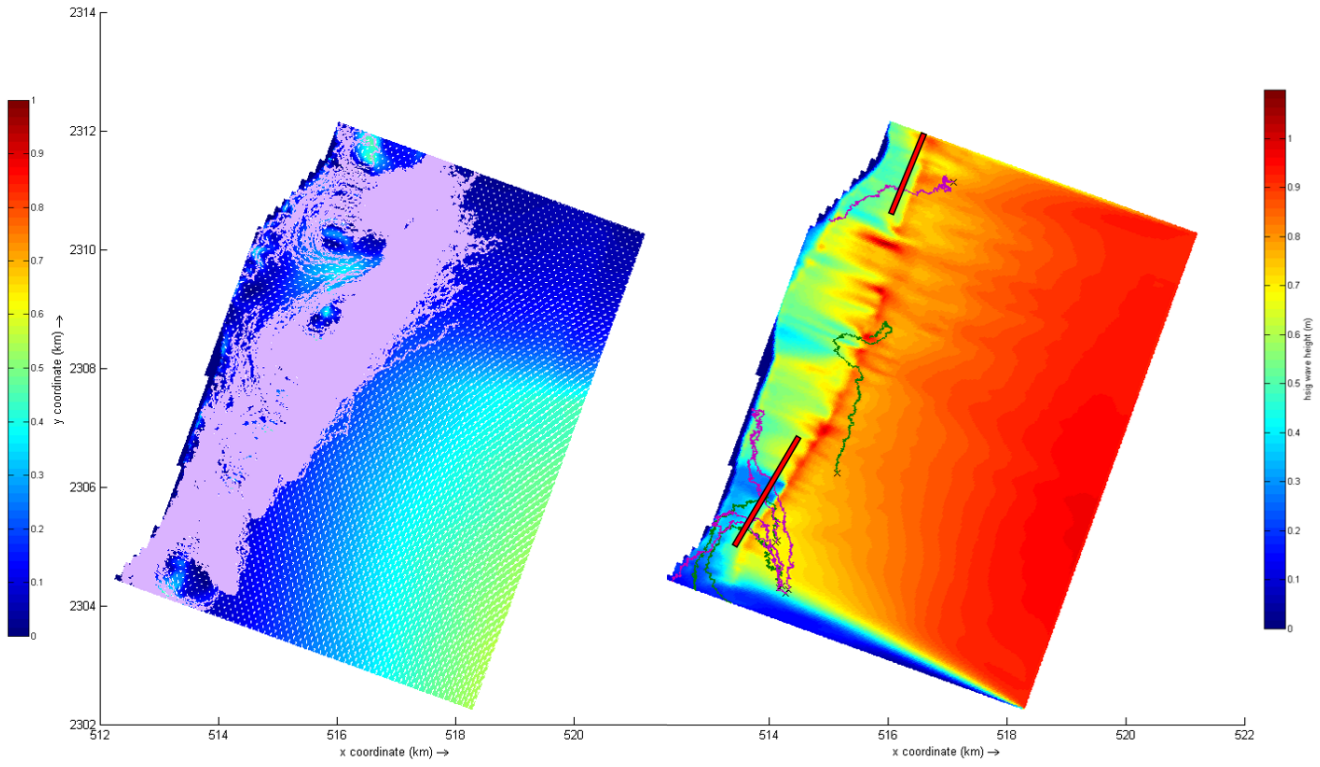

Figure 3.6: Distribution of sargassum particles during a 7-hour simulation (I) and single particle flow patterns with the optimal placement locations for a barrier during condition 3 (II).

Information barriers 1 (South) and 2 (North), with the the axis starting at 0° North:

- Information barrier 1: Angle with respect to NSWE-axis: 33.7°, Length: 2160 [m]
- Information barrier 2: Angle with respect to NSWE-axis: 23.3°, Length: 1370 [m]

3.3. Influence of floating barrier on sargassum transport

In this section it is investigated whether under the placement of the barrier, sargassum has the ability to move along the barrier towards the flushing locations. In Figure 3.7, the results of the interaction between a floating barrier and sargassum particles with the use of three different methods are illustrated. All three examples show how sargassum transports within the upper layer through the barriers as indicated by the red boxes. Even when the flow is zero in all directions as depicted in Figure 3.7 (II) and Figure 3.7 (III), the modelled particles still transport through the barrier. Unfortunately the results show that the Delft3D cannot accurately model the interaction between floating structures and tracking particles. A further explanation of the implementation of floating structures in Delft3D is given in Appendix D.

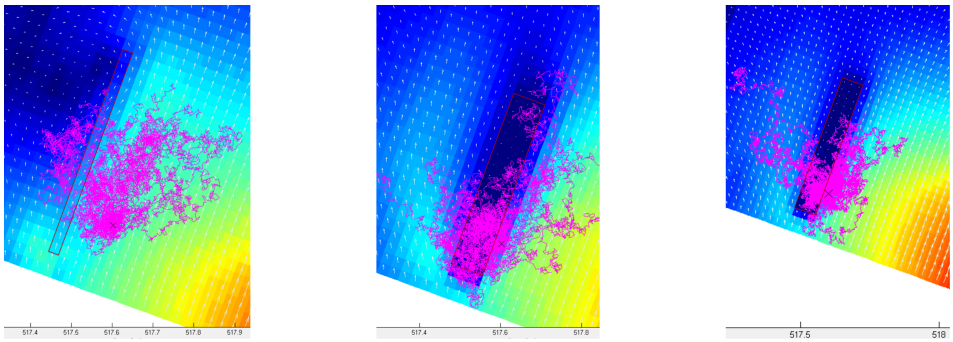

Figure 3.7: Sargassum interaction with floating barrier (I), sargassum interaction with rigid sheet (II), sargassum interaction with 3D-gate (III).

However, by using observation points at the location of the barrier, an estimation of the behaviour of sargassum particles in front of the barrier is made. For this estimation, it is assumed that the placement of a barrier does not affect the flushing capacity of the gates. In Figure 3.8 (I) the location of the observation points is illustrated based on the results of Section 3.2. In Table 3.2 the average depth-averaged velocities during condition 3 are presented in the direction along the barrier during the first test. The results show that barrier 1 pushes water southwards along the southern half of its length and northward along the northern part of the barrier. From location (34,59) to the southern end of barrier 1 (28,34), there is an overall flow toward the south, where sargassum is pushed back into the ocean as seen in Figure 3.6 (I) at the southern edge. North of (34,59) the flow direction shifts northward, pushing sargassum toward the gates where outflow occurs. The weakest current is observed at location (38,76) with an average velocity of 0.016 $\mathrm{m/s}$, or 58 $\mathrm{m/h}$. The direction of flow relative to the barrier is shown in detail in Figure C.21.

Table 3.2: Average current in the direction along the barriers of test 1 with condition 3 input

Location	Barrier	Average current $\mathrm{m/s}$	Direction
28,34	1	0.073	South
30,42	1	0.060	South
32,51	1	0.065	South
34,59	1	0.038	South
36,68	1	0.046	North
38,76	1	0.016	North
40,85	1	0.044	North
43,97	1	0.072	North
46,110	1	0.110	North
57,259	2	0.044	South
57,269	2	0.054	South
58,279	2	0.017	South
58,289	2	0.005	*North*
59,299	2	0.069	South
60,308	2	0.042	South

In contrast, the results of barrier 2 demonstrate its ability to directly transport sargassum towards the big gate from location (57,259) to (58,279). A weak point is identified between (58,279) and (59,299), where only northward-directed current is observed. The rest of the barrier shows relatively strong currents directed toward the big gate. To prevent sargassum from accumulating between these two points, the orientation of the barrier needs to be adjusted. For example, if the orientation of the barrier at the location of this weak link is set to 30°, the currents shift to 0.030 $\mathrm{m/s}$ southward. This adjustment ensures that all flow along the barrier is directed toward the main gate where flushing occurs.

A second test is applied with an overall adjusted barrier orientation of 28.2°. The location points and the depth-averaged velocities along the barrier of the northern border are presented in Figure 3.8 and Table 3.3 respectively. However, with the adjusted orientation and thus a different location for the observation points, the flow still exhibits conflicting directions at the northernmost three points. In this configuration, the weak point occurs at (58,299), where the current shifts from southward to northward between (58,299) and (56,289). Although this suggests potential accumulation, the current at (58,299) is directed offshore with maximum velocities of 0.42 $\mathrm{m/s}$, creating a flushing effect that prevents sargassum accumulation between these two points.

A detailed overview of the currents at the location of the observation points along the barrier is provided in Figure C.21, Figure C.22 and Figure C.23. From Figure C.22 it is evident that in the first test at location (59,299) the overall flow is also directed offshore. Thus, both barrier orientations demonstrate a self-organizing effect that pushes the sargassum away, preventing accumulation. There is however one key difference between the two test locations which highlights the optimal orientation. In the second test, the barrier is located closer to shore, which results in greater wave dissipation. As seen in Figure C.22, currents can reach up to 0.7 $\mathrm{m/s}$ at location (58,279), while in Figure C.23 the maximum occurs at (59,308) with velocities up to 0.6 $\mathrm{m/s}$. From a structural perspective, the second orientation is the more effective choice.

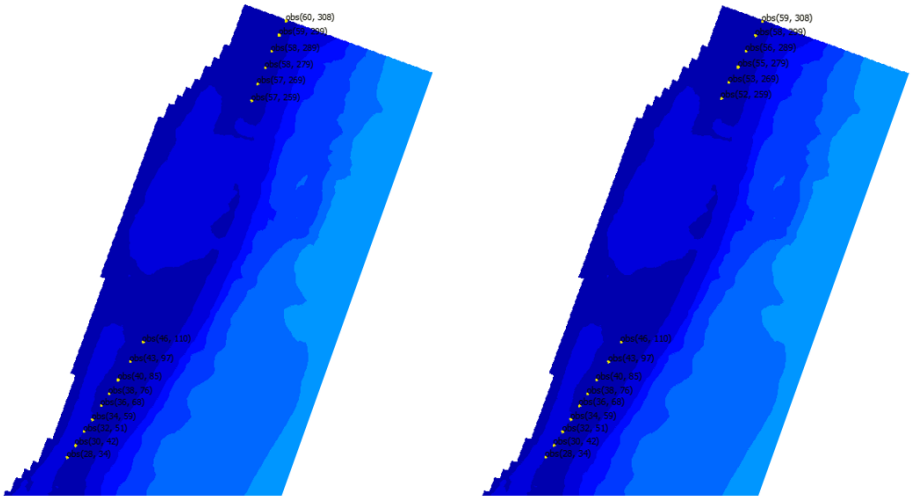

Figure 3.8: Locations of the applied observation points for barrier 1 (South) and 2 (North) during the first test (I) and the second test (II).

The second test shows that under depth-averaged velocities, the flow has the ability to push sargassum toward flushing gates or redirect sargassum toward the sea at the location of the barrier itself. The final information on the optimal barrier location and orientation are listed as follows:

- Barrier 1: angle with respect to NSWE-axis: 33.7°, length: 2160 m, starting and ending coordinates are (513255, 2305038) and (514450, 2306850) respectively.
- Barrier 2: angle with respect to NSWE-axis: 28.2°, length: 1375 m, starting and ending coordinates are (516019, 2310687) and (516670, 2311900) respectively.

Table 3.3: Average current in the direction along the barriers of test 2 with condition 3 input

Location	Barrier	Average current along barrier [$\mathrm{m/s}$]	Direction
52,259	2	0.076	South onshore
53,269	2	0.052	South onshore
55,279	2	0.017	South onshore
56,289	2	0.017	North onshore
58,299	2	0.027	South offshore
59,308	2	0.033	North onshore

Lastly, during a 7.5-hour simulation sargassum particles are released at the ends of the barrier to confirm whether all particles are flushed out into open waters and not end up along the coastline. In Figure 3.9 the distribution of 100 particles at each end is shown, confirming the effective flushing behaviour under the chosen barrier placement. This finalises the choice of location and orientation of the barriers, addressing the main question stated in Section 1.3.

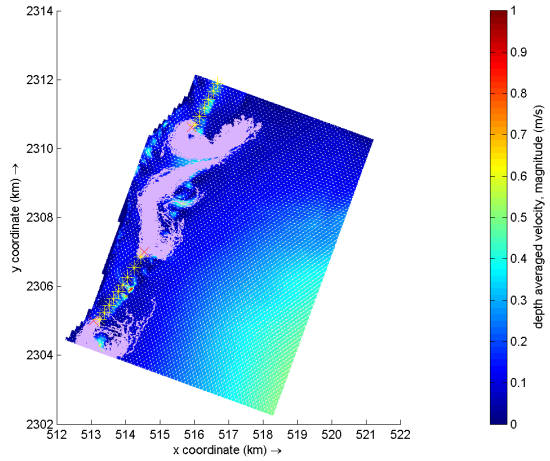

Figure 3.9: Distribution of sargassum particles during a 7.5-hour simulation, released at the ends of barriers 1 and 2 (red crosses) for the second test location. For this model condition 3 is used as the input setting.

3.4. EVA condition for structural input

For the force determination of the structural model, the following hydrodynamic inputs are required: H_s, T_p, the incoming current velocity u and the direction of the incoming current relative to the barrier in degrees. From Section 3.3, the optimal location along with the length and angle of the barrier relative to the NSWE-axis (0° N), has been determined. In Delft3D, by adding observation points, the hydrodynamic inputs described above can be determined. Figure 3.10 illustrates the locations of the observation points and shows how the waves have already broken on the reef with EVA conditions before reaching the floating barrier. It is interesting to observe how a separation line forms from the northeastern boundary extending to the opening of the northern gate, indicating wave breaking offshore above the separation line. In Table 3.4 the maximum values for three different barrier locations are presented. These locations were chosen based on the Delft3D results by selecting the highest values of H_s, T_p, and the velocity in the x-direction (west/east) in the upper layer independently. The locations are indicated by red markers in Figure 3.10.

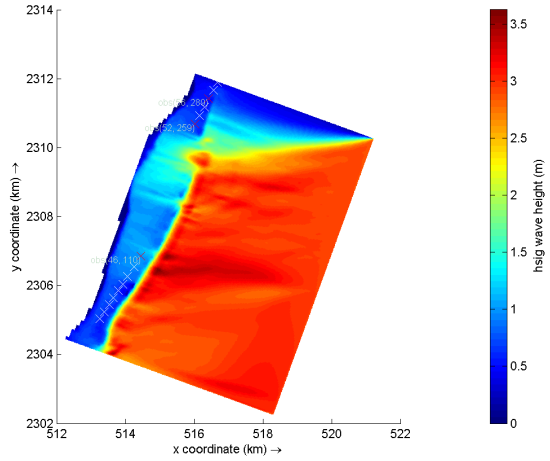

Figure 3.10: Wave map of H_s during EVA settings and the observation points at the location of barrier 1 (south) and 2 (north).

In Section 6.1, the dominant combination of hydrodynamic outputs is further discussed. In Table 3.4 the direction relative to the barrier is defined as the angle between flow and the barrier (black line going from 90° to 270°). This can be seen in Figure C.17, where the red dotted line shows the incoming direction concerning the barrier during maximum current magnitude. Lastly, it is important to mention that under EVA conditions, due to potential higher flushing capabilities of the lagoon, the amount of sargassum captured in front of the barrier is assumed to be negligible.

Table 3.4: EVA maximum hydrodynamic output at the location of barrier 1 & 2

Location	Barrier 1 (46,110)	Barrier 2 (52,259)	Barrier 2 (56,289)
H_s (m)	1.19	0.73	0.57
Tp (s)	7.36	9.11	5.03
Current (m/s)	0.37	0.60	1.06
Direction relative to barrier	66.84°	76.82°	39.60°
Current orientation	South West	East	South West

4
Barrier design

Designing an effective floating sargassum barrier at Puerto Morelos requires careful consideration of both environmental and operational site conditions. This Chapter outlines the key factors that influence the performance of such barriers by exploring how a floating barrier is optimally designed and constructed to effectively capture sargassum while minimising environmental impact. The Chapter addresses existing barrier designs, material selection and practical considerations for the local environment. Section 4.1 compares the different types of floating barriers currently in use for sargassum collection and their strengths and weaknesses are evaluated. In Section 4.2, different anchoring mechanisms are discussed based on functionality and strength. Section 4.3 examines materials based on their ability to resist marine conditions such as ultraviolet (UV) degradation, saltwater corrosion and biofouling. Common materials like high-density polyethylene (HDPE), Polyvinyl Chloride (PVC) and Galvanised steel are assessed for their mechanical properties under these conditions. Finally, in Section 4.5, all design choices are considered to ensure the barrier remains functional in the marine environment of Puerto Morelos. These choices include design, material, disassembling and repairing features and marine life considerations. By analysing these factors, this Chapter provides a framework for designing a floating barrier tailored to the conditions of Puerto Morelos.

4.1. Existing barrier designs

Over the last years, hotels and local governments have implemented various floating barrier designs to manage the sargassum stranding on their beaches. These designs were developed through trial and error. Despite significant investments, these methods lack scientific foundations and are not optimised for the specific conditions at Puerto Morelos. Barriers struggle to perform under changing wave forces and currents, requiring frequent maintenance and offering limited long-term success.[51][10] To determine the most suitable barrier for the Puerto Morelos area, this section compares the various types of barriers currently in use, evaluating their strengths and weaknesses under local conditions.

Several companies producing sargassum barriers have backgrounds in oil spill containment and many design principles have been adapted from these solutions.[3][22][25][35] The design of these sargassum barriers has, in part, been adapted from oil spill barriers. However, a key difference lies in the design properties. Oil containment barriers are made from solid, impermeable materials, whereas sargassum barriers are permeable to ensure water flows through the barriers while the sargassum is trapped. While most of the barriers have so-called mesh skirts with 3 mm holes in them, so sea turtles and sargassum can not get tangled in the barrier[36], other barrier producers claim that sea turtles and sargassum do not get tangled, even when nets with bigger holes are deployed.[51] However, there is no validated scientific research to back-up the claims. Based on field observations, expert opinions and research, four main types of sargassum barriers are identified. In this report, these are referred to as type I, type II, type III and type IV barriers. The barrier types are described in Section 4.1.1, Section 4.1.2, Section 4.1.3 and Section 4.1.4 respectively.

Figure 4.1: (a) Picture of type I barrier [4], (b) Picture of type II barrier [63], (c) picture of type III barrier [23], picture of type III barrier (d), (e) picture of submerged type I barrier[4], (f) picture of submerged type II barrier[58], (g) picture of submerged type III barrier[23], (h) picture of submerged type IV barrier[37].

4.1.1. Type I barrier

The type I barrier, shown in Figure 4.1 (a), consists of two parts: a floating cushion for buoyancy and a mesh skirt to prevent sargassum from passing underneath. The cushions are designed of PVC-coated, closed-cell, polyurethane (PU) foam logs, which offer buoyancy and protection from UV radiation.[23] The barriers exist in various dimensions, allowing customisation to accommodate different sargassum loads in diverse locations.[4]

As shown in Figure 4.1 (e), when type I barriers are deployed in a chain, they can cover large stretches at the surface of the water. The barrier section consists of 30-meter segments, which can be taken out individually. This feature simplifies maintenance and ensures the barrier remains functional even if a section requires repair. Type I barriers are typically used in shallow coastal regions due to their compact size and efficient deployment in reef-protected waters. Lastly, type I barriers are relatively affordable, as they share similarities with ocean-going oil booms, with the primary difference being the modified barrier draft attached to capture sargassum. According to Enviro-USA[33], type I barriers reduce the amount of sargassum reaching the beach by 85%. This claim however is not backed with scientific evidence, although other experts and observations agree that the type I barrier is not 100% effective.[51]

4.1.2. Type II barrier

As seen in Figure 4.1 (b), type II barriers have a different buoyancy design compared to types I and III barriers. Instead of a cushion on top, type II barriers use PU-filled, HDPE buoys woven through the mesh skirt structure. This buoy system makes the barrier more flexible and adaptable to fluctuating water conditions, as it allows the barrier to adjust more fluidly to waves and currents. The mesh skirt design also ensures that water can flow through while trapping the sargassum the same way as the type I barriers do.[23][48]

Figure 4.1 (f) shows that type II barriers are deployed in the same chain-linked way as type I barriers, with segments ranging from 25 to 50 meters in length.[63] Like type I barriers, type II segments are designed for easy detachment and replacement, which allows for easy maintenance and the possibility to quickly swap out sections when necessary. Type II barriers are particularly suited for coastal, reef-protected, environments where more adaptable barriers are required, due to the design providing a balance between buoyancy and flexibility. Moreover, these barriers are compact when transported and relatively inexpensive due to the affordable and widely accessible materials used in their construction.[23] Beach Bouncer[10] claims that the barrier is 100% effective, ensuring that no sargassum passes through. However, the company provides no supporting data and no scientific studies are available to verify this claim.

4.1.3. Type III barrier

type III barriers have a similar design to type I and IV barriers, as shown in Figure 4.1 (c), with a mesh skirt attached to floating materials. However, instead of a soft cushion filled with air or foam, the floating material consists of a double-walled, foam-filled, HDPE tube, ranging from 3 to 6 meters in diameter. These barriers form heavy-duty booms that are connected with rugged hardware, designed to reduce drag and strain on the system while effectively capturing both floating and submerged debris. Although effective in calm, unprotected waters, type III barriers are significantly more expensive due to their size and the inclusion of a steel channel running through the structural elements for added strength and durability. This construction allows them to withstand stronger environmental forces compared to other barrier types.[23]

Figure 4.1 (g) illustrates that type III barriers are deployed in larger segments, with variable lengths, as each segment can be independently deployed or removed. Their heavy-duty design makes them suitable for relatively calm but exposed waters, where additional strength is required. This added strength also contributes to their longevity. However, due to their buoyancy, type III barriers necessitate heavier anchoring, which increases the costs of anchoring and maintenance. Type III barriers can withstand wave heights of up to 1.20 m and currents of up to 0.8 $\mathrm{m/s}$.[10] Beyond these conditions, excessive stress may be placed on the connections and moorings due to their buoyancy. As a result, they are not recommended for deployment in areas with heavy wave action or breaking waves. According to Beach Bouncer[10], type III barriers completely blocks all sargassum with a 100% effectiveness rate, though the company has not provided any data, nor is there any known scientific research to support this.

4.1.4. Type IV barrier

The type IV barrier, illustrated in Figure 4.1 (d), is distinct from the other designs as it uses a PVC air-filled balloon for flotation instead of foam or hard plastic components. This feature makes the barrier lightweight and easy to deploy, as well as low volume when transported. Unlike the previous types, type IV uses nets instead of mesh skirts. This design reduces drag and inertia significantly, as the water can flow freely through the barrier. This lower drag results in reduced forces on the barrier and thus the moorings, meaning the barrier can be designed with less structural reinforcement since it experiences less stress. Still, using air-filled structures, this type of barrier can suffer from puncture.

Due to its light structure, type IV barriers are moored every two meters, ensuring stability in dynamic marine environments. However, since anchoring is the most dominant factor in terms of costs, overall costs significantly

increase.[10] Although nets are used, the designers claim that no marine life, such as sea turtles or the sargassum itself, becomes entangled in the system and no sargassum passes through the barrier. However, the designer can not back these claims with scientific research. The lack of a mesh skirt and instead using nets simplify the design and reduce structural needs. The type IV barrier is particularly suited for shallow coastal areas with low to moderate wave action.[51]

4.1.5. Design Failure

Regular maintenance is essential to ensure the effectiveness and longevity of all barrier types. Cleaning the barriers to remove marine growth, such as algae and barnacles, is crucial, as biofouling affects buoyancy and reduces UV resistance over time. The barriers are not designed to withstand extreme weather events like storms or hurricanes, which impose forces beyond their capacity. Different companies report varying lifespans for similar designs, with Abasco estimating 3-5 years[39], while others claim lifespans of 10[51] to 15 years[10]. Human factors, however, are the main reason for barrier dysfunction. Negligence decreases the real lifespan of the barrier drastically, for further details refer to Section E.1.1.

4.1.6. Pros and Cons of Different Barrier Designs

Each sargassum barrier design has its advantages and challenges, depending on factors like buoyancy, durability, ease of maintenance and adaptability to different marine environments. Some barriers perform well in high-energy conditions, while others are more suitable for calm or shallow waters. A detailed comparison is provided in Table E.1, but this section summarizes the key strengths and weaknesses of each design. Selecting the most appropriate barrier depends on balancing these factors to meet the specific needs of coastal areas.

Type I

+ Well-known design from the oil spill containment industry
- Only applicable in protected waters
- 85% sargassum reduce

Type II

+ High flexibility
+ Low shipping volume
- Untreated HDPE buoys not suitable for high UV conditions
- Only applicable in protected waters

Type III

+ Applicable in unprotected waters
+ Individually replaceable
- High shipping volume
- Heavy duty anchoring required
- Low flexibility

Type IV

+ Inexpensive design
+ Extreme low shipping volume
- Frequent anchoring
- Possibility of puncture
- Usage of controversial nets

4.2. Anchoring

All types of sargassum barriers require effective anchoring systems to maintain their stability and performance, particularly in fluctuating water conditions. The anchoring process is crucial for the effectiveness of the barrier and the most dominant factor in terms of cost.[10] In this section two types of anchoring are discussed and evaluated based on their features and properties: The direct anchor system and the anchor buoy system are presented in Figure 4.2 and Figure 4.3 respectively. Both systems can be modified by connecting the barrier to an additional anchoring point at the opposite site of the original anchor, providing greater positional stability in response to changing wave or current directions. The mooring lines are mostly made of nylon, due to its excellent shock absorption and durability, as explained in Section E.2.

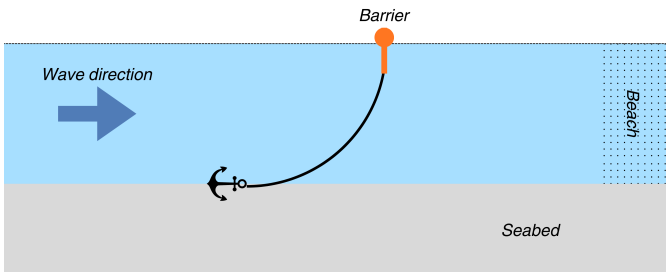

Figure 4.2: Schematic of the Direct Anchor System.

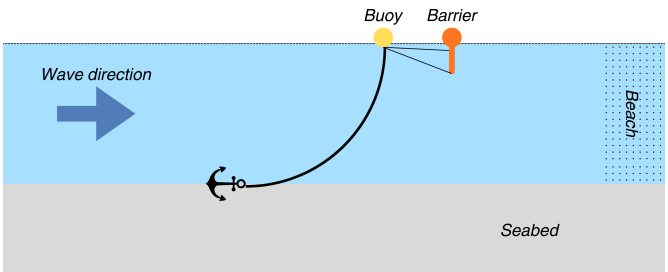

Figure 4.3: Schematic of the Anchor Buoy System.

4.2.1. Direct Anchor System

The direct anchor system is a simpler, more traditional approach, where the barrier is directly connected to an anchor on the seabed. This system involves fewer components, making it more straightforward to deploy and maintain. The simplicity of the system offers a cost-effective solution, particularly in areas where the environmental conditions are stable and the barrier is not exposed to significant wave action or strong currents.

The direct connection between the anchor and the barrier offers better control over the positioning of the barrier, ensuring that it remains fixed in place. When the barriers are detached, a replacement buoy should be attached to the mooring to simplify locating the lines for future reattachment.

4.2.2. Anchor buoy system

The anchor buoy system adds an intermediary buoy between the anchor on the seabed and the floating barrier. The buoy helps lift the mooring line, reducing the strain on the barrier and allowing for more flexibility in response to wave movement. When using the anchor buoy system the need for anchoring points to the seabed could be reduced by connecting the anchor buoy to multiple places to the barrier using different lengths of mooring lines from the buoy to the barrier as shown in Figure 4.4.

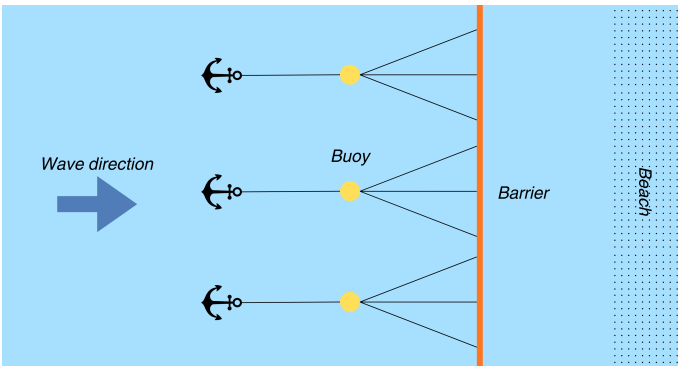

Figure 4.4: Schematic of possible configuration using anchor buoy system (from above).

The barrier can be attached at one or two points in this system, which further distributes the forces exerted on the barrier and helps maintain its shape. This system is particularly useful in areas where water conditions can vary significantly, such as regions with moderate wave action or shifting currents.

This system, however, is not included in the structural model described in Chapter 5, as the concept of multiple mooring lines connected from the barrier to an anchoring buoy emerged later in the research process and could no longer be integrated into the model.

Additionally, the anchoring buoy system allows for easy detachment of the barrier. This feature is particularly useful in situations where the barrier needs to be quickly removed or re-positioned, such as during extreme weather events or when maintenance is required.

4.2.3. Seabed attachment

There are three primary methods for attaching moorings to the seabed and the choice of method depends on the properties of the seafloor. When the seafloor consists of sand, an anchor (often Danforth-style fluke anchors[49]) can be used to secure the barrier. In cases where there is a thin layer of sand or the seafloor is predominantly rock, a hole can be drilled into the rock and a pin with a ring is inserted to create a stable attachment point using epoxy to bind together. This method is also used on reefs where the rock is exposed. A third option is to place a large concrete block on the seabed to anchor the mooring. However, this method can significantly impact marine life and the surrounding ecosystem by disturbing the ocean floor.

Using concrete blocks is the most cost-effective method for anchoring the barrier. Additionally, it provides more certainty in calculations regarding the forces it can withstand. Drilling into porous rock and securing pins with binding materials introduces complexity, making it difficult to guarantee how much force this method can reliably support, however, it reduces the impact on the ecological system significantly.

4.2.4. Design failure

The anchoring systems securing the barriers in place need periodic inspection and maintenance to ensure stability and effectiveness. As explained in Section 4.1.5 the most common reason for dysfunctioning of the barrier is caused by complications induced by humans.[51] For further explanation, refer to Section E.1.2.

4.2.5. Pros and cons of different anchoring systems

This section outlines the pros and cons of the different anchoring systems used for sargassum barriers. Each system has unique advantages and limitations depending on factors such as installation complexity, cost and adaptability to wave action and currents. The following lists summarize the strengths and weaknesses of the direct anchor and anchor buoy systems, helping to identify the most appropriate solution based on specific environmental and operational requirements.

Direct anchor system

+ Simple and easy to install
+ Cost-effective due to fewer components
- Vulnerable to strong waves and currents
- Less adaptable to changing environmental conditions

Anchor buoy system

+ Reduces vertical strain on the barrier
+ Helping the barrier maintain its shape using fewer anchoring points
+ Allows for easy detachment and repositioning
- Higher installation costs

4.3. Materials

Some material choices for sargassum barriers are sub-optimal given the harsh marine conditions they face. As discussed in Section 4.1.6, different barrier designs utilise a variety of materials with varying performance characteristics. Appendix E evaluates the commonly used materials in sargassum barrier construction, focusing on density, UV resistance, impact resistance and cost. This section summarises the main findings.

4.3.1. Polyethylene

HDPE was chosen for key barrier components, such as buoys and floating tubes, due to its excellent buoyancy, tensile strength and chemical resistance in marine environments. The ability of HDPE to withstand UV degradation with proper stabilisers makes it a suitable choice for long-term exposure to sunlight, which is critical in tropical regions.

- The low density of HDPE ensures sufficient buoyancy (0.94–0.97 $\mathrm{g/cm^3}$), while its impact resistance (20 $\mathrm{J/m}$ for stabilised HDPE) helps the barrier withstand physical forces from waves and debris.
- UV stabilisation is essential in environments like Puerto Morelos, where intense sunlight accelerates material degradation. HDPE can be treated with UV stabilizers to improve its resistance.

For a detailed analysis of the molecular structure of HDPE, mechanical properties and UV resistance mechanisms, see Section E.3.

4.3.2. Polyvinyl Chloride

PVC is another key material, particularly used in the mesh skirts of the barrier. While PVC is heavier than water (density: 1.3–1.7 $\mathrm{g/cm^3}$), its flexibility, chemical resistance and low cost make it an ideal choice for the submerged components of the barrier.

- Unplasticised PVC (uPVC) provides rigidity and strength, making it suitable for structural parts that need to resist wear and abrasion.
- Plasticised PVC (pPVC) offers flexibility, which is beneficial for parts exposed to wave movement.
- UV inhibitors can stabilize PVC well in high-UV environments of Puerto Morelos

For more detailed material properties and performance analysis of PVC, including molecular structure and UV degradation, refer to Section E.4.

4.3.3. Galvanised Steel

The anchoring components and connections between barrier segments rely on galvanised steel, which provides the necessary strength and durability for these critical load-bearing elements. However, since steel is prone to corrosion in marine environments, galvanisation offers a protective zinc coating that prevents rust formation. The specific corrosion mechanisms and detailed discussion on the galvanisation process are provided in Section E.5.

After evaluating the mechanical properties and environmental resistance of these materials, HDPE and PVC were selected as the primary materials for the barrier components. Galvanised steel is used for the strength throughout the barrier assuring its load-bearing capacity, with a protective PVC to ensure longevity in saltwater conditions.

4.4. Possible improvements

This reflects on the various barrier designs and material choices discussed earlier and identifies areas where improvements can be made. By analysing the strengths and weaknesses of each design, this section aims to suggest enhancements that can increase the overall effectiveness, durability and environmental compatibility of the barriers. These recommendations focus on optimising performance under the conditions at Puerto Morelos.

4.4.1. PMMA

Polymethyl methacrylate (PMMA) is a versatile, transparent thermoplastic widely used as a lightweight and shatter-resistant alternative to glass. As seen in Figure 4.5, PMMA is a polymer derived from the methyl methacrylate (MMA) monomer, with a structure that imparts both optical clarity and excellent chemical resistance. The key properties of PMMA, including impact strength, chemical resistance and UV resistance, make it an ideal candidate for marine applications. However, it is yet not utilised in any existing designs.

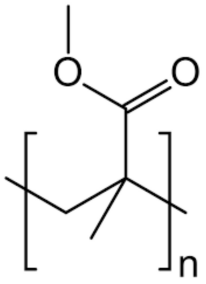

Figure 4.5: Molecule structure of PMMA.

Application of PMMA on floating barriers

With a density of 1.18 $\mathrm{g/cm^3}$, PMMA is heavier than water, requiring additional buoyancy aids such as foam inserts, similar to the design considerations for PVC barriers (see Section E.4).[8] PMMA exhibits excellent tensile strength and is known for its rigidity and impact resistance, making it one of the hardest thermoplastics. It resists shattering upon rupture, which is beneficial for structures exposed to environmental forces in marine settings. However, its brittleness under high-stress conditions limits its use in high-impact areas, where more flexible materials like HDPE or pPVC may be preferable.

Due to the stability of HDPE and PVC, these polymers are challenging to recycle. However, thermal degradation of PMMA allows up to 90% of the original MMA molecule to be recovered[55]. This makes PMMA buoys a more sustainable option, as they can be recycled at the end of the lifespan of the barrier. However, compared to the materials described in Section 4.3, PMMA is more than two and a half times as expensive. This can be seen in Table 4.1.

Table 4.1: Prices common polymers used in barriers according to Chemanalyst.

Polymer	Cost ($/mt)	Source
HDPE	1301	[34]
PVC	813	[53]
PMMA	3502	[54]

UV resistance

The biggest beneficial property of PMMA is its high resistance to UV degradation, which is a critical feature in outdoor applications exposed to sunlight. Unlike other polymers that require UV stabilizers, PMMA maintains its structural integrity even after prolonged exposure to UV radiation. This makes it a reliable choice for marine structures that endure intense sunlight.[8][19]

4.4.2. Antifouling applications

Biofouling, the accumulation of marine organisms such as algae and barnacles on submerged structures, could pose a challenge for floating barriers. Biofouling can degrade materials, reduce buoyancy and increase drag, resulting in raising maintenance costs and decreasing the longevity of the barrier.[64] To counter these effects, one can manually clean the barriers during maintenance or antifouling coatings can be applied to the barrier surfaces to prevent the attachment and growth of these organisms. However, established antifouling agents are not effective in one-year tests.[10] Recently, a new innovative solution of antifouling has emerged: nanocoatings. These coatings not only inhibit biofouling but also enhance the overall durability of the materials they are applied to, thereby reducing operational costs and extending the life of barriers.

Nanocoatings

Nanocoatings work by forming a very thin, protective layer on the surface of the barrier materials. This layer, typically only 1 to 100 nanometers thick, alters the surface properties of the material, making it less hospitable to marine organisms. By preventing the settlement of these organisms, the coatings reduce the need for frequent cleaning and maintenance, ensuring the barrier performs optimally over a longer period.[38] Nanocoatings use key principles

such as hydrophobicity and low surface energy to improve the durability of materials exposed to marine environments.

The superhydrophobic properties of nanomaterials create surfaces with contact angles, explained in Section E.6, greater than 150°. This means that water droplets bead up and roll off, carrying away dirt, salt and potential biofouling organisms in the process. This self-cleaning effect keeps the surface free from contaminants, further minimising maintenance efforts. Nanocoatings with low surface energy also minimise the ability of biological organisms to adhere. They achieve this by incorporating materials with antibiotic properties, or through physical mechanisms like smooth surfaces that reduce the ability of marine organisms to adhere. The cost of applying nanocoatings is relatively low compared to the long-term savings achieved through reduced maintenance and extended barrier lifespan. Lab studies demonstrate their antifouling potential by inhibiting the growth of organisms like algae and barnacles. However, the long-term durability and macro-scale application of these coatings under constant exposure to complex marine conditions remains an area needing further research and field validation.[38]

Silica nanocoatings

Silica coatings, a specific type of nanocoating, have proven to be highly effective in antifouling applications. The silica nanoparticles form a dense, uniform layer that provides a smooth, hydrophobic surface. This repels water, making it difficult for organisms to adhere to the material. The low surface energy of silica disrupts the ability of microorganisms, algae and barnacles to settle and grow, minimising biofouling and the associated wear and tear on the barrier.

In addition to biofouling prevention, silica coatings offer enhanced resistance to UV radiation and wear down. By applying silica coatings, the lifespan of sargassum barriers can be significantly extended, reducing the frequency of replacements and repairs. Furthermore, a key benefit of silica coatings is their environmental friendliness. Unlike traditional antifouling treatments that rely on toxic chemicals, silica coatings do not leach harmful substances into the water. This makes them a more sustainable option for protecting marine infrastructure, supporting both environmental preservation and long-term cost savings. The use of silica coatings could provide a durable, low-maintenance solution, ideal for maintaining the functionality and longevity of floating sargassum barriers in challenging marine environments. However, more research should be conducted on its effectiveness.[18]

4.5. Design Puerto Morelos

This section focuses on the specific conditions of Puerto Morelos, which play a critical role in determining the appropriate barrier design. First, the stakeholder interplay is explained in Section 4.5.1. Then, in Section 4.5.2, the unique environmental factors of the area are outlined. Lastly, in Section 4.5.3, a tailored barrier design is developed to meet these specific conditions, ensuring effective sargassum management while maintaining the integrity of the local marine ecosystem. The final design aims to address these challenges with an optimised solution.

4.5.1. Stakeholder interplay

The design and implementation of a sargassum barrier at Puerto Morelos are influenced by the interests and requirements of the stakeholders presented in Table A.1, each with unique perspectives on sargassum management. These stakeholders play critical roles in shaping the final design and operational approach of the barrier system. Their power is plotted against their interest in Figure A.1, representing the level of engagement each stakeholder requires.

University ENES, as a primary knowledge provider, holds significant influence over the scientific and technical foundation of the project, despite being in a lower-power position overall. Their academic interest in a scientifically sound methodology means they provide essential research and analysis but rely on other stakeholders for funding and implementation. Furthermore, their interest lies in ecological preservation, more than in the benefits for recreational users of the area.

Stakeholders in the tourism and recreational sector, particularly hotels, have a high interest in sargassum management; however, only hotels hold significant power. While both groups are heavily impacted by sargassum and rely on effective management, hotel-driven solutions may not benefit local recreational users. Therefore, a cost-effective and adaptable solution is proposed to serve all stakeholders. Successful sargassum management aligns with their objectives, making their engagement essential to project success.

The fishing industry and environmental NGOs have, similar to the recreational users, high interest but low power. However, they are vital in ensuring that the project respects ecological sustainability. Their focus on marine conservation and minimal disruption to ecosystems necessitates regular updates and transparency to gain their support and prevent opposition. Engaging these stakeholders helps align the design of the barrier with long-term sustainability and community acceptance.

Overall, the success of the sargassum barrier project at Puerto Morelos relies heavily on the financial aid of the hotel industry and the political support of government and local parties, informed by research by ENES. By consulting with environmental groups and the fishing industry, the project can ensure that its design respects both ecological integrity and local economic needs.

4.5.2. Design conditions Puerto Morelos

In this section the design conditions of Puerto Morelos are explained. Using the requirements described in this section, together with the properties of Section 4.1, Section 4.3 and Section 4.4 a well-substantiated choice of design can be made, tailored to the conditions of Puerto Morelos.

Physical properties

Barriers have to physically withstand the hydrodynamic conditions of the Puerto Morelos area, as described in Section 3.4. From the results of Section 3.2, the optimal location for the floating barrier is found. At this location, data from observation points provide the significant wave height, peak period and maximum current velocities, which are essential for determining the forces the barrier must withstand. This is done in Section 6.2. In Table 3.4 the resulting current velocities, peak period and significant wave heights for the barrier at the three most dominant locations are given.

Marine Life

The reef in front of the beaches of Puerto Morelos is part of the 1000 km long Mesoamerican Reef, which is home to a diverse range of marine life, including octocorals, sponges, black corals, calcareous macroalgae, various fish species and sea turtles.[32][60] Specifically, the reef is located within the northern sector of the Mesoamerican Barrier Reef System (nsMBRS). Marine life in Puerto Morelos has suffered significantly from the heavy influxes of sargassum that began arriving in 2018 and 2019, as illustrated in Figure E.7 provided by the Moon Palace.[50] However, there have been signs of recovery in certain parts of the ecosystem in recent years, offering hope for the restoration of the reef and its associated marine communities.

The arrival of large amounts of sargassum still poses significant challenges for marine life, particularly affecting seagrass, fish, sea turtles and corals. The accumulation of sargassum on the surface of the water blocks sunlight from reaching seagrasses and corals, which rely on light for photosynthesis. This reduction in light availability negatively impacts these species, leading to potential declines in their populations.[46] Additionally, on the beaches, the piled-up algae obstruct sea turtles from reaching nesting sites, making it difficult for them to lay eggs. It also obstructs the ability of baby turtles to safely make their way from the shore to open water.

Additionally, the presence of sargassum affects the coral reef ecosystem. Combined with other disturbances such as coral bleaching and hurricanes, the excessive sargassum can shift the ecosystem from a healthy coral-dominated state to one dominated by macroalgae, further stressing the reef environment.[45] The ocean floor in front of the coast of Puerto Morelos consists of a thin layer of sand over a rock base, while the reef is composed of rock overgrown by coral, making it essential to minimize disturbance during any intervention.[74]

To conclude, when designing a sargassum barrier, it is crucial to ensure that marine life, including fish and sea turtles, is not disturbed. Additionally, the anchoring system should avoid damaging sensitive ecosystems such as coral reefs and seagrass beds to maintain environmental integrity.

Disassembly and adjustments

Barriers must be designed to be disassembled, as they need to be removed from the water during extreme weather conditions, including hurricanes. These severe events can exert excessive force on the barriers, potentially leading to significant damage if they are left in place. Since hurricanes are often forecasted several days in advance, the operation to remove the barrier can be well-planned and executed on time. As discussed in Section 2.2.3, hurricanes and similar extreme conditions occur almost annually (with 9 events recorded in the last 10 years). Given the infrequency of these events, it is not practical to over-engineer the barriers to withstand such rare occurrences. Instead, designing the barriers to be quickly and efficiently disassembled offers a more cost-effective and practical solution. Additionally, the high wave energy and tidal forces during hurricanes naturally flush the reef lagoon in Puerto Morelos, which helps maintain the ecosystem by removing debris.[61]

Furthermore, maintenance and cleaning are essential for the longevity and functionality of the barriers and the ability to disassemble them simplifies this process. In certain conditions, it may be necessary to adjust the orientation of the barriers to better protect the coastline in certain weather conditions. This adaptability ensures that the barriers can be reoriented based on weather conditions, maximising their effectiveness.

4.5.3. Final design for Puerto Morelos

In this section, the key properties and design requirements for a sargassum barrier tailored to the conditions of Puerto Morelos are presented. The final design incorporates a hybrid approach, integrating features from existing barrier

types combined with an anchoring system to achieve optimal performance. Each design choice has been validated based on site-specific conditions, including wave forces, currents and mooring limitations. The analysis takes into account factors such as barrier strength, flexibility and allowable deflection, ensuring that the structure meets the necessary criteria for durability and efficiency in sargassum containment while minimising environmental impact.

Barrier design

There are four barrier designs described in Section 4.1, each with its advantages and disadvantages. In this section, the pros and cons of each design are weighted to determine which barrier type is best suited for the Puerto Morelos area.

Barrier type I only catches or deflects around 85% of the sargassum, which falls short of the goal of capturing 100%. Given the high influx of sargassum in the Puerto Morelos area, particularly during peak seasons, it is essential to maximize efficiency and containment. While type I barriers are cost-effective and easy to maintain, their limited ability to capture all sargassum makes them unsuitable.

Barrier type II, on the other hand, presents a very suitable option for the conditions at Puerto Morelos. Its flexible design allows it to adapt easily to varying current conditions and directions, as well as easy deployment and taking in. This makes the type II barrier highly compatible with both the direct and indirect anchoring configurations planned for the site. The HDPE buoys used in this design are lightweight and durable, providing sufficient buoyancy without adding excessive strain to the anchoring system. Additionally, treating the HDPE buoys with UV stabilizers enhances their longevity in the high UV environment of Puerto Morelos. Moreover, the low shipping volume makes it easy to handle them and store them when they are not deployed.

Barrier type III is less suitable for this project due to its heavy anchoring requirements. The significant weight and size of the barrier demand a robust anchoring system. The anchoring is the dominant factor in terms of cost, especially because concrete blocks cannot be used in the Puerto Morelos area due to the sensitive marine life and the potential damage they could cause to the reef. The additional expense of the heavier-duty anchoring and maintenance requirements makes Barrier type III impractical for the conditions of Puerto Morelos.

Similarly, Barrier type IV requires frequent anchoring points (every two meters) to maintain its shape, which increases both installation and operational costs, particularly because concrete blocks cannot be used. The reliance on nets also raises concerns about the potential entanglement of marine life, such as sea turtles. However, by replacing the nets with the same mesh grids used in other barriers and reinforcing the structure to reduce the need for frequent anchoring, it becomes possible to adapt Barrier type IV for use in the Puerto Morelos area. Without these crucial adaptations, however, Barrier type IV remains a less favourable option. A solution with fewer anchoring points is still preferred to minimize environmental disruption.

Anchoring strategy

A reliable and long-lasting solution is essential for anchoring a barrier in the Puerto Morelos area. Therefore, the indirect anchoring strategy is recommended. This strategy, described in Section 4.2.2 uses anchor buoys attached to the seabed. First, this method allows the barrier to adapt to varying wind directions, enabling flexibility to close the barrier on the north or south side of the lagoon. Secondly, the anchor buoy system simplifies the process of removing the barrier in case of storms or hurricanes, as well as when maintenance is needed. Finally, the buoyancy requirements of the barrier itself are reduced, as the anchor buoys bear the strain, lifting the mooring rather than relying on the barrier's buoyancy. This combination of factors makes the anchor buoy system an efficient and adaptable choice for long-term deployment. The initial costs of this system are higher because of the use of more materials. Still, by reducing the complications when removing and reattaching the barrier, the long-term operational costs are significantly lowered, making it a cost-effective solution over time.

For attaching the moorings to the seabed, drilling holes in the rock and using pins for anchoring is recommended. Since the reef consists primarily of rock or rock covered by a thin layer of sand. This method, as described in Section 4.2.3, offers a stable and reliable anchoring solution while minimising environmental impact. By avoiding the use of large concrete blocks, which could significantly disturb the sensitive marine ecosystem, the pin-based anchoring system ensures that the barrier can be secured without harming the reef. Lastly, using the anchor buoy system reduces the need for anchoring points to the seabed, when connecting the anchor buoy to multiple places to the barrier using different lengths of mooring lines from the buoy to the barrier as shown in Figure 4.4. Overall, this design offers an effective solution for capturing sargassum while minimising disruption to the local ecosystem, balancing practical operational needs with ecological preservation.

To balance the need for reef protection to achieve a cost-effective solution, the number of anchoring points is minimised while ensuring that the barrier maintains its intended shape. By making strategic choices in the barrier design, such as optimising the positioning and flexibility of the segments, it is possible to reduce the frequency of anchor

points. This approach not only reduces environmental disturbance to the reef but also lowers installation and maintenance costs.

Maintenance

Based on the evaluation in Section 4.4.2, nanocoatings are not ready yet to be incorporated into the final design to improve durability and reduce biofouling. Still, the lifespan of the barriers can be extended by regularly carrying out maintenance to ensure the long-term effectiveness and structural integrity of the barrier.

To avoid damage during extreme weather events, the barrier should be removed from the water when the H_s and T_p exceed the thresholds specified in Section 3.4. This measure helps prevent structural failure from forces beyond the limits of the barrier design. It is recommended to remove the barrier for routine maintenance when no sargassum arrivals are forecasted. Once the barrier is out of the water, the steps described in Section 10.1 should be carried out.

By following these maintenance procedures, the barrier remains effective in capturing sargassum while minimising operational costs. Regular maintenance, combined with the possible use of advanced nanocoatings in the future, assures the longevity of the barrier system under the marine conditions of Puerto Morelos.

Input for structural model

The final design for the sargassum barrier is based on a type II barrier. However, several design modifications are necessary to ensure optimal performance under the Puerto Morelos conditions. These adjustments, involve refining the dimensions, material thickness and structural strength to meet the environmental challenges described in Section 3.4. Figure 4.6 presents a schematic view of the front and side profiles of the final barrier design, illustrating the proposed structure and its critical dimensions, as shown in Table 4.2. This section elaborates on the design choices and how they are affecting the structural model in Chapter 5.

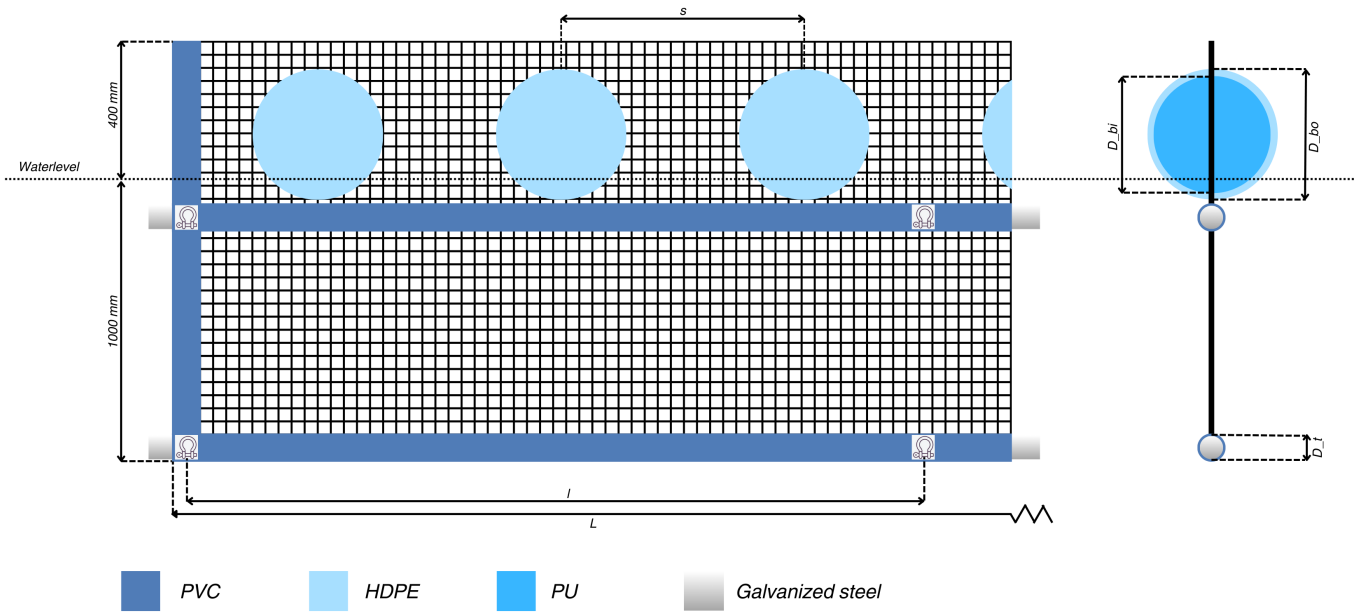

Figure 4.6: Schematic of front view barrier (left) and side view barrier (right).

Table 4.2: Dimensions Puerto Morelos barrier

Symbol	Variable
s	Distance between buoys
l	Distance between mooring lines
L	Length barrier segment
D_{bo}	Outer diameter buoy
D_{bi}	Inner diameter buoy
D_t	Diameter of the tension cable

The barrier consists of a pPVC woven mesh grid with 3 mm holes, this mesh grid is submerged (draft) for 1000 mm and sticks 400 mm out of the water (freeboard) to prevent sargassum from going over. Every s meter, two half-round HDPE, UV stabilised, buoys filled with PU foam (density ranges from 40 to 60 $\mathrm{g/cm^3}$) are placed. Galvanised steel is used for the barrier's cables and shackles, with PVC hoses and galvanisation providing the primary corrosion protection. To mitigate potential CRS effects, regular maintenance and inspection are advised, ensuring the integrity of

the cables over time. The diameter of two galvanised steel cables determines the tensile strength and axial stiffness of the barrier. The cable is also the ballast preventing the barrier from losing its vertical shape. With galvanised steel shackles the segments are connected at both cables to the next barrier segment.

5 Structural model

This chapter presents the model that describes the behaviour of a floating sargassum-catching barrier on the sea surface. First, an overview of the model is provided in Section 5.1, where the underlying assumptions, governing equations, boundary and interface conditions are discussed. Next, Section 5.2 covers the mooring lines of the structure. Following that, Section 5.3 focuses on the structural loading acting on the barrier. In Section 5.4, the Finite Element Method (FEM) used to solve the governing equations is explained. Finally, Section 5.5 outlines the calculations for the vertical stability of the floating barrier. Together, these sections provide a basis for Chapter 6, which offers insights into the resulting stresses and deformations of a barrier structure when implemented in the Puerto Morelos area. By doing so, this chapter together with Chapter 6 answers the main structural research question posed in Section 1.3.

5.1. Model definition

To analyse the stresses and deformations of the barrier, a model is developed to evaluate its behaviour. While the model aims to closely simulate the actual performance of the barrier, it is never a perfect representation due to the necessary assumptions that need to be made. This section first addresses these assumptions, followed by a presentation of the governing equations of motion. Finally, the relevant boundary and interface conditions are explained.

5.1.1. Assumptions

First, it is assumed that the floating barrier behaves like a string, capable of extending in the longitudinal direction. This assumption aligns with the design, as the barrier cannot withstand any compressive forces or moments.

Second, the mooring lines supporting the floating barrier are modelled as string elements. Since these elements are situated in very shallow water, the line is short, thus the catenary shape of the lines is assumed to provide negligible stiffness to the system, As a result, the mooring lines only generate a restoring force when fully tensioned.

Third, since the forces are expected to come mainly from one direction, it is assumed that the mooring lines remain fully tensioned most of the time. The mooring lines are therefore preset with their maximum length and axial stiffness.

Lastly, two types of damping are considered: added mass and viscous damping. Added mass increases the inertia of an object moving through fluid by accounting for the displaced fluid and is included in the Morison equation, as discussed in Section 5.3.2. Viscous damping, on the other hand, resists the motion of the object, converting some kinetic energy into heat and thereby reducing the velocity of an object over time. This effect is directly incorporated into the FEM model.

5.1.2. Governing equations

The governing equations of motion are described in the coordinate system given in Figure 5.1.

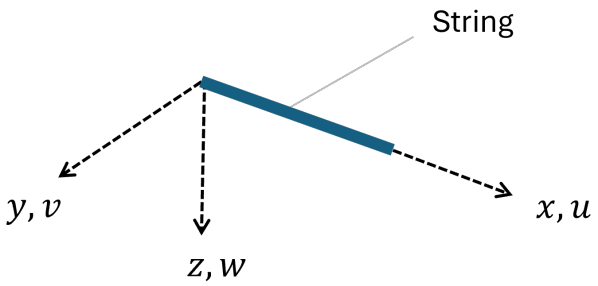

Figure 5.1: Reference system for the structural model.

The behaviour of the string is governed by two equations of motion. The first equation of motion describes the longitudinal displacement of the string (similar as the equation of motion of a rod). The equation is as follows:

$$\rho A \frac{\partial^2 u}{\partial t^2} + C_u \frac{\partial u}{\partial t} - \frac{\partial}{\partial x}\left(EA \frac{\partial u}{\partial x}\right) = f_u(x,t) \tag{5.1}$$

Where:

- $u(x,t)$ is the longitudinal displacement $[\mathrm{m}]$,
- E is the Young's modulus $[\mathrm{N/m^2}]$,
- ρ is the density $[\mathrm{kg/m^3}]$,
- A is the cross-sectional area $[\mathrm{m^2}]$,
- C_u is a damping factor $[\mathrm{kg/s \cdot m}]$,
- $f_u(x,t)$ is the external force in the longitudinal direction $[\mathrm{N/m}]$.

The second equation of motion describes the displacement of the string in transverse direction. This equation is given as follows:

$$\rho A \frac{d^2 v}{dt^2} + C_v \frac{\partial u}{\partial t} - T \frac{d^2 v}{dx^2} = f_v(x,t) \tag{5.2}$$

Where:

- $v(x,t)$ is the transverse displacement $[\mathrm{m}]$,
- ρ is the density $[\mathrm{kg/m^3}]$,
- A is the cross-sectional area $[\mathrm{m^2}]$,
- C_v is a damping factor $[\mathrm{kg/s \cdot m}]$,
- T is the tension present in the string $[\mathrm{N}]$,
- $f_v(x,t)$ is the external force in the transverse direction $[\mathrm{N/m}]$.

5.1.3. Boundary and interface conditions

The barrier structure is modelled as a string connected to mooring line elements. Each mooring line is attached to an anchor point. This anchor point is fixed in space and therefore forms a boundary conditions where both degrees of freedom are constrained. In addition, the mooring lines are treated as string elements but with a distinct EA

An example of a model structure is shown in Figure 5.2, where the barrier is supported by mooring lines at both ends and an additional mooring line at the midpoint. The red dots in the figure indicate the boundary points.

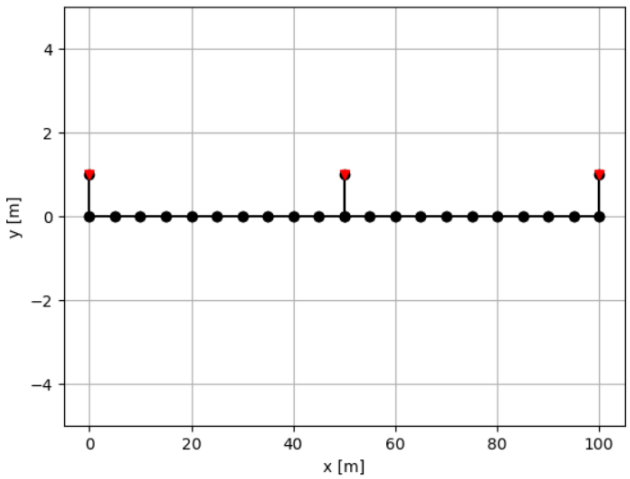

Figure 5.2: Simplified mesh grid structure that is used in the model.

5.2. Mooring lines

The mooring line stiffness is determined by both geometrical and elastic stiffness. The elastic stiffness comes from the material properties of the cable, while the geometrical stiffness results from changes in the geometry of the mooring line [26]. Mathematically, this reads:

$$k_{mooring} = k_{geometry} + k_{material} \tag{5.3}$$

To accurately model the behaviour of the mooring lines, it is essential to understand their functioning. Since the barrier is situated in relatively shallow water, the mooring lines do not form a catenary shape capable of generating

a restoring force without the use of an excessively long line. As a result, the mooring lines only generate a restoring force when they are fully stretched, implying that in Equation 5.3, $k_{geometry} \rightarrow 0$, because the geometry of the mooring line does not contribute to its stiffness. Consequently, $k_{material}$ equals the EA of the mooring line, but only when the displacement of the fairleads $u_{fairlead}$, which is the element that connects the barrier to the mooring line, relative to the anchoring point exceeds the length of the mooring line. At that point, the mooring line is under tension, and the stiffness is governed solely by $k_{material}$.
However, since the mooring lines exist in a 3-dimensional space, it is crucial to carefully evaluate when the displacement of the fairlead exceeds the length of the mooring line. Figure 5.3 illustrates the offset from its initial position in the y-direction.

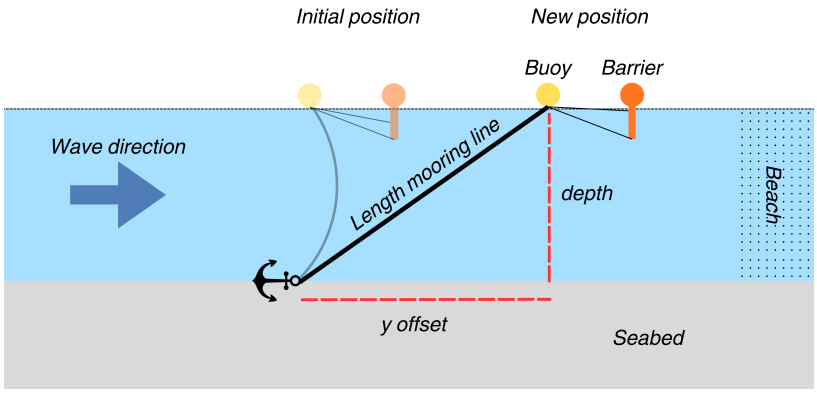

Figure 5.3: Offset in y-direction if the buoy is moving.

In this 2-dimensional representation, the length of the mooring line can be calculated using the Pythagorean theorem:

$$l_m^2 = v^2 + d_0^2 \tag{5.4}$$

Where:

- l_m is the length of the mooring line $[\mathrm{m}]$,
- v is the offset in y-direction $[\mathrm{m}]$,
- d_0 is the average water depth $[\mathrm{m}]$.

As the length of the mooring line and the depth are known beforehand, the offset in the y-direction can be calculated. This value is used to give the mooring lines a fixed length in the model but with a different EA.

5.3. Determining loading on the barrier

This section provides a detailed explanation of the forces acting on the structure. It begins by describing the generation of a wave spectrum, which is used to calculate particle velocities and accelerations. Then, it explains how these velocities and accelerations are applied in the Morison Equation to determine the time-varying forces exerted on the structure.

5.3.1. Generating the wave spectrum

To get an accurate representation of the sea states, a JONSWAP energy spectrum is generated based on T_p and H_s. The JONSWAP spectrum is widely used to represent realistic sea states, particularly in coastal and offshore environments. It provides a more accurate description of how wave energy is distributed across different frequencies in a given sea state. This allows one to assess how different components of the wave spectrum contribute to the total forces acting on the barrier.

The Marine and Hydrokinetic Toolkit (MHKiT) [2], an open-source software developed in Python, is used to generate a JONSWAP spectrum. As an input, it takes the aforementioned T_p and H_s. Additionally, the dt (time step) and n_s (number of time steps) can be adjusted.

The generated JONSWAP spectrum gives $S(f)$, which is the energy per unit frequency of the waves for different wave frequencies. This information can be used to relate the amplitude of the individual frequency components of waves by the following relation:

$$\sum_{f}^{f+\Delta f} \frac{1}{2} a_n^2 = S_n(f)\Delta f \tag{5.5}$$

The total power in a small frequency band $[f, f + \Delta f]$ is equal to the power spectral density $S_n(f)$ multiplied by the bandwidth Δf. The corresponding amplitude of the signal at that frequency is $a_n(f)$, and its squared value is related to the power. Rewriting allows one to compute the amplitude spectrum using:

$$a_n(f) = \sqrt{2S_n(f)\Delta f} \tag{5.6}$$

This spectrum gives the amplitude of the wave components at each frequency, which can then be used to reconstruct the time-domain wave elevation and particle velocities. The total wave elevation $\eta(t, x)$ at time t and position x is obtained by summing the contributions from all individual frequency components. Each frequency component contributes a sinusoidal oscillation to the overall wave field. The total wave elevation is expressed as:

$$\eta(t, x) = \sum_n a_n(f_n) \cos(2\pi f_n t - k_n x + \phi_n) \tag{5.7}$$

Where:

- f_n is the frequency of the n-th component $[\mathrm{Hz}]$,
- k_n is the corresponding wave number $[-]$, related to the wave frequency f_n by the dispersion relation,
- ϕ_n is the phase shift, which accounts for the initial position of the wave crest. Note that this is randomised.

By summing these sinusoidal components, a realistic representation of the time-varying surface elevation that accounts for waves of different frequencies is generated. The particle velocities are also determined by summing the contributions from each frequency component. The horizontal and vertical velocity components, $u(t, x, z)$ and $w(t, x, z)$, at a depth z are given by:

$$u(t, x, z) = \sum_n a_n(f_n)\omega_n \frac{\cosh(k_n(z + d))}{\sinh(k_n d)} \cos(2\pi f_n t - k_n x + \phi_n) \tag{5.8}$$

$$w(t, x, z) = \sum_n a_n(f_n)\omega_n \frac{\sinh(k_n(z + d))}{\sinh(k_n d)} \sin(2\pi f_n t - k_n x + \phi_n) \tag{5.9}$$

Where:

- $\omega_n = 2\pi f_n$ is the angular frequency in $[\mathrm{rad/s}]$,
- d is the average water depth in $[\mathrm{m}]$,
- The hyperbolic functions $\cosh$ and $\sinh$ describe the decaying influence of wave motion with depth, reflecting how the wave effects diminish with increasing distance from the water surface.

Finally, the particle acceleration in a wave field is calculated for both the horizontal and vertical components similarly. For a given frequency component, the acceleration is the second derivative of the wave-induced displacement concerning time. The horizontal and vertical components of particle acceleration are thus given by:

$$a_x(t, x, z) = \sum_n a_n(f_n)\omega_n^2 \frac{\cosh(k_n(z + d))}{\sinh(k_n d)} \sin(2\pi f_n t - k_n x + \phi_n) \tag{5.10}$$

$$a_z(t, x, z) = -\sum_n a_n(f_n)\omega_n^2 \frac{\sinh(k_n(z + d))}{\sinh(k_n d)} \cos(2\pi f_n t - k_n x + \phi_n) \tag{5.11}$$

Where:

- $a_n(f_n)$ is the amplitude for the n-th frequency component $[\mathrm{m}]$,
- $\omega_n = 2\pi f_n$ is the angular frequency of the n-th component $[\mathrm{rad/s}]$,
- k_n is the wave number corresponding to f_n $[-]$,
- d is the water depth $[\mathrm{m}]$,
- z is the depth below the water surface $[\mathrm{m}]$.

These equations are programmed based on Python scripts provided in other courses in the Hydraulic and Offshore Structures curriculum at the TU Delft. However, these scripts are altered to make them suitable for this application. Using the velocities and accelerations of the particles, the forcing on the structure can be determined using the Morison Equation.

5.3.2. Morison equation

The total force on the barrier, $F(t)$, consists of several components that account for both wave and current effects, as well as the added mass due to surrounding water and sargassum. This force is represented as follows:

$$F(t) = F_D(t) + F_{AM}(t) + F_S(t) \tag{5.12}$$

Where:

- $F_D(t)$ is the *Drag force* due to viscous effects and the relative velocity between the wave-induced water particle motion and the current,
- $F_{AM}(t)$ is the *Inertia force* (added mass), which accounts for the acceleration of the surrounding fluid,
- $F_S(t)$ is the *sargassum force*, representing the additional force caused by sargassum on the structure.

Important to note is that only forces from the y-direction are considered. This is due to the fact that in Chapter 6 the barrier is modelled as a thin plate. Because this plate is thin, the vertical forces, which come from the vertical motion of the water particles, are assumed to be neglected.

Drag Force

$F_D(t)$ is given by the relative velocity between the wave-induced particle velocity and the current speed. The force is proportional to the square of the relative velocity:

$$F_D(t) = \frac{1}{2} C_D \times \rho D(u(t) + U_x)|u(t) + U_x| \tag{5.13}$$

Where:

- $u(t)$ is the wave particle speed in $[\mathrm{m/s}]$,
- U is the current speed $[\mathrm{m/s}]$,
- C_d is the drag coefficient $[-]$,
- D is the diameter of the structure $[\mathrm{m}]$.

Inertia (Added Mass) Force

The $F_{AM}(t)$ represents the effect of the wave-induced acceleration of the water on the structure. It is proportional to the added mass of the fluid displaced by the structure:

$$F_{AM}(t) = C_I \rho A \dot{u}(t) \tag{5.14}$$

Where:

- $C_I = 1 + C_m$ is the inertia coefficient $[-]$,
- C_m is the mass coefficient $[-]$,
- $\dot{u}(t)$ is the wave-induced acceleration $[\mathrm{m/s^2}]$,
- A is the cross-sectional area of the submerged part of the structure $[\mathrm{m^2}]$.

Sargassum Force

$F_S(t)$ arises from the mass of sargassum, which exerts an additional force on the structure due to the motion of the surrounding water:

$$F_S(t) = \rho_s g d_s t_s \cdot \dot{u}(t) \tag{5.15}$$

Where:

- ρ_s represents the density of sargassum $[\mathrm{kg/m^3}]$,
- g is the gravitational constant $[\mathrm{m/s^2}]$,
- d_s is the depth to which sargassum extends $[\mathrm{m}]$,
- t_s is the thickness of the sargassum layer in y direction $[\mathrm{m}]$,
- $\dot{u}(t)$ is the wave-induced acceleration $[\mathrm{m/s^2}]$.

Combined Forces

By summing these components, the total force on the barrier can be expressed as:

$$F(t) = \frac{1}{2} C_D \cdot \rho D(u(t) + U)|u(t) + U| + C_I \rho A \dot{u}(t) + m_s \cdot \dot{u}(t) \tag{5.16}$$

Using the particle velocities and accelerations for each time instant, a time-dependent force can be calculated according to Equation 5.16. Based on the design choice for the first iteration, parameters such as C_m, C_i, C_d and an appropriate value for D can be chosen. These design parameters for the Puerto Morelos area are discussed in Chapter 6.

5.4. Finite Element Method

This section outlines the use of the FEM to solve the governing equations described in Section 5.1.2. It begins by defining the problem to be addressed, followed by a setup of the mesh for a generic barrier structure. Next, the required mass matrix is introduced, and the FEM solution process is explained. Finally, the necessary post-processing is addressed.

The FEM implementation is carried out in a Python environment, where input of the model variables can be easily modified, allowing users to tailor it to their specific needs. It is important to note that this model is adapted from a notebook used in the Computational Modelling course at TU Delft, but it has been customized to suit this particular problem.

5.4.1. Problem set up

To solve the barrier structure, a linear system of equations is constructed based on the governing equations of motion presented in Section 5.1.2. The general form of the equations for a linear dynamic system is given by:

$$\mathbf{M}\ddot{\mathbf{u}} + \mathbf{C}\dot{\mathbf{u}} + \mathbf{K}\mathbf{u} = \mathbf{f} \tag{5.17}$$

Where:

- $\mathbf{M}$ is the mass matrix,
- $\mathbf{C}$ is the damping matrix,
- $\mathbf{K}$ is the stiffness matrix,
- $\mathbf{f}$ is the force vector,
- $\mathbf{u}$ is the displacement vector,
- $\dot{\mathbf{u}}$ is the first derivative of displacement with respect to time (velocity),
- $\ddot{\mathbf{u}}$ is the second derivative of displacement with respect to time (acceleration).

In the case of a dynamic, nonlinear string structure, the tension depends on the deformation of the string, making it a dynamic geometric nonlinear problem. To solve this, a slightly different approach is used compared to standard methods.

Instead of relying on a stiffness matrix, the internal forces are calculated directly from the current configuration of the structure. Using this method, the system of equations is expressed as follows:

$$\mathbf{M}\ddot{\mathbf{u}} = \mathbf{f}_{\text{ext}} - \mathbf{f}_{\text{int}} \tag{5.18}$$

In this approach, both the stiffness matrix and the damping matrix are omitted because the stiffness matrix varies with deformation, depending on the solution itself. Using an explicit time integration scheme allows for a more efficient calculation of the internal forces directly.

The damping matrix is also excluded initially. Typically, the damping matrix is introduced after the semi-discrete form of the equation is reached, often using Rayleigh damping based on the stiffness and mass matrices. However, in this case, since the stiffness matrix is nonlinear, the damping is incorporated directly into the internal force calculation.

The resulting equation that is solved is as follows:

$$\mathbf{M}\ddot{\mathbf{u}}_{n+1} = \mathbf{f}_{\text{ext}} - \mathbf{f}_{\text{int}}(\mathbf{u}_n, \dot{\mathbf{u}}_n) \tag{5.19}$$

With this equation only the mass matrix is required, presented in Section 5.4.3.

5.4.2. Mesh set up

The barrier is positioned horizontally along the x-axis and is divided into multiple elements with nodes, all of equal length. Mooring lines are attached to the barrier, with each mooring line represented by a single element. These mooring lines are placed vertically along the barrier, and their element length is determined using Equation 5.4.
The Python notebook allows you to modify both the total length of the barrier and the element size of the barrier structure. Additionally, the x-coordinates for the mooring lines can be specified. Furthermore, it is possible to adjust the mooring line length and water depth, which are then used to calculate the length of the mooring lines within the mesh. A simple mesh grid with three mooring lines attached to the barrier is illustrated in Figure 5.2.

5.4.3. Mass matrix

Here the elemental mass matrix is given based upon the governing equations of motion given in Section 5.1.2. For the full derivation of the elemental mass matrix, please see Appendix H.

Since each node has two degrees of freedom, the degrees of freedom vector for each element becomes:

$$\mathbf{U}_e = \begin{bmatrix} u_i \\ v_i \\ u_{i+1} \\ v_{i+1} \end{bmatrix}$$

Based upon the structure of the elemental displacement vector, the elemental mass matrix is then as follows:

$$M_e = \frac{\Delta x}{6} \begin{bmatrix} 2\rho A & 0 & \rho A & 0 \\ 0 & 2\rho A & 0 & \rho A \\ \rho A & 0 & 2\rho A & 0 \\ 0 & \rho A & 0 & 2\rho A \end{bmatrix}$$

Eventually, this derived mass matrix is ready to be assembled into the global system of equations for further analysis. The Python notebook has the capability to input the required mass for both the mooring line elements and the barrier elements. This mass is expressed in units of $[\mathrm{kg/m}]$, which corresponds to the density of the material multiplied by its cross-sectional area.

5.4.4. Numerical solving

With the defined mesh, the element mass matrix is assembled into a global mass matrix. To apply the constraints of the structure, the rows and columns corresponding to the fixed nodes of the mooring lines (the anchor points) are removed.

In addition to spatial discretization, time discretization is applied using an explicit Runge-Kutta method of order 5(4) (RK45). By default, the SciPy solver uses adaptive time-stepping to ensure accuracy. This is why, when solving the ordinary differential equation, the time step varies during integration since the integration method checks the local error at each time step and adjusts the step size accordingly. This is to maintain accuracy in the integration process while minimising computational cost. So, if the error is within bounds, the time step is sufficient and the integration process proceeds. If the error exceeds the tolerance, the time step is reduced. The initial conditions for the problem are set to zero, meaning both displacement and velocity are zero at the initial time.

Finally, using Equation 5.19, the accelerations at each time step are computed. From these accelerations, the velocities and displacements are then determined.

As described in Section 5.4.1 the internal force is calculated at each time step. This force is made up of two parts: the stiffness component, which depends on the displacement of the element, and the damping component, which is based on its velocity. The stiffness component is determined by calculating the strain in each element and multiplying it by the axial stiffness of that element. Meanwhile, the damping component is calculated by finding the velocity difference between the nodes of the element and multiplying it by a damping constant. The total internal force is obtained by combining these two components. The Python notebook gives the possibility to adjust the axial stiffness of the barrier structure and the axial stiffness of the mooring lines. In addition, the damping constant can be adjusted.

5.4.5. Post-Processing

The goal of this FEM analysis is to determine the internal forces within the structure. Since the internal tension is calculated at each time step, these values can be stored throughout the simulation. Ultimately, a graph is generated, showing the point in time when and in which element the maximum tension occurs in the structure.

5.5. Vertical stability

This section describes how the buoyancy of the barrier is calculated. The calculation focuses on the anchor buoy system, as outlined in Section 4.5. The primary objective is to assess the vertical stability of both the barrier and the anchor buoys, ensuring that the barrier remains above the free water surface.

To assess the vertical stability, the system is divided into two components: one evaluating the buoyancy of the barrier itself and the other focusing on the buoyancy of the anchor buoy. The primary vertical force acting on the barrier comes from the weight of the barrier structure, meaning the barrier buoys must provide sufficient buoyancy to counteract this force. For the anchor buoy, the main vertical force comes from the mooring lines, so it must have enough buoyancy to resist the vertical component of the maximum force exerted by the mooring lines. These forces are illustrated in Figure 5.4

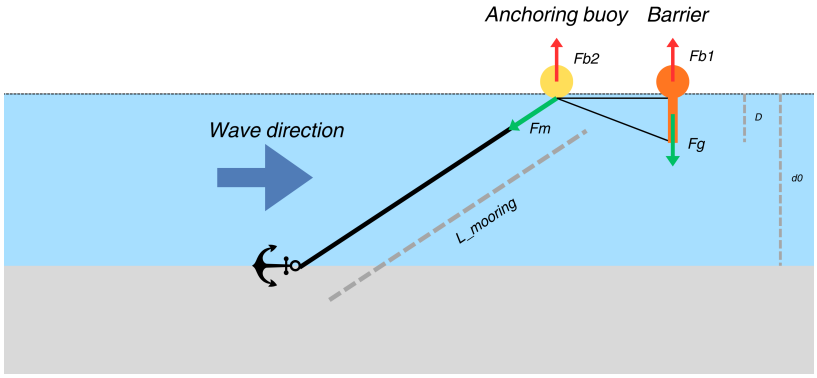

Figure 5.4: Overview of forces that play a role in vertical stability.

5.5.1. Buoyancy barrier

With the assumption that the buoys are spheres, the buoyancy capacity of the barrier buoys is calculated according to:

$$R = (((\rho_w - \rho_b) \cdot V_b \cdot g) + ((\rho_w - \rho_p) \cdot V_p \cdot g)) \cdot n \tag{5.20}$$

With V_b, V_p and n calculated in Equation 5.21, Equation 5.22 and Equation 5.23 respectively:

$$V_b = \frac{1}{6}\pi D_{bo}^3 - \frac{1}{6}\pi D_{bi}^3 \tag{5.21}$$

$$V_p = \frac{1}{6}\pi D_{bi}^3 \tag{5.22}$$

$$n = \frac{l}{s} \tag{5.23}$$

Where:

- ρ_w is the density of seawater $[\mathrm{kg/m^3}]$,
- ρ_b is the density of the buoy material $[\mathrm{kg/m^3}]$,
- ρ_p is the density of the polymer material inside the buoy $[\mathrm{kg/m^3}]$,
- V_b is the volume of the buoy material $[\mathrm{m^3}]$,
- V_p is the volume of the polymer material inside the buoy $[\mathrm{m^3}]$,
- n is the amount of buoys between two mooring lines,
- D_{bo} is the outside diameter of a buoy $[\mathrm{m}]$,
- D_{bi} is the inside diameter of the buoy $[\mathrm{m}]$,
- l is the distance between the mooring lines $[\mathrm{m}]$,
- s is the distance between the buoys in $[\mathrm{m}]$,
- g is the gravitational constant $[\mathrm{m/s^2}]$.

This buoyancy capacity should always be larger than the self weight of the barrier. This self weight is calculated according to:

$$F_{G,tot} = F_{G,net} + F_{G,t} \tag{5.24}$$

With:

$$F_{net} = (\rho_{net} - \rho_w) \cdot (D + D_{upper}) \cdot l \cdot g \tag{5.25}$$

$$F_t = \frac{1}{4}\pi D_t^2 \cdot l \cdot (\rho_t - \rho_w) \cdot g \cdot 2 \tag{5.26}$$

Where:

- $F_{G,net}$ is the self weight of the net structure $[\mathrm{N}]$,
- $F_{G,t}$ is the self weight of the tension cables $[\mathrm{N}]$,
- ρ_{net} is the density of the net structure $[\mathrm{kg/m^3}]$,
- ρ_t is the density of the tension cables $[\mathrm{kg/m^3}]$,
- D is the height of the submerged part of the barrier $[\mathrm{m}]$,
- D_{upper} is the height of the barrier above the free water surface $[\mathrm{m}]$,
- D_t is the diameter of the tension cables $[\mathrm{m}]$.

5.5.2. Buoyancy anchoring buoy

The buoyancy capacity of the anchor buoy is determined using Equation 5.20, applying the specific dimensions and material properties of the anchor buoy. The vertical force acting on the buoy comes from the tension in the mooring line together with the weight of the mooring line. The FEM model calculates the tension in the mooring line, and the maximum tension observed is used as input. Since the focus is on vertical stability, only the vertical component of this maximal mooring line tension is considered. This component is calculated as follows:

$$F_{vertical} = \frac{H_{max}}{X} \cdot F_h \tag{5.27}$$

With:

$$H_{max} = d_0 + \frac{1}{2}H_s \tag{5.28}$$

$$X = \sqrt{L_{mooring}^2 - H_{max}^2} \tag{5.29}$$

Where:

- H_{max} is the maximal water level $[\mathrm{m}]$,
- X is the horizontal distance between the anchoring point and the anchoring buoy $[\mathrm{m}]$,
- F_h is the maximal tension observed in the mooring lines $[\mathrm{N}]$,
- d_0 is the average still-water depth $[\mathrm{m}]$,
- H_s is the significant wave height $[\mathrm{m}]$,
- $L_{mooring}$ is the length of the mooring line $[\mathrm{m}]$.

The weight of the mooring line is calculated as follows:

$$F_{G,m} = \frac{1}{4}\pi D_m^2 \cdot L_{mooring} \cdot (\rho_m - \rho_w) \cdot g \tag{5.30}$$

Where:

- D_m is the diameter of the mooring line $[\mathrm{m}]$,
- $L_{mooring}$ is the length of the mooring line $[\mathrm{m}]$,
- ρ_m is the density of the mooring line $[\mathrm{kg/m^3}]$.

If the buoyancy capacity is larger than $F_{vertical} + F_{G,m}$, the design is sufficient buoyant and the vertical stability check is complete.

6 Implementation of the structural model

This chapter discusses the implementation of the structural model for a floating barrier in the Puerto Morelos area. It begins with an explanation of the parameters used in the structural model and the methods applied to obtain them. Section 6.1 introduces the parameters, followed by Section 6.2, which presents the force time series derived from H_s and T_p, as given in Section 3.4. Finally, the corresponding results are provided in Section 6.3. The wave energy spectrum and statistical amplitude spectrum (generated using MHKiT) are included in Appendix F.

6.1. Input parameters

Table 6.1 provides an overview of the input parameters for the structural model. Due to the extensive runtime of the model, the assumption is made that the current is the primary factor influencing force determination. This assumption has been preliminarily validated through test runs within a simplified model environment. However, further examination is necessary to confirm its validity for a larger-scale design. The final column in Table 3.4 presents the input parameters used in the hydrodynamic component. Complex to determine parameters are discussed in the following subsections. It is important to note that certain design parameters are initial choices and may be refined iteratively based on the model results.

Table 6.1: Input variables for the model.

Parameter	Value	Explanation
D_{cable} - Diameter of cable in barrier	5 cm	First design choice
$D_{mooring}$ - Diameter of mooring line	11 cm	First design choice
E - Stiffness steel	200 GPa	Please see Section 6.1.1
L - Length barrier	680 m	Reduced length due to computational capacity
l - Distance between mooring lines	20 m	To reduce running time
s - Distance between buoys	0.5 m	First design choice
D_{b1o} - Outside diameter of buoys of barrier	0.35 m	First design choice
D_{b1i} - Inside diameter of buoys of barrier	0.33 m	First design choice
D_{b2o} - Outside diameter of anchoring buoys	2.0 m	First design choice
D_{b2i} - Inside diameter of anchoring buoys	1.95 m	First design choice
D_m - Diameter of mooring lines	15 cm	First design choice
l_m - Maximal length of the mooring lines	6 m	First design choice: larger than d_0
ρ_b - Density of buoys	955 $\mathrm{kg/m^3}$	First design choice
ρ_p - Density of polymer inside buoy	50 $\mathrm{kg/m^3}$	As described in Section 4.2.2
ρ_{net} - Density of net	0.375 $\mathrm{kg/m^3}$	First design choice
ρ - Density of water	1022 $\mathrm{kg/m^3}$	Measured density of Puerto Morelos [17]
C_D - Drag coefficient	0.6	As described in Section 6.1.2
C_m - Mass coefficient	1	Conservative value based on empirical relations
C_I - Inertia coefficient	2	$C_I = C_m + 1$
C - Damping coefficient	$0.01 \cdot EA$	Prevents system from becoming unstable
D - Height of submerged part of the barrier	1 m	Please see Section 6.1.3
D_{upper} - Height of part of the barrier above water	0.4 m	First design choice
T_p - Peak period	5.03 s	As described in Section 3.4
α - Angle of incidence wave	39.6°	As described in Section 3.4
H_s - Significant wave height	0.57 m	As described in Section 3.4
d_0 - Average still water depth	3.5 m	As described in Chapter 3
U - Current speed	1.06 $\mathrm{m/s}$	As described in Section 3.4
m_s - Mass of sargassum	13.36 $\mathrm{kg/m^3}$	As described in Section 2.3.1
d_s - Depth of sargassum	0.25 m	As described in Section 2.3.1
t_s - Thickness of accumulated sargassum	1 m	As described in Section 6.1.4
T - Length evaluation time of forcing	60 s	To reduce running time
dt - Time step in solver	0.5 s	To reduce running time

6.1.1. Mooring line material

In Section 4.2, it was noted that the mooring line material was initially chosen as nylon rope. However, due to the low modus of elasticity of nylon and its associated nonlinear behaviour, steel was selected as a replacement within

the model. This substitution increases the axial stiffness of the mooring line, thereby reducing deformations.

6.1.2. Drag coefficient

To account for the drag force exerted by the water on the structure, it is necessary to determine an appropriate drag coefficient, C_D. Since the structure consists of multiple shapes rather than a single uniform one, determining this coefficient presents a challenge. To address this, certain simplifications are made. Figure 6.1 illustrates the cross-section of the design. The mooring lines are sufficiently long to allow the barrier to move freely up and down, so the spherical shape of the buoy is assumed to contribute minimally to the overall drag. The buoy's buoyant nature allows it to "ride" the wave movement. Thus, the simplification has been made that the buoy does not contribute to the drag: solely the protective net below the free surface.

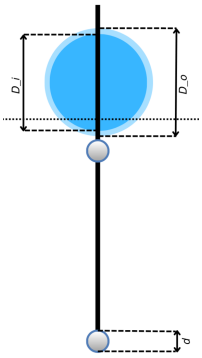

Figure 6.1: Schematic of the cross-section of the barrier.

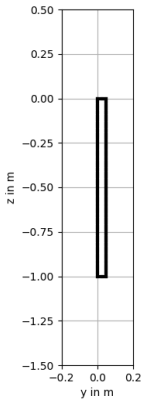

Figure 6.2: Simplified cross-section that is used in the model.

Research has been done on the effects of biofouling on fishing nets. Therefore, the net and cables of the barrier are simplified to represent a net, heavily fouled with biofouling. The biofouling in this model represents the presence of sargassum. Based on findings from [11], a drag coefficient of 0.6 is used. Additionally, the dimensions of the cross-sections are shown in Figure 6.2. Given the thin structure of the barrier, it is reasonable to assume that only forces acting in the y-direction need to be considered.

Since determining the drag coefficient is challenging, the model is executed with multiple values for C_D. This is presented in Chapter 7.

6.1.3. Height of the submerged part of the barrier

As it is assumed that the mooring lines are sufficiently long to allow the barrier to move freely up and down, primarily the netting will be considered as the height of the submerged part of the barrier. In this assumption, it is also taken into consideration that the waves will not break at the barrier, as described in Section 3.4. Thus, the height of the submerged part of the barrier is approximately 1 m.

6.1.4. Thickness sargassum

The thickness of the sargassum layer on the water surface is needed to determine the volume of the sargassum pushing on the structure. In the extreme value conditions, the thickness of sargassum in front of the barrier is limited, as most particles are flushed away. However, to take a conservative approximation, a thickness of 1 m is chosen. This is based on information in Section 3.4. Note that this is in the y-direction on the water surface.

6.2. Force determination

The wave elevation, velocity, and acceleration time series are determined as described in Chapter 5. These time series can be found in Appendix G. Based on the wave-particle velocity and accelerations, the forcing on the barrier is determined by making use of the Morison Equation. This gives the plot as illustrated in Figure 6.3. Again, only the force in the horizontal direction (y-direction) is considered.

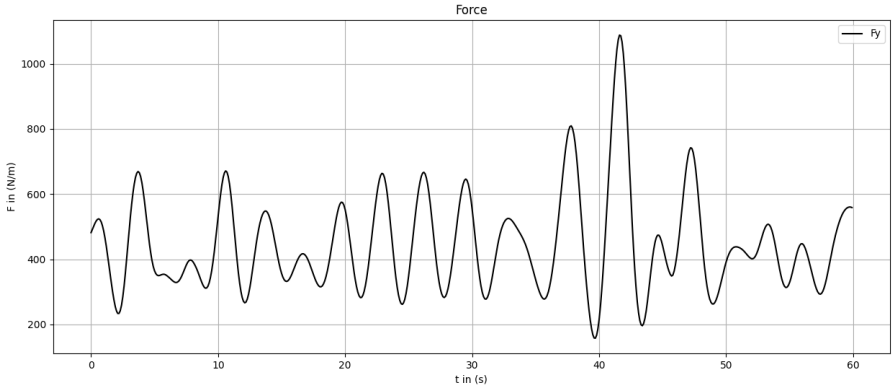

Figure 6.3: Force in y-direction F_y, based on wave characteristics described in Appendix G.

6.3. Results

To provide the results of the model, a stress check of the barrier structure and mooring lines is conducted. In addition, the vertical stability of the structure is investigated.

6.3.1. Stress check barrier

To calculate the maximum stresses in the barrier the maximum internal forces at each time step are first analysed. The maximum internal force within the barrier is shown in Figure 6.4, where a peak force of 147.4 kN is observed.

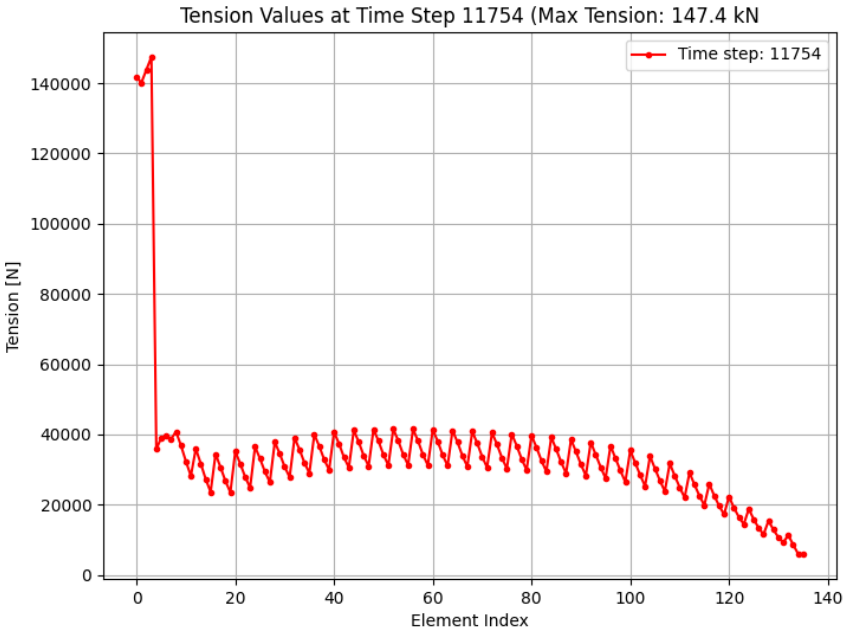

Figure 6.4: Maximum tension in barrier, input parameters as described in Table 6.1.

The tension on the left side shows an abnormally high value. This occurs because the barrier is suddenly removed from its initial position. To focus on the relevant data where the internal forces are representative, the first 25% of the data points will be excluded from the analysis, ensuring that only the results after the barrier has settled into position are considered, once the initial displacement effects have diminished. These results are shown in Figure 6.5.

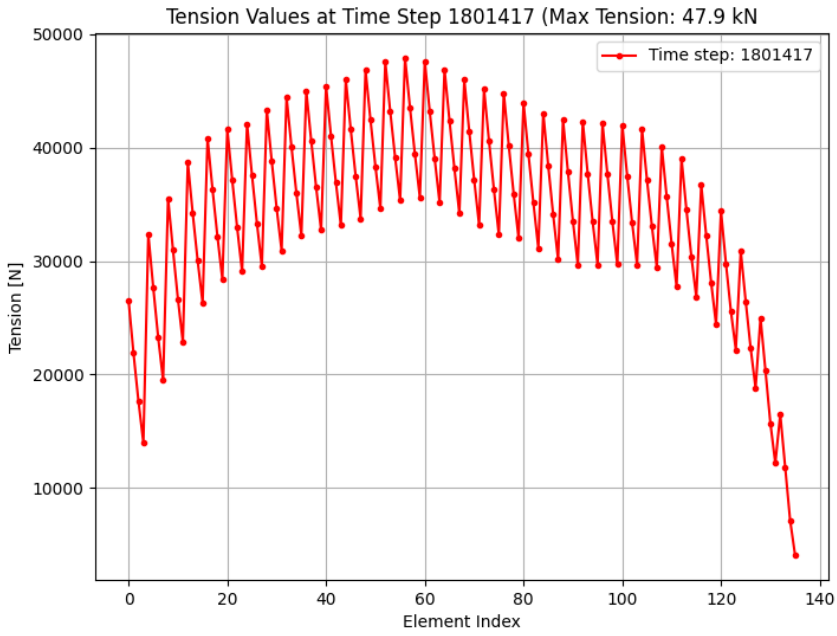

Figure 6.5: Maximum tension in the barrier for the last 75% of the time steps, input parameters as described in Table 6.1.

Based on the newly found maximum tension of 47.9 kN in Figure 6.5, the maximum stress in the barrier is computed. The stress σ can be calculated according to:

$$\sigma = \frac{F_{tension}}{A_{cable}} \tag{6.1}$$

Where:

- σ is the stress $[\mathrm{N/mm^2}]$
- $F_{tension}$ is the maximal tension force in the barrier $[\mathrm{N}]$
- A_{cable} is the total area of the cables in the barrier $[\mathrm{mm^2}]$

As the cables are made from steel, it needs to be checked whether the following is true:

$$\sigma \leq f_{y,d} \tag{6.2}$$

Where:

- f_y is the yield strength of steel $[\mathrm{MPa}]$

As $A_{cable} = 3927\ \mathrm{mm^2}$, and $F_{tension} = 47.9\ \mathrm{kN}$, this results in $\sigma = 12.0\ \mathrm{N/mm^2}$. If it is assumed that S235 steel is used ($f_y = 235\ \mathrm{N/mm^2}$), the unity check results in 0.05.

6.3.2. Stress check mooring lines

The maximum tensile force in the mooring lines is obtained from Figure 6.6, where the maximum internal forces are plotted for each mooring line.

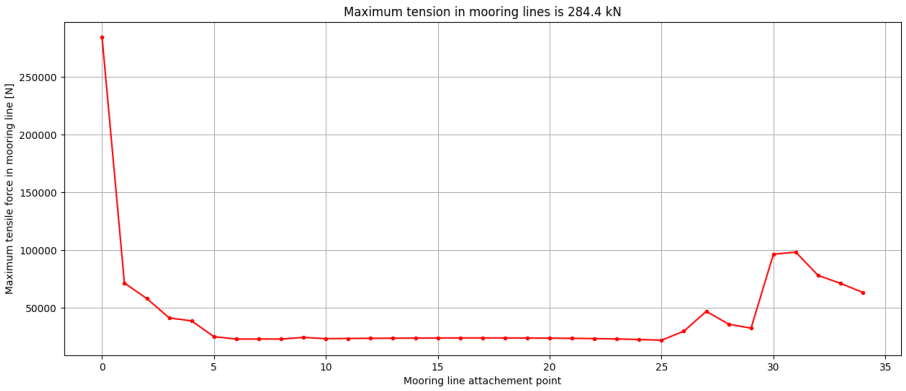

Figure 6.6: Maximum tension in each mooring line, input parameters as described in Table 6.1.

Once again, an unusually high peak of 284.4 kN is observed on the left side, which may suggest that the results are significantly affected by the initial movement of the barrier from its starting position. This initial impulse force is likely unrealistic. Therefore, for this analysis, the first 25% of the time steps and their corresponding results are excluded. The results are plotted in Figure 6.7

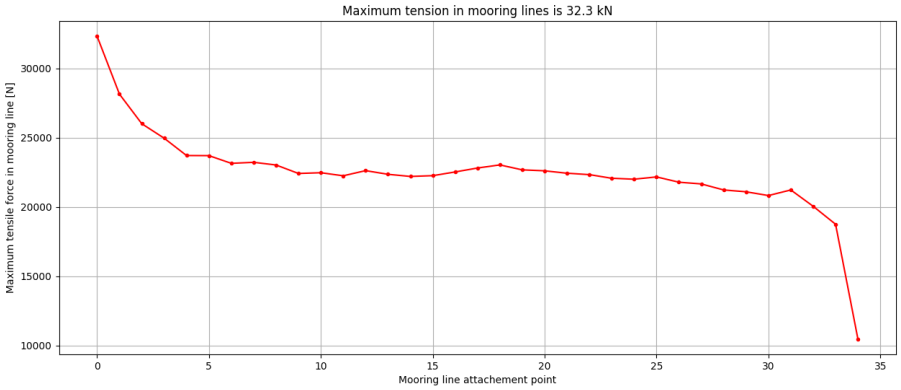

Figure 6.7: Maximum tension in each mooring line, input parameters as described in Table 6.1.

Following the same procedure for the mooring lines as for the barrier, the following can be found: As $A_{mooring} = 17671\ \mathrm{mm}^2$, and $F_{tension} = 32.3\ \mathrm{kN}$, this results in $\sigma = 1.9\ \mathrm{N/mm}^2$. If it is assumed that S235 steel will be used ($f_y = 235\ \mathrm{N/mm}^2$), the unity check results in 0.008.

6.3.3. Vertical stability check

First, the buoyancy of the barrier buoys is evaluated using a buoy spacing of 0.5 m. The outer diameter is set at 0.35 m, while the inner diameter is assumed to be 0.33 m. Based on the material densities and the barrier dimensions, a unity check value of 0.72 is obtained.

Next, the anchoring buoys are analysed. From the barrier model, the maximum mooring line tension is calculated to be 32.3 kN. Assuming an outer diameter of 2.0 m and an inner diameter of 1.95 m for the anchoring buoys, a unity check value of 0.99 is determined.

6.4. Summary of results

Table 6.2: Summary of results.

Parameter	Value
Maximum tensile force in barrier $[\mathrm{kN}]$	147.4
Maximum tensile force in mooring lines $[\mathrm{kN}]$	32.3
Unity check stress in barrier $[-]$	0.05
Unity check stress in mooring line $[-]$	0.008
Unity check vertical stability anchoring buoys $[-]$	0.99
Unity check vertical stability barrier buoys $[-]$	0.72

7 Validation of the structural model

This chapter delves into the unexpected results observed in Chapter 6. In response to these findings, specific parameters likely to impact these results have been selected and adjusted to assess their effects and sensitivity. In this chapter first the unusual results are examined in Section 7.1. Next, the parameters that are modified are introduced in Section 7.2. Finally, the outcomes resulting from these parameter changes are presented in Section 7.3.

7.1. Unexpected result

In Chapter 6, the vertical stability unity check of 0.99 is achieved only when the diameter of the anchoring buoys is 2 m. However, this diameter is excessively large, especially considering that the still water depth is only 3.5 m. The large buoy diameter is necessary to counteract the significant tension in the mooring lines, which generates a substantial vertical force that pulls the buoy downward.

To better understand the model, it is useful to explore potential adjustments to its parameters and assess how these changes influence the results. By fine-tuning certain parameters, a more reasonable result for the vertical stability check could be achieved. Additionally, this process allows for partial validation of the model, as it enables to verify whether the results from parameter adjustments align with expected outcomes.

7.2. Variable parameters

This section outlines the three parameters that are modified to evaluate their impact on the results.

7.2.1. Mooring Line Spacing

To further examine the influence of the number of mooring lines on the tension in each line, the model is run with different spacings between the mooring lines. Ideally, the spacing is reduced, which increases the number of mooring lines. However, adding more mooring lines significantly increases the running time of the model, which is not feasible due to computational limitations. Therefore, the opposite approach is taken: the model is run with increased spacing between the mooring lines, effectively reducing their total number. The spacing is increased from 20 m to 40 m. It is expected that, with fewer mooring lines, the maximum force on each line increases. If this is observed, it is inferred that the reverse occurs with more mooring lines.

7.2.2. Axial Stiffness of Mooring Lines

Another parameter that relates to the vertical stability check of the anchoring buoys, is the excessively high axial stiffness in the mooring lines. To address this, the model is rerun using a smaller mooring line diameter, or a different material, which lowers the value of EA. Having a lower EA, should result in lower tensions, but more strain in the material. If the tensions are reduced, it is shown that changing the material and diameter of the mooring line indeed has an influence on the tension within that mooring line. Therefore, the model is run with an EA value of 100 times smaller.

7.2.3. Drag Coefficient

The drag coefficient C_D plays a crucial role in determining the forces acting on the barrier. Given the difficulty in accurately defining C_D, the model is additionally tested with two different values: $C_D = 0.4$ and $C_D = 0.8$. It is expected that a lower drag coefficient results in lower forces, while a higher drag coefficient leads to higher forces. The primary aim of this analysis is to evaluate the extent to which the drag coefficient affects the system's overall behaviour.

7.3. Final results

7.3.1. Mooring line spacing

This subsection presents the maximum tension in the barrier and the maximum tensions in each mooring line when the model is executed with increased spacing between the mooring lines, thereby reducing their total number. The spacing between the mooring lines is increased from 20 m to 40 m.

Maximum tension in the barrier

Figure 7.1 illustrates the maximum tension in the barrier with a reduced number of mooring lines. In comparison to Figure 6.5, the maximum tension that occurred has increased from 47.9 kN to 81.4 kN: almost doubling. This

behaviour is expected, as it is intuitive that reducing the number of mooring lines increases the tension within the structure, as the structure must bear a greater load.

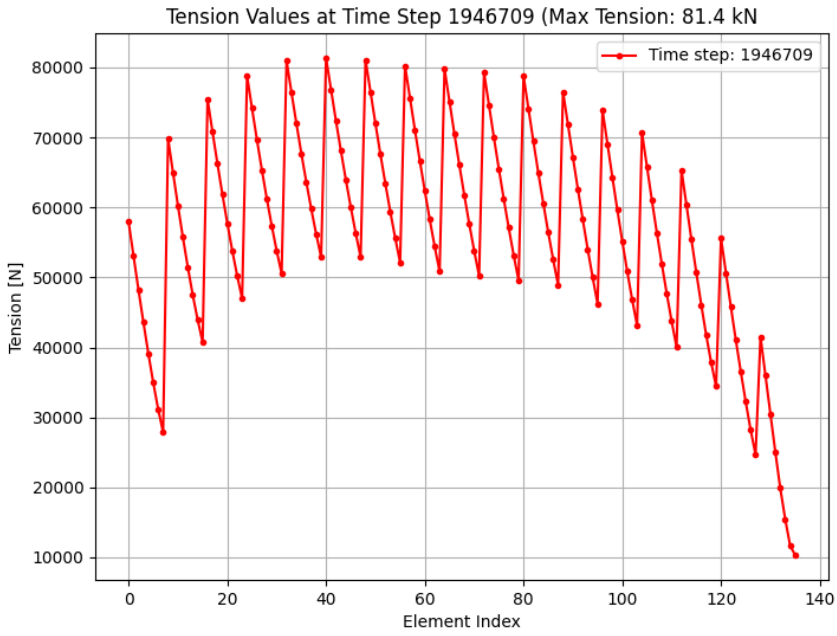

Figure 7.1: Maximum tension in barrier for 40 m mooring line spacing. Other input parameters: see Table 6.1.

Maximum tension in each mooring line

Figure 7.2 shows the maximum tension in each mooring line when the number of mooring lines is reduced. The figure indicates a doubling of maximum tension, rising from 32.4 kN in Figure 6.7 to around 65.4 kN. These results align perfectly with expectations, as reducing the number of mooring lines increases the load on each line.

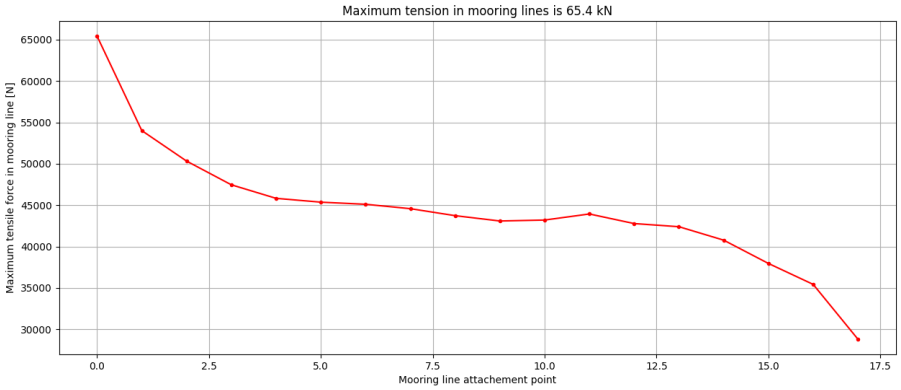

Figure 7.2: Maximum tension in each mooring line for 40 m mooring line spacing, Other input parameters: see Table 6.1.

7.3.2. Axial stiffness mooring lines

This subsection presents the maximum tension in the barrier and the tension in each mooring line when the model is run with an EA value for the mooring lines reduced by a factor of 100, thereby significantly reducing their stiffness.

Maximum tension in the barrier

Figure 7.3 shows the tension in the barrier for a reduced EA. The behaviour is almost identical to the behaviour that was observed in Figure 6.5, as it is 0.4 kN lower. However, the displacements in this model run are higher, since the barrier is effectively less constrained by the mooring lines. This can be seen according to the following relationship:

$$T = EA \cdot \epsilon \tag{7.1}$$

Where:

- T is the tension force in an element $[\mathrm{N}]$,

- ϵ is the strain in an element $[-]$.

Since the tension remains the same and EA decreases, ϵ can only increase, thus resulting in larger deformations.

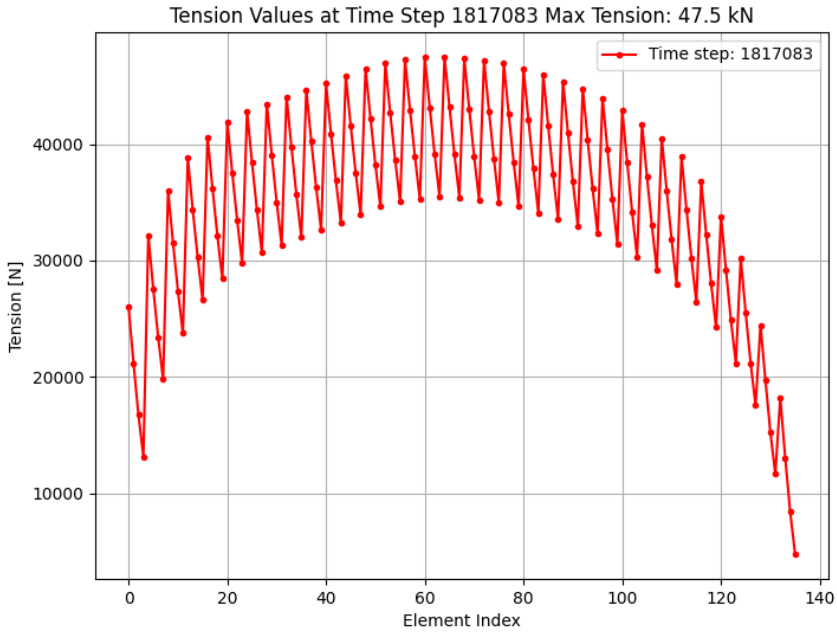

Figure 7.3: Maximum tension in barrier for EA 100 times smaller. Other input parameters: see Table 6.1.

Maximum tension in each mooring line

Figure 7.4 shows the maximum tension in each mooring line for a lower EA value per mooring line. Compared to Figure 6.7, the maximum tension that occurs is almost the same. 31.7 kN compared to 32.3 kN. As the displacements are larger, this is in line with the expectations.

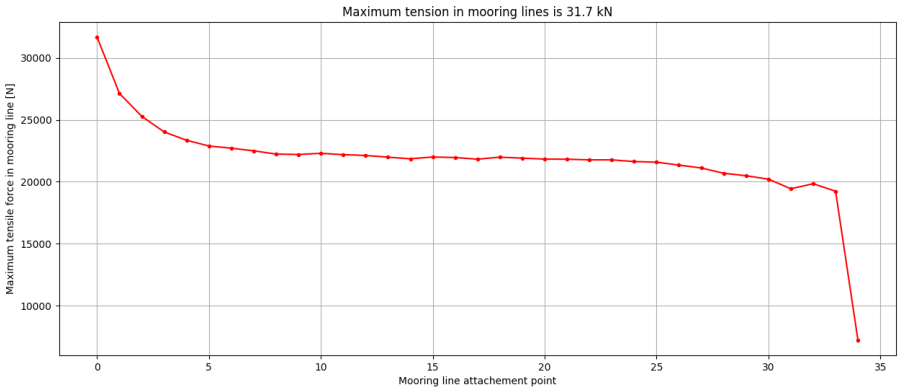

Figure 7.4: Maximum tension distribution in mooring lines for EA 100 times smaller. Other input parameters: see Table 6.1.

7.3.3. Drag coefficient: C_D = 0.4

This subsection presents the maximum tension in the barrier and the maximum tension in each mooring line when the model is run with $C_D = 0.4$, thereby reducing the forcing on the barrier.

Maximum tension in the barrier

Figure 7.5 shows the maximum tension in the barrier for $C_D = 0.4$. Compared to Figure 6.5, it is observed that the tension decreases from 47.9 kN to 38.3 kN. This is in line with expectations, as a lower drag coefficient intuitively results in lower forces within the barrier.

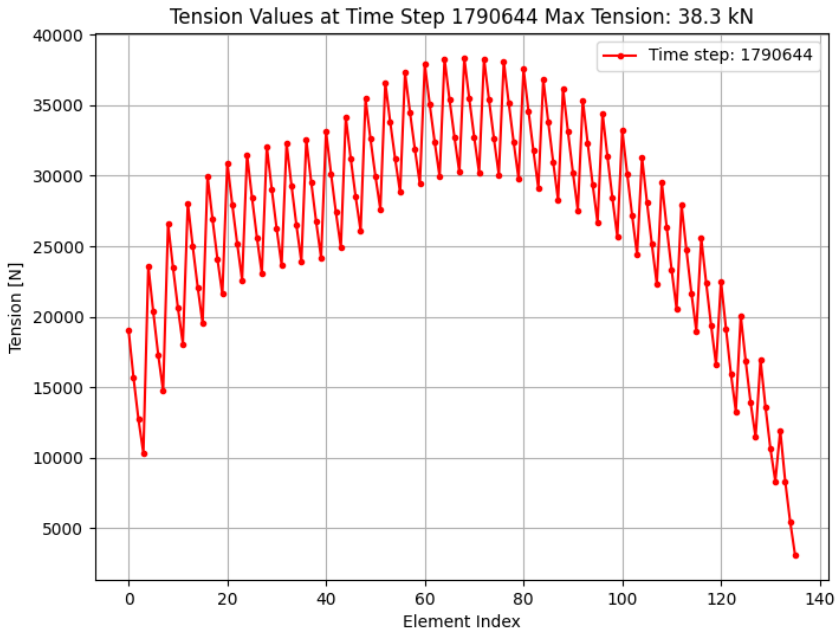

Figure 7.5: Maximum tension in barrier for $C_D = 0.4$. Other input parameters: see Table 6.1.

Maximum tension in each mooring line

Figure 7.6 shows the maximum tension in the mooring lines for $C_D = 0.4$. Compared to Figure 6.7, the tension has decreased from 32.3 kN to 22.8 kN. This is in line with the expectations, as a lower drag coefficient results in less forcing on the barrier. Therefore, the mooring lines need to withstand less force.

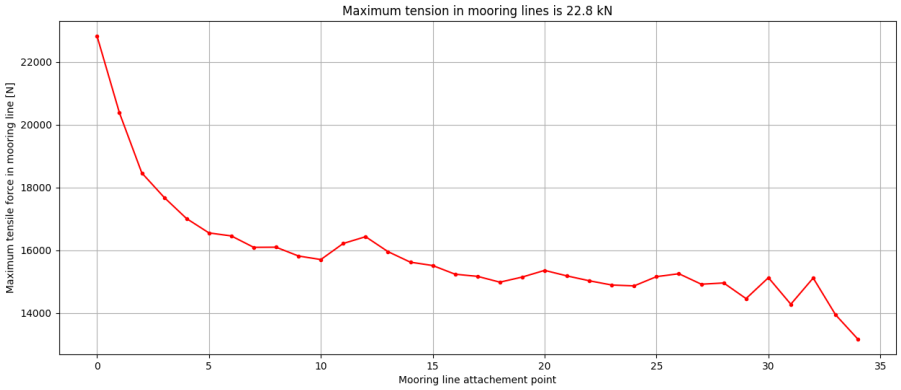

Figure 7.6: Maximum tension in mooring lines for $C_D = 0.4$. Other input parameters: see Table 6.1.

7.3.4. Drag coefficient: $C_D = 0.8$

This subsection presents the maximum tension in the barrier and the maximum tension in each mooring line when the model is run with $C_D = 0.8$, thereby increasing the forcing on the barrier.

Maximum tension in the barrier

Figure 7.7 illustrates the maximum tension in the barrier for $C_D = 0.8$. Compared to Figure 6.5, the maximum tension has increased from 47.9 kN to 57.7 kN. Again, this is in line with the expectations, as a higher C_D results in a larger forcing on the barrier. Consequently, a larger tension in the barrier is observed.

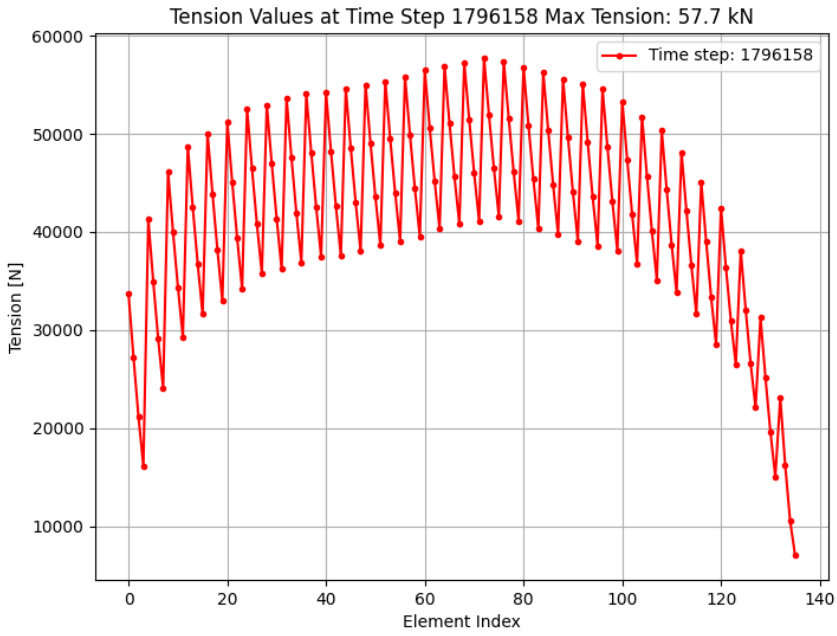

Figure 7.7: Maximum tension in barrier for $C_D = 0.8$. Other input parameters: see Table 6.1.

Maximum tension in each mooring line

Figure 7.8 presents the maximum tension in the mooring lines for $C_D = 0.8$. Compared to Figure 6.7, the maximum tension has increased from 32.3 kN to 41.6 kN. Again, this result is in line with the expectations, as a higher drag coefficient results in a larger forcing on the barrier. Consequently, this results in larger forces within the mooring lines.

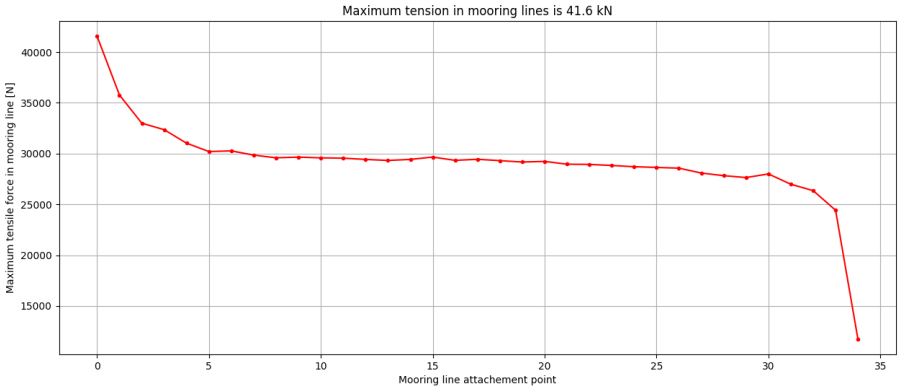

Figure 7.8: Maximum tension in mooring lines for $C_D = 0.8$. Other input parameters: see Table 6.1.

8 Discussion

This chapter covers all the key discussion points related to this study. It begins by discussing the validity of the study in Section 8.1. Then, Section 8.2 examines the limitations of the study from hydrodynamic, barrier design, and structural perspectives.

8.1. Validity of the study

8.1.1. Hydrodynamic analysis

The results of the hydrodynamic analysis are based on the model outcomes from the Delft3D software. The choice of parameters and inputs significantly influences the results of the model. Several aspects and assumptions made during the project raise concerns about the validity of the outcomes and whether the modelled results are accurate enough to answer the research questions stated in Section 1.3. The following aspects raise concerns and require further discussion.

Location

The phenomenon that has the most influence on the hydrodynamic model is the Yucatán Current. This current has a constant magnitude of 0.5 $\mathrm{m/s}$, based on research that measured this current near Cozumel. It is uncertain whether this value of 0.5 is of correct use at the southeastern boundary implemented in the model. Because this current has such a large influence on the flow patterns, a more detailed analysis of this current near the coast of Puerto Morelos is important.

Secondly, the ends of both barriers are positioned near the grid boundaries. At the southern boundary, a negative current reaching 0.1 $\mathrm{m/s}$ at the edge of the reef is introduced, though it remains uncertain whether this value is an accurate assumption. At the northern boundary, a Neumann condition is applied. Consequently, the hydrodynamic results near these boundaries are less reliable. Increasing the grid size would improve the accuracy of the flow in these areas. Additionally, the model boundaries used in this study have not been validated. For further studies, such validation is necessary to enhance the accuracy of the modelled flow. This also counts for hydrodynamic results at the gates or over the reefs. By utilising real-life monitoring sensors within the research area, the models in Delft3D can be validated against the obtained hydrodynamic data.

Furthermore, the results of the EVA indicate that waves have already dissipated from the northeastern boundary to the start of the big gate, as seen by the offshore separation line (blue to red) in Figure 3.10. This early dissipation raises doubts about the accuracy of the hydrodynamic results for the observation points of barrier 2 (north). If the offshore condition extends uniformly across the entire eastern boundary, and the waves break at the reef, the hydrodynamic results would be more consistent. However, with the results shown in Figure 3.10, the fact that waves have already broken before reaching the northern reef certainly influences the flow patterns within the reef lagoon. This undoubtedly impacts the findings, especially since the results for barrier 2 were used as input for the structural model. The reasons for the incorrect wave modelling and its impact on the structural input remain unclear.

Sargassum

Modelling sargassum presents a challenge, as its physical properties are represented by particles within a fluid, requiring validation. Now, based on argued assumptions, sargassum is modelled with results that seem valid, but proof from field data is necessary for the properties of the tracers. For example, a passive tracer is used, which has no impact on the flow within the model. This makes the model less complex, but the assumption that the presence of sargassum does not affect the flow is not grounded. If research results show that sargassum does interact with the flow, another model in the Water Quality module of Delft3D could be used.

Another important sargassum uncertainty is the buoyant nature of the algae and the influence of the direct forcing of wind on the part of the object extending above the surface. It is unclear when sargassum starts deteriorating and loses this buoyancy. This is important when further research is done on sargassum captured by the barrier. Next to this, the direct forcing of wind is now based on a scientific paper but also requires validation. One of the conclusions from the paper is that the wind drag coefficient is not constant and changes under different conditions.

Floating barrier

In addition to the modelled sargassum transport, the impact of a floating barrier on the flow circulation of the reef remains uncertain. As discussed in Section 2.4, when a floating structure is placed within the reef after wave dissipation, its influence on wave set-up can be assumed negligible. However, since the designed barrier includes a fine

mesh grid underneath the buoy, it remains unclear how the flow behaves as it passes through the barrier. According to fluid dynamics, when flow approaches a gate extending to a certain depth, it accelerates as it passes through and returns to equilibrium further downstream, with a certain amount of energy loss. The presence of a mesh grid will certainly affect the flow to some extent, possibly influencing the flow behind the barrier. It is uncertain whether this effect is significant enough to impact the flushing capacities of the lagoon. The obtained results of Section 3.3, assume the impact of such a mesh grid to be negligible.

Both uncertainties in flow dynamics and sargassum transport behaviour, contribute to the overall uncertainty regarding the optimal placement of a floating barrier. However, when viewed on a large scale, the results do indicate effective areas where sargassum particles, if transported similarly to the modelled behaviour, can be redirected away from the coast.

8.1.2. Barrier design

In designing an effective sargassum barrier for Puerto Morelos, this study faced challenges related to the trial-and-error nature of existing sargassum management solutions. Many commercial barriers, while marketed as highly effective, lack independent scientific validation and their claimed performance is unsupported.

Barrier

Several companies, such as Beach Bouncer, claim near-perfect sargassum capture rates, up to 100% effectiveness. However, these claims are rarely supported by scientific research, raising questions about their validity. In this project, the lack of reliable data influenced the decision not to use Type I barriers in Section 4.5.3. If such performance figures were validated, it could have provided a stronger case for choosing Type I barriers. More accurate performance studies of the different barrier types would significantly improve the quality of future barrier selection processes.

Similarly, as stated in Section 4.1 it is claimed that large-holed nets do not pose a risk of entangling sea turtles or sargassum, but again, there is no independent research confirming this. To mitigate these risks, mesh grids with 3 mm holes were chosen for the barrier, ensuring that sea turtles and sargassum are unlikely to become trapped. Choosing more proven mesh designs ensures that potential risks to marine life are minimized, even in the absence of strong empirical evidence from manufacturers.

Another important consideration is whether the height of the buoy above the waterline (freeboard) is sufficient to prevent overflow of sargassum during extreme conditions, such as high waves and strong currents (EVA conditions). If the barrier is too low, it reduces the barrier's effectiveness. Additional testing and validation are recommended to confirm that the current buoy height can handle these conditions, ensuring the barrier performs well in the conditions of Puerto Morelos.

8.1.3. Structural model

Based on the unexpected result regarding vertical stability, the validity of the model was assessed in Chapter 7. This assessment involved adjusting the mooring line spacing, axial stiffness of the mooring lines and the drag coefficient of the barrier, after which the outcomes were compared with its expectations. These adjustments helped partially validate the model, indicating that any discrepancies likely arise from input parameters rather than flaws within the model itself.

Given that the only truly unexpected outcome was the need for significantly larger-than-anticipated anchoring buoys, parameter adjustments were implemented. Each change yielded results consistent with theoretical expectations, supporting the hypothesis that the large buoy dimensions result from the chosen input parameters. This hypothesis is plausible, as the increased buoy size may be attributed to the following factors.

Firstly, the mooring line spacing was adjusted. Due to computational limitations, this spacing was increased, as decreasing the spacing results in excessively long running times. The results were in line with the expectations: the tension in each mooring line increased. It is inferred that the reverse happens when the mooring line spacing reduces. This means that with more mooring lines there would be less tension in the mooring lines, leading to a better vertical stability unity check.

Secondly, it is observed that the drag coefficient plays an important role in force determination. Since the barrier does not have a regular shape, no standard drag coefficient is available. A study was found to determine the drag coefficient of a fishing net with severe biofouling, and this value has been applied to the barrier. However, this drag coefficient has been used for the entire length of the net, whereas in practice, only about one-fourth of the net will likely be covered by sargassum. It is therefore uncertain whether the entire protective net has a drag coefficient of 0.6, or if certain parts experience lower drag. Multiple values of C_D were used in the model to address this uncertainty and the resulting force was significantly different. If the drag coefficient in reality is lower, this would also lead

to a more reasonable vertical stability unity check. Ideally, the C_D of a barrier is determined empirically, as in this study, the presence of the buoy is neglected as well.

Lastly, the forcing applied to the barrier is likely to be uncertain. Initially, the hydrodynamic model introduces considerable uncertainty in determining T_p and H_s. Based on this uncertainty, a peak value is selected for the barrier design. Force calculations then rely on this peak H_s and T_p and apply the JONSWAP method, which further adds uncertainty and occasionally produces outliers with higher force values in the time series. This results in a maximum force derived from an already high peak, potentially leading to an overestimation. Since the highest tension in the mooring lines occurs under this peak force—necessitating large anchoring buoys—it is possible that the applied forcing is overstated. With this in mind, it could be that with the real forcing the dimensions of the buoy are more realistic.

Besides the aforementioned points, the initial conditions have a severe impact on the results. In the model, the barrier starts suddenly moving as the force is applied. This results in a large impulse force on the barrier. This force is not representative of the internal forcing, as it is way higher than the barrier in reality experiences. Therefore, the first 25% of the resulting forcing is removed. However, this number has been picked to make sure that the initial position does not affect the results. A lower percentage, e.g. 10%, would perhaps suffice as well. Further investigation is required to address this initial condition issue thoroughly.

8.2. Limitations of the study

8.2.1. Hydrodynamic analysis

Hydrodynamic settings

This research only investigates the three largest sargassum arrivals, leaving uncertainty about how the barrier system functions under other hydrodynamic conditions. For instance, based on the 10-year time series analysis, wave heights offshore are lower than an H_s of 0.75 m during the large arrival condition 55% of the time. In this research, it is not investigated for which hydrodynamic condition the big gate loses its flushing capability, which is a key factor in determining the optimal location of the barrier. The results demonstrate that the barrier performs effectively under the three large arrival conditions. However, its performance under different conditions remains a limitation of this study.

Sargassum

Another important limitation is the number of layers applied in the vertical direction in the Delft3D software. Sargassum floats in the upper layer of the water column, where the current is strongly impacted by wind and waves. For an accurate representation of sargassum transport behaviour, multiple layers with a small top layer compared to the others give the most realistic flow results. Adding more layers, however, requires significantly more computing time and capacity. Multiple layers together with longer runs consumed too much computing capacity and resulted in high computer memory outputs which were not manageable in the working conditions provided.

EVA

The challenge with the EVA lies in the introduction of subjectivity at two key stages. First, the threshold is selected from a broad spectrum of possible values, derived from the Mean Residual Life (MRL) figure. This range, as well as the threshold itself, could have been determined differently. As described in Section 2.2.3, this choice significantly affects the number of data points considered in the EVA.

Secondly there is subjectivity in determining the peak period. Multiple methods are available to derive T_p. For this research, it is chosen to compare the zero crossing period, T_z, value to the corresponding H_s values from the Copernicus dataset. Based on the linear trend of these values, a T_z value is calculated for the extreme H_s. However, the scatter plot data includes wind-driven wave data, meaning the linear trend is visually determined. This step introduces uncertainty into the calculation of T_z, and thus T_p.

Floating barrier

The final limitation lies in the modelling of the floating barrier. Based on the results presented in Section 3.3, it can be concluded that further research is required to correctly model the interaction between particles in the upper layer with the presence of floating structures. This is especially important for understanding the detailed movement of sargassum along the barrier. In this study, for barriers of 2160 m and 1375 m in length, 9 and 6 observation points were added respectively. However, for every 200- meters in between the observation points, it remains unclear whether sargassum is being trapped or continues flowing toward the flushing areas.

8.2.2. Barrier design

Anchoring

The lack of site-specific data on seabed attachment strength at Puerto Morelos posed a significant challenge. Without this information, it remains difficult to accurately quantify the forces needed for the anchoring system, which limited

the ability to perform a detailed cost analysis. Without understanding how well the anchoring system would perform under local conditions, only qualitative assessments of anchoring costs were possible. One potential solution to overcome this issue is using data from oil booms, where similar marine forces are encountered. If this data could be applied, it would help estimate the forces on the anchoring system and support a more detailed and accurate cost assessment for this project.

Materials

The performance of HDPE and PMMA buoys, under the specific marine conditions at Puerto Morelos has not been studied. This gap made it difficult to do a quantitative analysis of the prolonged lifetime of PMMA buoys. Thus, to conduct a cost-benefit analysis when comparing PMMA to HDPE. Similarly, nanocoatings were considered to extend the lifespan of barrier materials by reducing biofouling and UV degradation. However, the lack of data on lifespan improvements and the most suitable types of nanocoatings for the barriers created difficulties in determining their effectiveness. Without this information, it is challenging to provide quantitative data on their impact on long-term maintenance and costs. Further studies on the performance of the polymers and nanocoatings are required to optimize material and protection to improve the overall durability of the barrier.

Design Puerto Morelos

Although the Type II design is justified based on current knowledge, alternative designs could be explored to enhance performance or reduce costs, especially when adapted to the conditions of Puerto Morelos. Further testing and adaptation may reveal other barrier types that can meet the same environmental challenges while offering different benefits, such as easier deployment or better resistance against storm conditions.

8.2.3. Structural model

Modelling

The primary limitation of the model is the excessively long running time. As discussed in Chapter 3 and Chapter 4, a barrier length of 1370 m with mooring lines spaced every 8 m was recommended. However, due to limited computational capacity, the simulations could not be completed within 12 hours (the longest the model was run). To address this, the barrier length was reduced to 680 m, with mooring lines spaced every 20 m, which reduced the running times to approximately 6 hours.

Two factors are believed to contribute to these long running times. First, the mooring lines were assigned a different EA, as they were expected to have a larger diameter due to the increased spacing of 20 m. This higher EA may cause the solver, which uses adaptive time stepping to ensure accuracy, to take smaller time steps. Second, the model involves large matrices due to the relatively fine mesh. These matrices can become very large, although many entries are zero. To improve efficiency, sparse matrices could be used. However, due to time constraints, the project team was unable to implement this optimisation in the model.

Due to the lengthy running times, the model has only been run under extreme conditions with high current velocities. Simulations with lower current inputs and higher significant wave heights have not been performed. Given the time constraints of the project duration, it is assumed that the higher current will have a more significant impact on the forces acting on the barrier than an increase in significant wave height.

Another limitation of the structural model concerns how the mooring lines are incorporated. Ideally, the stiffness of a mooring line, represented by its EA, would change based on its position. An attempt was made to implement this by instantly increasing the EA when the mooring line came under tension (i.e., upon reaching a certain deformation). However, the SciPy solver encountered issues with this approach. The sudden increase in EA caused convergence problems, as the solver could only manage such changes with extremely small time steps. A potential solution was to gradually increase the stiffness using a $tanh$ function, but this also proved ineffective, as the solver still failed to converge. Therefore, the mooring lines were modelled with a fixed length and an increased EA. However, since the length is fixed, this EA does not depend on the position of the mooring line but is a constant value. As mentioned before, the EA of the mooring lines has a higher value than the EA of the barrier.

Another consequence of not being able to adjust the EA of the mooring lines is the inability to manually select the anchoring points of the lines. If the EA could change based on the position of the mooring lines, certain lines could become tensioned earlier, allowing the barrier to take on specific shapes. These tailored shapes could help redirect the sargassum more effectively. However, since the current structural model cannot simulate this, it is not possible to evaluate the internal forces for different barrier configurations.

Lastly, the preset maximum length of the mooring lines introduces challenges for dynamic loading on the structure. Since the dynamic loading consistently acts in the same direction, the structure naturally moves in response to it. However, as the load decreases, the structure tries to return along the same path it initially followed. Due to the mooring lines being fixed at their maximum length, the barrier's return movement becomes inaccurate. This happens

because the mooring lines can only rotate around their anchor points, distorting the barrier's shape and reducing the accuracy of both the movements and the resulting tensions.

To address this issue, one solution is to apply the previously mentioned method of using mooring lines with adjustable stiffness. Another option is to model the mooring lines as consisting of multiple elements with additional nodes, allowing for a more accurate representation of their behaviour.

Force determination

Several simplifications have been made in determining the forcing on the barrier. First, the cross-sectional shape of the barrier has been simplified to that of a thin plate. It is assumed that the buoy on top contributes minimally to the drag force, as it is expected that the buoy 'rides' on top of the waves. However, this has not been empirically verified. In reality, the buoy may contribute more to the drag than currently assumed, which could result in a significant increase in the drag force.

Also, an assumption has been made regarding the location where wave particle velocities and accelerations are determined. Currently, these values are taken at the free surface as this is the most simple way to implement it into the model. This is a conservative approach, as velocities and accelerations decrease with depth. In reality, the lower parts of the barrier will experience less wave-induced force, as the velocities and accelerations used in the Morison Equation are smaller at a larger depth. Related to this is the fact that all nodes currently experience the forcing at the same time. However, in reality, this is not the case since the waves and current have an angle of incidence. This means that certain nodes will experience the forcing first, while other nodes will experience it later. This has been simplified in the model. Lastly, an assumption of a uniform current profile has been made, which may not be accurate and could significantly affect the forcing on the barrier.

9 Conclusion

This chapter presents the conclusions of the study, starting with separate conclusions of the hydrodynamic analysis, barrier design, and structural model. First, the key outcomes of the hydrodynamic study are addressed, followed by an examination of the conclusions drawn from the barrier design. Next, the results of the structural model are reviewed. Finally, a general conclusion is provided, summarising the overall insights from the entire study.

9.1. Hydrodynamic analysis

The main question that needs to be answered is: *"How does the position of the floating barrier influence the movement of sargassum at the coast of Puerto Morelos?"*. To answer this, it is first necessary to understand how sargassum behaves under the current flow conditions in the bay of Puerto Morelos. The analysis indicates that sargassum particles enter the lagoon primarily through reef areas. However, not all particles reach the shoreline, as gyres within the lagoon partially flush the sargassum back into the sea. These gyres are generated by outflows at the openings in the reef, specifically at the "gates" and the south channel. These four regions have an almost constant outflow, as explained in Section 3.1. Especially the big gate induces the strongest circulatory flow, redirecting the most sargassum towards the Yucatán Current, which transport the sargassum offshore.

These flow patterns, together with the flow along the barrier and the wave dissipation due to the reef, determine the optimal position and shape of a floating sargassum barrier along the coast of Puerto Morelos. The barrier is most effective when positioned on the southern and the northern reefs, with its ends aligned at the edges of the flushing areas to avoid interference with natural flushing processes. For a barrier designed to enhance the chance of redirecting sargassum back to the sea, the flow along the entire length of the barrier should be directed toward one of the flushing ends to prevent sargassum accumulation. In this way, the barrier can effectively intercept sargassum and redirect it offshore. Lastly, H_s, T_p and current velocities exert forces on the barrier. From a structural point of view, all three factors should be minimized to reduce the loads. The final decision for the optimal barrier location and orientation are listed as follows:

- Barrier 1: angle with respect to NSWE-axis: 33.7°, length: 2160 m, starting and ending coordinates are (513255, 2305038) and (514450, 2306850) respectively.
- Barrier 2: angle with respect to NSWE-axis: 28.2°, length: 1375 m, starting and ending coordinates are (516019, 2310687) and (516670, 2311900) respectively.

Based on the model results, it can be concluded that the position and orientation of a floating barrier are critical for effectively redirecting sargassum and protecting the shoreline of Puerto Morelos.

9.2. Barrier design

To determine the optimal barrier design for the Puerto Morelos area, various barrier designs, anchoring systems and materials were evaluated. In conjunction with identifying the environmental and operational conditions, an effective approach was developed. The analysis compared four types of floating barriers in Section 4.1, with Type II being selected for its flexibility and relatively low number of anchoring points, minimising disturbance to the local marine environment. The indirect anchoring system further reduced the need for additional anchoring points.

Material selection focused on durability, leading to the choice of HDPE and PVC for their resistance to UV degradation. Additionally, galvanized steel cables were chosen for strength throughout the barrier. Although nanocoatings showed promise in reducing maintenance, they were excluded from the final design due to their lack of proven real-world effectiveness. Section 4.4 highlighted potential material improvements, such as PMMA and innovative antifouling applications, but these were ultimately not integrated due to higher costs and the need for further testing in marine environments.

Section 4.5 focused on tailoring the final design specifically to the environmental conditions of Puerto Morelos. The local marine ecosystem, including sensitive coral reefs and seagrass beds, required a solution that minimised ecological impact while maintaining durability. By analysing wave forces and current velocities in Section 3.4, along with barrier types, anchoring systems and marine life considerations, the barrier was designed to be easily disassembled during extreme weather, while ensuring optimal performance. Additionally, the final design integrates flexibility in the anchoring system, allowing for efficient deployment and maintenance while protecting the local ecosystem.

9.3. Structural model

The primary structural research question posed was: ”How can a general structural model for a floating sargassum-catching barrier be developed and implemented?” Drawing on the findings and analyses presented in Chapter 5, Chapter 6 and Chapter 7 this question can now be addressed.

The core concept underlying the modelling of the sargassum barrier is its representation as a cable structure. This cable is supported by mooring lines and subjected to a distributed load consisting of wave and current-induced forces. Since obtaining an analytical solution for this dynamic problem is not possible, numerical methods are required. In this report, FEM was used. However, the nonlinear behaviour of a dynamic cable presents challenges in FEM, as explained in Chapter 5. The goal was to determine the internal forces in both the barrier and its mooring lines, enabling iterative improvements to the design dimensions.

The input for the structural model includes the environmental conditions of the Puerto Morelos area and the first iteration design specifications of the barrier. Using Airy wave theory and the Morison Equation, the forces acting on the barrier were calculated. It is important to note that several simplifications were made in order to calculate these forces. A significant assumption involves the simplification of the cross section of the barrier and thus its associated drag coefficient. This assumption has a considerable impact on the results. Ideally, the accuracy of the simplified cross section and drag coefficient would be tested empirically, but the project team lacks the resources to conduct such experiments.

Changes in input parameters result in outputs that are in line with the theoretical expectations of these adjustments. This indicates that any discrepancies in the results of the design unity checks are more likely to arise from input parameters rather than from flaws within the model itself.

9.4. General Conclusion

This study has developed and evaluated a comprehensive approach to design a floating barrier system aimed at intercepting sargassum along the coast of Puerto Morelos. By integrating hydrodynamic analysis, barrier design, and structural modelling, the study addressed key research questions concerning the optimal placement, design, and structural performance of the barrier.

The hydrodynamic analysis demonstrated that the position and alignment of the barrier significantly influence its effectiveness in redirecting sargassum offshore. By analysing flow patterns within the lagoon and along the barrier, the study identified the southern and northern reefs as optimal locations to position the barrier ends, thereby enhancing the natural flushing effect while minimising the accumulation of sargassum along the shoreline.

In the barrier design research, various structural and material considerations were assessed to optimize the system for durability and minimal ecological impact. Type II barrier design, supported by an indirect anchoring system, emerged as the preferred solution, offering structural flexibility while reducing the number of anchoring points and associated disturbances to sensitive marine ecosystems. Material choices, including HDPE, PVC, and galvanised steel cables, were selected based on their durability and resistance to marine conditions, while future improvements in antifouling technologies were identified for potential enhancement.

The structural model enabled detailed analysis of the internal forces within the barrier and its mooring system, utilising a FEM approach. For the dynamic and nonlinear nature of the problem, assumptions regarding barrier cross-sectional shape, drag coefficient and mooring lines were applied, yielding results aligned with theoretical expectations. While limitations in resources prevented empirical validation of these assumptions, the sensitivity of the model to input parameters indicated that any variations in results are likely due to environmental conditions rather than fundamental modelling errors.

In summary, the study has successfully provided a validated framework for designing a floating sargassum barrier, tailored to the hydrodynamic, environmental, and structural constraints of the Puerto Morelos region. This framework serves as a foundation for future improvements and field applications, with recommendations for further empirical validation to refine design parameters and enhance overall barrier performance.

10 Recommendations

This chapter outlines the recommendations based on the findings of this study. Suggestions are provided for effectively installing the barrier, ensuring optimal performance and efficiency. Additionally, recommendations are made for potential follow-up research to address areas that require further investigation. These recommendations aim to enhance both the practical implementation and the broader understanding of the system.

10.1. Practical recommendations

This research contains next to the theory, a practical view on how sargassum barriers should be designed. In this section, practical advice on implementing a barrier is given. The scope of the research, described in Section 1.1, is to protect the shore and redirect the sargassum into the sea. The design of a barrier across the entire Yucatán peninsula is neither realistic nor financially feasible. It is highly recommended, to analyse the flow of the area where future barriers are being built. The hydrodynamic analysis of the reef of Puerto Morelos is a perfect example of how flushing effects reduce the required barrier length. This saves materials, costs and implementation time.

When the barrier is taken out of the water for maintenance, it is recommended to carry out the following maintenance steps, ensuring a prolonged lifetime while minimizing risks of failure of the barrier.

- Thoroughly clean the barrier whenever it is taken out of the water. This helps remove accumulated biofouling, debris and salt deposits that could degrade the materials over time.
- When stored, keep the barrier dry and out of direct sunlight to avoid UV degradation and unnecessary wear. This is particularly important for materials like HDPE and PVC, which can become brittle after prolonged exposure to UV rays.
- Inspect galvanised steel cables for signs of pitting corrosion, especially in areas exposed to closed rusty seawater (CRS). If pitting corrosion is detected, take immediate action to repair or replace the affected cables, as this type of corrosion can severely weaken the structure over time.

10.2. Research recommendations

10.2.1. Hydrodynamic model

As discussed in Section 8.1, many input parameters in the flow and sargassum model remain uncertain, necessitating validation. This section recommends methods for establishing a more accurate representation of flow and sargassum transport. Additionally, further research on a real floating barrier is essential to analyse its interaction with sargassum.

Sargassum

One of the most important aspects of predicting transport of sargassum is establishing an accurate transport model of sargassum particles. As mentioned in Section 2.3, sargassum is modelled by introducing a passive tracer, which is based on many input parameters that have argued assumptions. The transport behaviour of sargassum can be validated by attaching GPS trackers to the sargassum mats offshore and comparing the GPS data with the modelled tracks. This is only possible when the flow patterns of the observed location are known, so it accurately describes the physical observation. Adding real-time flow conditions at the boundaries of the model highly increases the accuracy of the hydrodynamic results as well. Floating buoys that measure hydrodynamic conditions can obtain this field data. So far, satellite-detected sargassum is the most effective strategy for long-term monitoring. This monitoring method provides data that helps to predict sargassum movement in the future.

Floating barrier

The conclusions of this research are based on model results that describe only the flow patterns and corresponding sargassum movements along the coast of Puerto Morelos. The potential impact of a floating barrier on flow patterns within the reef lagoon remains unknown. Although this influence has been assumed negligible, it is recommended to test flow behaviour around a floating barrier. Introducing a prototype barrier in a wave flume allows for the examination of flow patterns around the barrier and enables the measurement of actual hydrodynamic forces exerted on it. This approach would also enable small-scale validation of the structural elements.

10.2.2. Barrier design

Claims on the effectiveness of the sargassum barriers of companies like Beach Bouncer lack scientific validation. Future research should focus on field trials that measure the sargassum capture rate of different barrier types under

real-world conditions, such as varying currents and wave forces. Standardised testing protocols should be developed to assess immediate and long-term effectiveness. These tests must be standardised based on the most dominant factors influencing their effectiveness and change these factors based on environmental conditions. Furthermore, research is needed to investigate their long-term durability, ensuring more sustainable solutions.

Additionally, future research should evaluate the long-term durability of PMMA in marine environments, providing data to support a cost-benefit analysis compared to HDPE. Similarly, while nanocoatings show promise for preventing biofouling and UV degradation, real-world effectiveness in marine conditions remains unknown. Field studies should assess their ability to reduce maintenance needs and extend material lifetimes.

Lastly, the ecological effects of sargassum barriers require continuous monitoring. Long-term studies should measure these impacts and assess how barrier placement and design can mitigate negative outcomes even further. These studies should focus on key ecological indicators, such as the impact of barriers on coral health and sea turtle nesting patterns, ensuring that barrier solutions balance effective sargassum management with ecological preservation. This monitoring is important for balancing effective sargassum management with ecological preservation, ensuring that the barrier solutions are sustainable for both marine life and coastal ecosystems.

10.2.3. Structural model

Given the challenges encountered with the computational efficiency of the model, future research should focus on optimising its performance. One option for improvement is the implementation of sparse matrices, which could significantly reduce computational time.

Further investigation into methods for adjusting mooring line stiffness and modelling the mooring lines with multiple elements and nodes, allowing a better representation of the mooring lines, also shows great potential for enhancing the accuracy of the dynamic response of the barrier. This could potentially be obtained by using a $tanh$ function to manage stiffness changes in the mooring lines

Moreover, to ensure a more accurate representation of the forces acting on the barrier, the drag coefficient should be empirically determined. This would lead to a better understanding of the interaction of the barrier with its environment and allow for more precise force calculations. Additionally, the hydrodynamic analysis together with multiple statistical methods, each with its own uncertainty, are used to obtain the forcing. More investigation in these uncertainties could result in a more realistic representation of the forcing.

Bibliography

[1] en. Oct. 2024. URL: https://cds-beta.climate.copernicus.eu/datasets/reanalysis-era5-single-levels?tab=overview.

[2] URL: https://mhkit-software.github.io/MHKiT/.

[3] Abasco. *About us | ABASCO*. URL: https://www.abasco.com/about-us.html.

[4] Abasco. *Seaweed Control Barrier & Sargassum Containment Boom - Aquatic Plant Barriers | ABASCO*. URL: https://www.abasco.com/sargassum-seaweed-boom.html.

[5] United States Environmental Protection Agency. URL: https://www.epa.gov/habs/management-methods-sargassum-inundation-events-sies.

[6] Nina Maria Ainali, Dimitrios N. Bikiaris, and Dimitra A. Lambropoulou. "Aging effects on low- and high-density polyethylene, polypropylene and polystyrene under UV irradiation: An insight into decomposition mechanism by Py-GC/MS for microplastic analysis". In: *Journal of Analytical and Applied Pyrolysis* 158 (Sept. 2021), p. 105207. DOI: 10.1016/j.jaap.2021.105207. URL: https://www.sciencedirect.com/science/article/pii/S0165237021001935.

[7] G. Akovali. *Plastic materials: polyvinyl chloride (PVC)*. Jan. 2012, pp. 23–53. DOI: 10.1533/9780857096357.23. URL: https://www.sciencedirect.com/science/article/pii/B9780857091222500024.

[8] Umar Ali, Khairil Juhanni Bt. Abd Karim, and Nor Aziah Buang. "A Review of the Properties and Applications of Poly (Methyl Methacrylate) (PMMA)". In: *Polymer Reviews* 55.4 (June 2015), pp. 678–705. DOI: 10.1080/15583724.2015.1031377. URL: https://doi.org/10.1080/15583724.2015.1031377.

[9] G Athié et al. "Yucatan Current variability through the Cozumel and Yucatan channels". In: *Ciencias Marinas* 37 (Aug. 2011), pp. 471–492. DOI: 10.7773/cm.v37i4A.1794.

[10] Duane Bennish. *Personal Communication*. Email conversation with the author. Discussed barrier types for Sargassum barrier project. Sept. 2024.

[11] Chun-Wei Bi and Tiao-Jian Xu. "Numerical Study on the Flow Field Around a Fish Farm in Tidal Current". In: *Turkish Journal of Fisheries and Aquatic Sciences* 18.5 (May 2018), pp. 705–716. URL: https://www.trjfas.org/abstract.php?id=1211.

[12] A. C. Biesheuvel. "Effectiveness of floating breakwaters: Wave attenuating floating structures". Available at http://resolver.tudelft.nl/uuid:aa142b5d-b11d-4c88-9ced-acd8ef8628a2. Master's thesis. Delft: TU Delft, 2013.

[13] Kristi Blokhin. en. URL: https://enterprise.shutterstock.com/image-photo/closeup-seaweed-on-beach-sand-coastline-2128019234.

[14] D. Braun and S.T. Rabie. "Photostabilizing effect of some thermal stabilizers for poly(vinyl chloride) in the presence of filler". In: *Journal of Vinyl and Additive Technology* 15.4 (Oct. 2009), pp. 224–228. DOI: 10.1002/vnl.20206. URL: https://doi.org/10.1002/vnl.20206.

[15] Longsheng Chen and Zewei Lin. "Polyethylene: Properties, Production and Applications". In: *2021 3rd International Academic Exchange Conference on Science and Technology Innovation (IAECST)* (Dec. 2021). DOI: 10.1109/iaecst54258.2021.9695646. URL: https://doi.org/10.1109/iaecst54258.2021.9695646.

[16] C. Coronado et al. "On the circulation in the Puerto Morelos fringing reef lagoon." In: *Coral Reefs* 26 (2007), pp. 149–163. DOI: 10.1007/s00338-006-0175-9.

[17] X. A. Cortez. "Modelación numérica de la hidrodinámica en la Laguna Arrecifal de Puerto Morelos". In: (2024).

[18] Carina I.C. Crucho. "Silica coatings: From nanostructures to biological entities". In: *Applied Materials Today* 38 (Apr. 2024), p. 102179. DOI: 10.1016/j.apmt.2024.102179. URL: https://doi.org/10.1016/j.apmt.2024.102179.

[19] Karollyne Gomes De Castro Monsores et al. "Influence of ultraviolet radiation on polymethylmethacrylate (PMMA)". In: *Journal of Materials Research and Technology* 8.5 (Sept. 2019), pp. 3713–3718. DOI: 10.1016/j.jmrt.2019.06.023. URL: https://www.sciencedirect.com/science/article/pii/S2238785419305861.

[20] Deltares. *Delft3D FLOW*. 4.05. Deltares. Delft, Oct. 2024.

[21] M. A. Donelan et al. "On the limiting aerodynamic roughness of the ocean in very strong winds". In: *Geophysical Research Letters* 31.18 (Sept. 2004). DOI: 10.1029/2004gl019460.

[22] Elastec. *About Elastec | History of Elastec American Marine*. Feb. 2024. URL: https://www.elastec.com/about-elastec/.

[23] Elastec. *Beach Bouncer | Weed and Debris barrier*. Unpublished document. 2024.

[24] Editor Engineeringtoolbox. *The Engineering ToolBox*. Mar. 2024. URL: https://www.engineeringtoolbox.com/.

[25] enviro. *ABOUT US | ENVIRO-USA*. URL: https://enviro-usa.com/about-enviro-usa/.

[26] Odd Magnus Faltinsen. *Sea loads on ships and offshore structures*. Cambridge University Press, 1999.

[27] *Finally a solution to eradicate the algae sargasse – AlgeaNova*. URL: https://algeanova.com/finally-a-solution-to-eradicate-the-algae-sargasse/.

[28] Leroy Gardner. "The use of stainless steel in structures". In: *Progress in Structural Engineering and Materials* 7.2 (Feb. 2005), pp. 45–55. DOI: 10.1002/pse.190. URL: https://doi.org/10.1002/pse.190.

[29] Aridane G. González et al. "Redox interactions of Fe and Cu in seawater". In: *Marine Chemistry* 179 (Jan. 2016), pp. 12–22. DOI: 10.1016/j.marchem.2016.01.004. URL: https://doi.org/10.1016/j.marchem.2016.01.004.

[30] Google. *Google Earth*. 2024. URL: https://earth.google.com/web/@20.85930143,-86.81985859,-8.94882695a,54419.19358978d,30.72251577y,0h,0t,0r/data=CgRCAggBOgMKATBKCAiamfPoBRAA.

[31] Antimo Graziano, Shaffiq Jaffer, and Mohini Sain. "Review on modification strategies of polyethylene/polypropylene immiscible thermoplastic polymer blends for enhancing their mechanical behavior". In: *Journal of Elastomers Plastics* 51.4 (June 2018), pp. 291–336. DOI: 10.1177/0095244318783806. URL: https://doi.org/10.1177/0095244318783806.

[32] Erika Gress et al. *The Mesoamerican Reef*. Jan. 2019, pp. 71–84. DOI: 10.1007/978-3-319-92735-0\{_}5. URL: https://doi.org/10.1007/978-3-319-92735-0_5.

[33] *Heavy Duty | ENVIRO-USA*. URL: https://enviro-usa.com/heavy-duty-seaweed-barrier/.

[34] *High density polyethylene prices, monitor, news demand*. July 2024. URL: https://www.chemanalyst.com/Pricing-data/hdpe-7.

[35] Champ Internet. *Emergency Oil Spill Clean-up amp; Removal Company | Acme Environmental*. Nov. 2022. URL: https://acmeboom.com/about-us/.

[36] Susan Jackson. *How to control Sargassum seaweed*. Jan. 2024. URL: https://www.elastec.com/how-to-control-sargassum-seaweed/.

[37] The Wall Street Journal. *This Cancún Resort Fights 20,000 Tons of Invasive Seaweed Each Year | WSJ Booked*. June 2024. URL: https://www.youtube.com/watch?v=31d8c-9tKbk.

[38] Santosh Kumar et al. "Nanocoating Is a New Way for Biofouling Prevention". In: *Frontiers in Nanotechnology* 3 (Nov. 2021). DOI: 10.3389/fnano.2021.771098. URL: https://doi.org/10.3389/fnano.2021.771098.

[39] Clint LaBounty. *Personal Communication*. Email conversation with the author. Discussed barrier types for Sargassum barrier project. Sept. 2024.

[40] Katie Langin. "Seaweed masses assault Caribbean islands". en. In: *Science* 360.6394 (June 2018), pp. 1157–1158.

[41] R. Lanzafame. *MUDE Textbook*. 2024. URL: https://mude.citg.tudelft.nl/2023/book/intro.html.

[42] Robert Lanzafame. *CIEM42X0 Probabilistic Design*. 2024. URL: https://tudelft-citg.github.io/HOS-prob-design-24/.

[43] James H. Lindsay and Thomas J. O'Keefe. *Electrogalvanizing*. Jan. 1994, pp. 165–228. DOI: 10.1007/978-1-4899-1733-1\{_}4. URL: https://doi.org/10.1007/978-1-4899-1733-1_4.

[44] Shuan Liu et al. "The Corrosion Performance of Galvanized Steel in Closed Rusty Seawater". In: *International Journal of Corrosion* 2013 (Jan. 2013), pp. 1–9. DOI: 10.1155/2013/267353. URL: https://doi.org/10.1155/2013/267353.

[45] Zoe Loffler and Andrew S. Hoey. "Canopy□forming macroalgal beds (Sargassum) on coral reefs are resilient to physical disturbance". In: *Journal of Ecology* 106.3 (Oct. 2017), pp. 1156–1164. DOI: 10.1111/1365-2745.12875. URL: https://doi.org/10.1111/1365-2745.12875.

[46] Clifford Louime, Jodany Fortune, and Gary Gervais. "lt;igt;Sargassumlt;/igt; Invasion of Coastal Environments: A Growing Concern". In: *American Journal of Environmental Sciences* 13.1 (Jan. 2017), pp. 58–64. DOI: 10.3844/ajessp.2017.58.64. URL: https://doi.org/10.3844/ajessp.2017.58.64.

[47] L.C. Mendes et al. "Mechanical, thermal and microstructure evaluation of HDPE after weathering in Rio de Janeiro City". In: *Polymer Degradation and Stability* 79.3 (Mar. 2003), pp. 371–383. DOI: 10.1016/s0141-3910(02)00337-3. URL: https://doi.org/10.1016/s0141-3910(02)00337-3.

[48] *Mesh Boom Beach Protection Seaweed | DESMI - Make life flow*. URL: https://www.desmiro-clean.com/products-solutions-library/mesh-boom/.

[49] Tiffany Z. Monaco. *Experimental Studies of Scale Model Drag Embedment Anchors (DEAs) Subjected to Impulse Forces*. URL: https://surface.syr.edu/cie_thesis/4/?utm_source=surface.syr.edu%2Fcie_thesis%2F4&utm_medium=PDF&utm_campaign=PDFCoverPages.

[50] Antonio Ortiz. *Control Anual Moon Palace*. Data provided by Moon Palace. Sept. 2024.

[51] Antonio Ortiz. *Personal Communication*. In field presentation by the author. Provided insights on the design specifications of the floating barriers. Sept. 2024.

[52] Sabrina M. Parra et al. "Seasonal variability of saltwater intrusion at a point-source submarine groundwater discharge". In: *Limnology and Oceanography* 61.4 (2016), pp. 1245–1258.

[53] *Poly methyl methacrylate (PMMA) prices, news, monitor*. July 2024. URL: https://www.chemanalyst.com/Pricing-data/polymethyl-methacrylate-50.

[54] *Poly methyl methacrylate (PMMA) prices, news, monitor*. July 2024. URL: https://www.chemanalyst.com/Pricing-data/polymethyl-methacrylate-50.

[55] Violeta Popescu et al. "The characterization of recycled PMMA". In: *Journal of Alloys and Compounds* 483.1-2 (Feb. 2009), pp. 432–436. DOI: 10.1016/j.jallcom.2008.08.148. URL: https://doi.org/10.1016/j.jallcom.2008.08.148.

[56] Nathan F. Putman et al. "Improving transport predictions of pelagic Sargassum". In: *Journal of Experimental Marine Biology and Ecology* 529 (2020), p. 151398.

[57] Nathan F. Putman et al. "Improving transport predictions of pelagic Sargassum". In: *Journal of Experimental Marine Biology and Ecology* 529 (2020), pp. 151–398. ISSN: 0022-0981. DOI: https://doi.org/10.1016/j.jembe.2020.151398. URL: https://www.sciencedirect.com/science/article/pii/S0022098120300125.

[58] *QUINTANA TOO STARTS INSTALLATION OF FLOATING BARRIER AGAINST SARGASSUM.* URL: https://rentalpropertyinvestingrivieramaya.com/barrier-against-sargassum.html.

[59] Rosa Rodríguez-Martínez et al. "Environmental state and tendencies of the Puerto Morelos CARICOMP site, Mexico". In: *Rev. biol. trop* 58 (Oct. 2010), pp. 23–43. URL: https://www.researchgate.net/publication/49815323_Environmental_state_and_tendencies_of_the_Puerto_Morelos_CARICOMP_site_Mexico.

[60] Fabián A. Rodríguez-Zaragoza and Jesús E. Arias-González. "Coral biodiversity and bio-construction in the northern sector of the mesoamerican reef system". In: *Frontiers in Marine Science* 2 (Mar. 2015). DOI: 10.3389/fmars.2015.00013. URL: https://doi.org/10.3389/fmars.2015.00013.

[61] Jantien Rutten et al. "Beaching and Natural Removal Dynamics of Pelagic Sargassum in a Fringing□Reef Lagoon". In: *Journal of Geophysical Research Oceans* 126.11 (Nov. 2021). DOI: 10.1029/2021jc017636. URL: https://doi.org/10.1029/2021jc017636.

[62] Alok K. Sahu, K. Sudhakar, and R.M. Sarviya. "Influence of U.V light on the thermal properties of HDPE/Carbon black composites". In: *Case Studies in Thermal Engineering* 15 (Nov. 2019), p. 100534. DOI: 10.1016/j.csite.2019.100534. URL: https://doi.org/10.1016/j.csite.2019.100534.

[63] *Sargassum containment barriers | Beach Trotters*. URL: https://en.beach-trotters.com/products/sargassum-containment-barriers.

[64] Franck Schoefs, Arash Bakhtiari, and Hamed Ameryoun. "Evaluation of Hydrodynamic Force Coefficients in Presence of Biofouling on Marine/Offshore Structures, a Review and New Approach". In: *Journal of Marine Science and Engineering* 10.5 (Apr. 2022), p. 558. DOI: 10.3390/jmse10050558. URL: https://doi.org/10.3390/jmse10050558.

[65] S.M.A. Shibli, B.N. Meena, and R. Remya. "A review on recent approaches in the field of hot dip zinc galvanizing process". In: *Surface and Coatings Technology* 262 (Dec. 2014), pp. 210–215. DOI: 10.1016/j.surfcoat.2014.12.054. URL: https://doi.org/10.1016/j.surfcoat.2014.12.054.

[66] M. J. Tucker. *Waves in ocean engineering*. Chichester: Ellis Horwood Ltd., 1991.

[67] Brigitta I. van Tussenbroek et al. "Severe impacts of brown tides caused by Sargassum spp. on near-shore Caribbean seagrass communities". In: *Marine Pollution Bulletin* 122.1 (2017), pp. 272–281. ISSN: 0025-326X. DOI: https://doi.org/10.1016/j.marpolbul.2017.06.057. URL: https://www.sciencedirect.com/science/article/pii/S0025326X17305374.

[68] UNAM. *Datos Actuales Estación Puerto Morelos, Quintana Roo. México*. 2020. URL: https://sammo.icmyl.unam.mx/.

[69] Abigail Uribe-Martínez et al. "Multiscale distribution patterns of pelagic rafts of sargasso (Sargassum spp.) in the Mexican Caribbean (2014–2020)". In: *Frontiers in Marine Science* 9 (2022). ISSN: 2296-7745. DOI: 10.3389/fmars.2022.920339. URL: https://www.frontiersin.org/journals/marine-science/articles/10.3389/fmars.2022.920339.

[70] Mengqiu Wang et al. “Remote Sensing of Sargassum Biomass, Nutrients, and Pigments”. In: *Geophysical Research Letters* 45.22 (July 2018). DOI: 10.1029/2018gl078858. URL: https://doi.org/10.1029/2018gl078858.

[71] Terry Ward. *What a massive sargassum bloom could mean for your Florida, Caribbean, or Mexico Vacation*. Apr. 2024. URL: https://www.afar.com/magazine/what-is-sargassum-and-how-will-it-affect-your-beach-vacation.

[72] Xiuqin Xiang et al. “Effect of the combination of a benzophenone□type ultraviolet absorber with thermal stabilizers on the photodegradation of poly(vinyl chloride)”. In: *Journal of Vinyl and Additive Technology* 16.1 (Jan. 2010), pp. 23–32. DOI: 10.1002/vnl.20222. URL: https://doi.org/10.1002/vnl.20222.

[73] Joanne Yip and Wing-Yu Chan. *Textile fibers and fabrics*. Jan. 2020, pp. 47–72. DOI: 10.1016/b978-0-12-819492-8.00003-x. URL: https://www.sciencedirect.com/topics/materials-science/polyethylene.

[74] Paula Andrea Zapata-Ramírez et al. “Accuracy of IKONOS for mapping benthic coral-reef habitats: a case study from the Puerto Morelos Reef National Park, Mexico”. In: *International Journal of Remote Sensing* 34.9-10 (Oct. 2012), pp. 3671–3687. DOI: 10.1080/01431161.2012.716922. URL: https://doi.org/10.1080/01431161.2012.716922.

[75] X.G. Zhang and E.M. Valeriote. “Galvanic protection of steel and galvanic corrosion of zinc under thin layer electrolytes”. In: *Corrosion Science* 34.12 (Dec. 1993), pp. 1957–1972. DOI: 10.1016/0010-938x(93)90053-j. URL: https://doi.org/10.1016/0010-938x(93)90053-j.

[76] X U Zhao et al. “Solid-phase photocatalytic degradation of polyethylene plastic under UV and solar light irradiation”. In: *Journal of Molecular Catalysis A Chemical* 268.1-2 (May 2007), pp. 101–106. DOI: 10.1016/j.molcata.2006.12.012. URL: https://www.sciencedirect.com/science/article/pii/S1381116906014270.

[77] Y. Zou, J. Wang, and Y.Y. Zheng. “Electrochemical techniques for determining corrosion rate of rusted steel in seawater”. In: *Corrosion Science* 53.1 (Sept. 2010), pp. 208–216. DOI: 10.1016/j.corsci.2010.09.011. URL: https://doi.org/10.1016/j.corsci.2010.09.011.

[78] R. Zuraimi et al. *Tensile Strength Analysis of High Density Polyethylene for Injection Moulded Parts*. Oct. 2017. URL: https://jamt.utem.edu.my/jamt/article/view/2860.

A
Stakeholder analysis

Table A.1: Stakeholder analysis

	Stakeholder	Comments
1	University ENES	The university is a key stakeholder in this project, with an academic interest in developing a scientifically sound approach to design sargassum barriers tailored to specific locations. The university aims to create a methodology based on research, environmental factors and engineering principles that can be applied to various coastal regions. By supporting the project, the university contributes to scientific knowledge in marine engineering and ecosystem management. The results of this research could also provide valuable insights for future academic work and publications.
2	Hotel industry	The tourism sector, particularly hotels, is heavily impacted by the influx of sargassum. The aesthetics of beaches are what encourage visitors to come to the hotels. The sargassum discourages visitors from visiting. Hotels rely on clean beaches to attract tourists, making them a key stakeholder in sargassum management. Many hotels have taken part in manual cleanup efforts and would benefit from sustainable, long-term solutions like barriers.
3	Local government (Municipality of Puerto Morelos)	Local governments are primarily responsible for managing the collection and removal of sargassum, which impacts public spaces and tourism infrastructure. They play a key role in coordinating cleanup efforts, enforcing regulations, and ensuring the economic stability of coastal communities. Their focus is on finding cost-effective and environmentally sustainable solutions to address the ongoing sargassum problem. They have the power to grant permits to build barriers.
4	National government	The national government is involved at a higher policy level, ensuring that regulations are in place to manage environmental impacts and support industries like tourism and fishing. They also oversee funding for larger-scale cleanup and barrier-building projects, research efforts, and international cooperation on sargassum issues.
5	Barrier producers	Companies that manufacture and deploy sargassum barriers are key stakeholders, as they provide the technological solutions necessary to address the problem. Their involvement includes offering expertise on barrier design, materials, and installation, and they have a direct interest in the project's success for further business opportunities.
6	Tourists	Tourists visiting the affected regions are stakeholders due to their direct influence on the local economy. The presence of sargassum deters tourism, and visitors expect clean, attractive beaches. sargassum barriers would improve the beach experience, making the location more appealing for tourists and benefiting the local economy.
7	Fishing industry	sargassum can disrupt local fishing industry by harming marine life. The fishing industry relies on healthy marine ecosystems and clear access to the ocean for sustainable fishing practices. Effective sargassum management would help prevent these disruptions, ensuring the livelihoods of those working in fishing industry.
8	Local businesses	Small businesses that rely on tourism and beach users, such as restaurants, shops, and service providers, are impacted by declining tourism due to sargassum. These businesses benefit directly from sargassum management solutions, which can restore beach aesthetics and increase visitor numbers.
9	Environmental NGO	Environmental non-governmental organisations are invested in the preservation of marine ecosystems. They may advocate for sustainable solutions to sargassum management that minimise harm to the environment and biodiversity. It is critical for them that barrier systems are investigated ensuring that any intervention is ecologically sound.
10	Recreational water users	Individuals involved in water sports, diving, and boating are affected by the presence of sargassum, which can impede their activities. These stakeholders may support barrier solutions that keep waterways clear, maintaining the viability of recreational activities that contribute to the local economy.
11	sargassum harvesting companies	Companies that see value in sargassum for products like biofuels, fertilizers, or animal feed would have an interest in barrier deployment to facilitate collection. These stakeholders could potentially turn a problem into an opportunity by using sargassum as a resource.

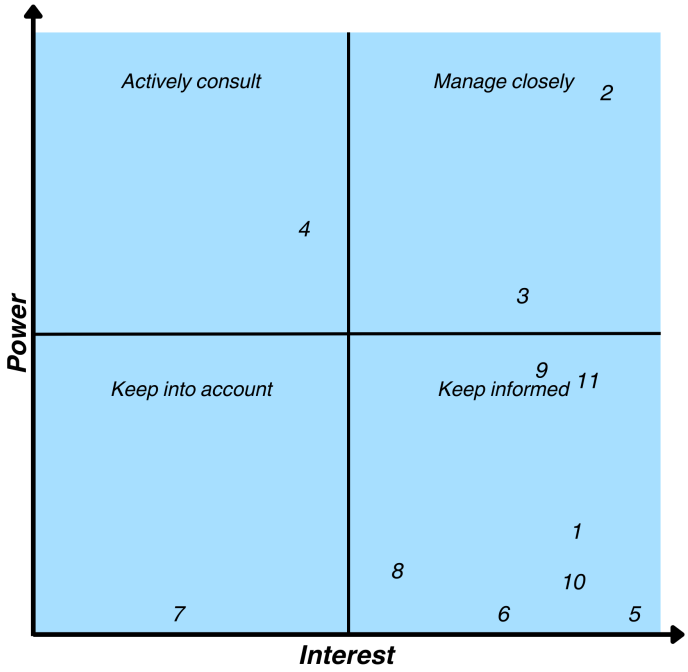

Figure A.1: Power interest grid stakeholder analysis.

B
Extreme Value Analysis and wind roses

This section elaborates on the EVA analysis. For this analysis, a POT is used. This method determines a threshold value with an MRL plot. Since this is a graphical method, the chosen threshold value is based on a visual estimation.[42] Figure B.1 displays the MRL plot, showing a quasi-linear trend between threshold values of 1.1 m and 1.8 m. Within this range, the threshold value is set at 1.7 m, as this value balances the need to capture a sufficient number of extreme events (peak values) in the POT method while considering the total amount of data points. Setting a threshold lower than 1.7 m results in an excessive number of peaks.

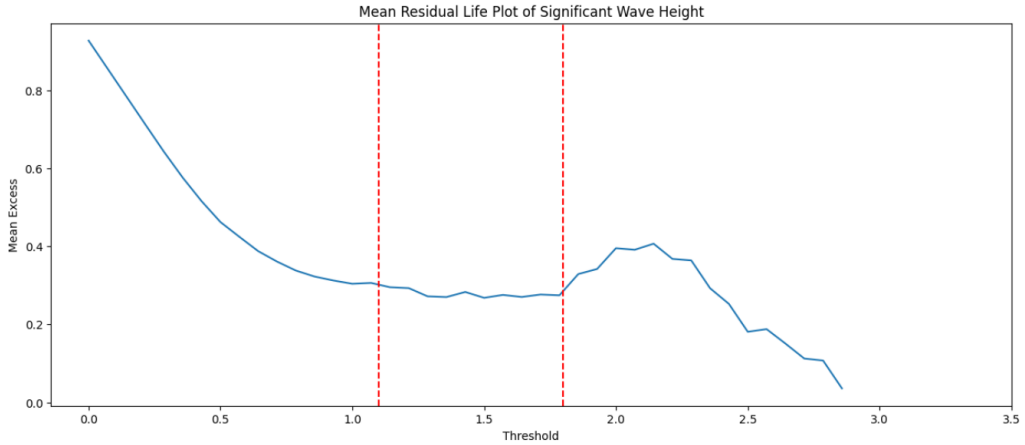

Figure B.1: Mean Residual Life of H_s, based on a 10-year time series at Puerto Morelos.

In addition to the threshold parameter, a 24-hour declustering time is applied. This declustering time is selected to ensure that the peak values are independent. Ensuring independence is crucial because the peak values must be independent and identically distributed (i.i.d.) to generate a representative and unbiased distribution of the peak significant wave heights. Furthermore, peak values exceeding three meters are excluded from the dataset, as these correspond to hurricane conditions. In Chapter 4, a further explanation is given why these conditions are neglected in our design. The resulting time series and corresponding peaks are shown in Figure B.2. The remaining Probability Density Function (PDF) of the peaks is given in Figure B.3, which aids in selecting an appropriate probability distribution for the data.

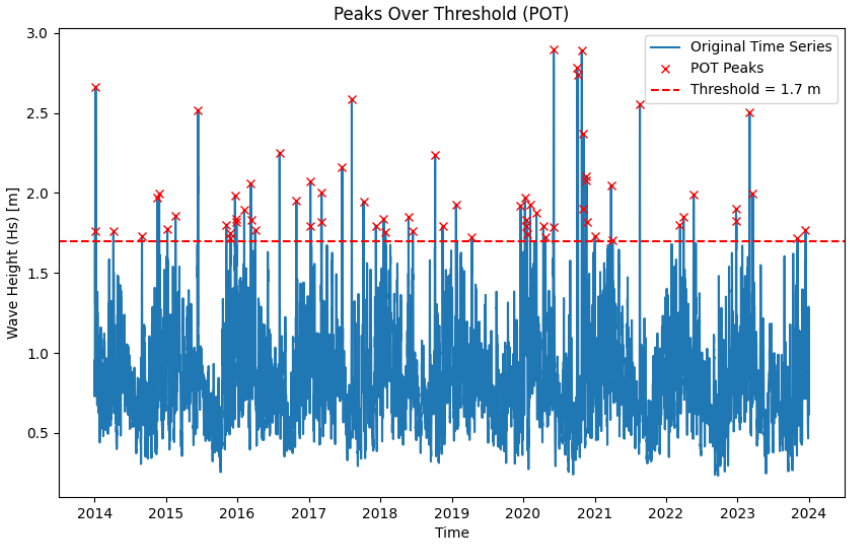

Figure B.2: Peaks Over Threshold H_s, based on a 10-year time series at Puerto Morelos.

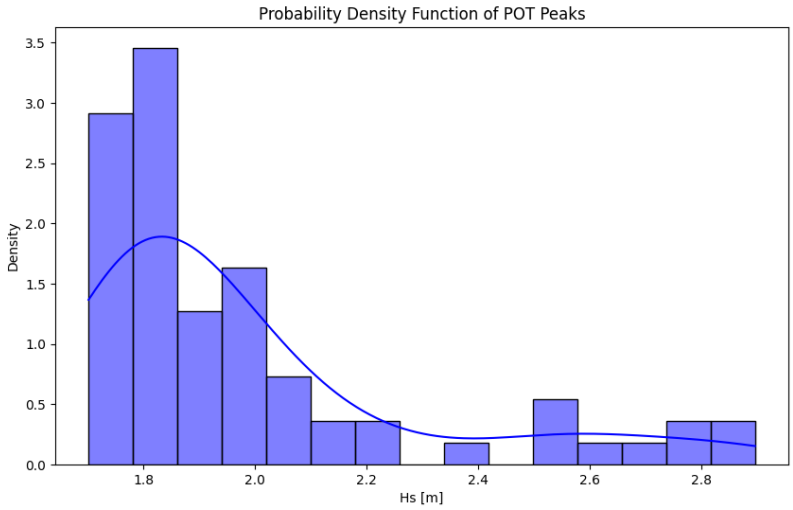

Figure B.3: Extreme Value Analysis: Probability Density Function of H_s.

With a Pareto extreme value distribution, multiple fits are obtained using standard probability distributions. These fitted distributions are presented together in Figure B.4, where both the PDF and the cumulative distribution functions (CDFs) are plotted. This shows which probability distribution corresponds with the PDF of the H_s values.

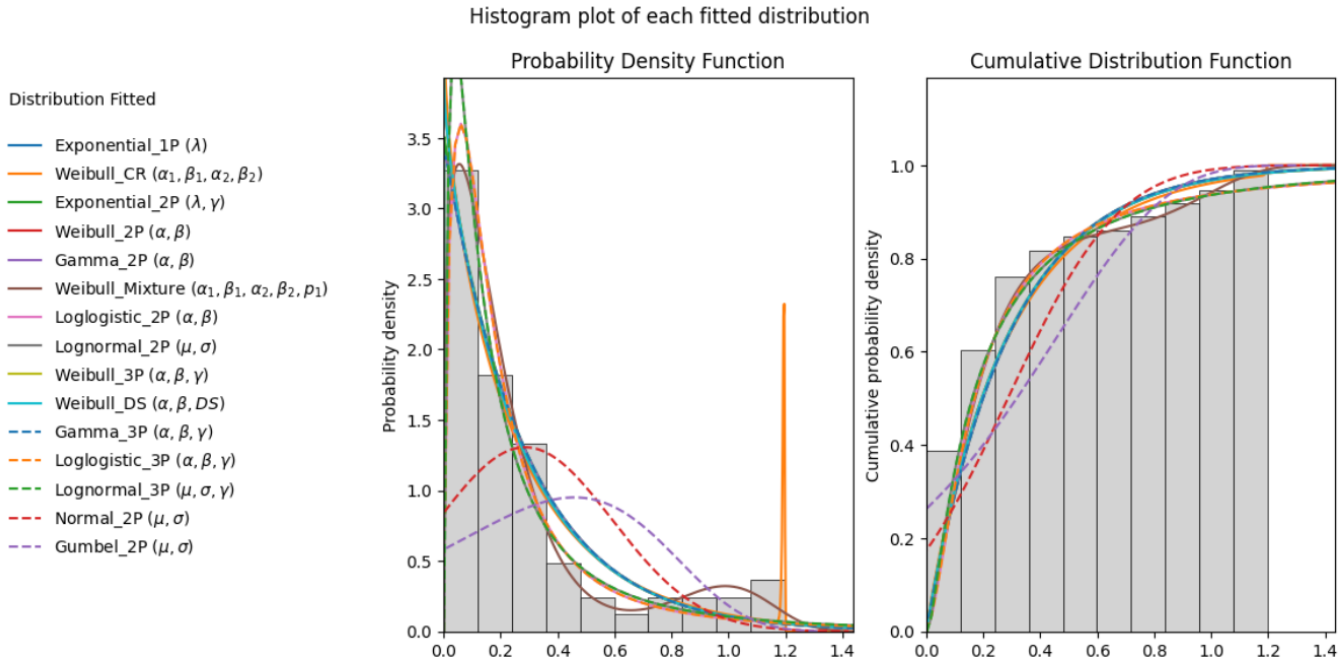

Figure B.4: Fitting probability distributions on the Puerto Morelos H_s data of a 10-year time series[1].

According to a Mean Squared Error (MSE) calculation an exponential distribution fits the data the best. This distribution is shown in Figure B.5. From the analysed dataset, 69 peaks were obtained from 21902 values for significant wave height, covering a timespan of ten years. This corresponds to approximately 7 peaks per year. The exceedance probability for a 10-year return period is calculated as $p = \frac{1}{10 \cdot 7}$. Therefore, the 10-year return level for the significant wave height, $H_{s,10}$, is at $1 - p = 98.6\%$. This results in an estimated return level for $H_{s,10}$ of 2.91 m, when an exponential distribution is used. The choice for a 10-year return period is motivated in Section 4.1.5.

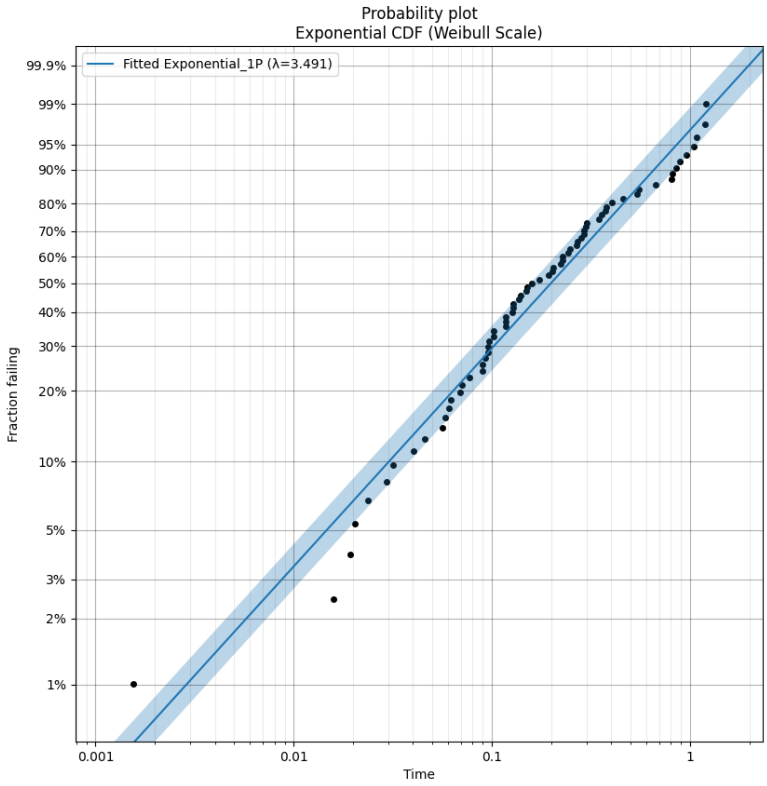

Figure B.5: Extreme Value Analysis: Fitted distribution of Exponential CDF.

Thereafter, the peak wave period (T_p) can be determined using the correlation between H_s and T_z. The dataset provides the T_z, for each (H_s). This correlation is visible in Figure B.6. Two distinct trends are observed. The data for H_s incorporates both wind-driven waves and swell. In the Puerto Morelos region, swell-driven waves are of primary interest, as the area is dominated by the propagation of swell generated in the Caribbean basin by eastern trade winds.[16] To determine the value of T_z, a line is drawn through the centre of the swell-driven wave data points. Extrapolation of the line shown in Figure B.6 shows that for an H_s value of 2.91 m, T_z is 10.4 s. The peak wave period (T_p) is then derived from T_z using Equation B.1 [66], which results in a T_p of 13 s. The wind speed (u_{wind}) is also determined with a scatter plot, giving again the H_s values with their corresponding u_{wind}. The resulting wind speed is 17.5 $\mathrm{m/s}$, obtained from Figure B.7.

$$T_p = 1.29 \cdot T_z \tag{B.1}$$

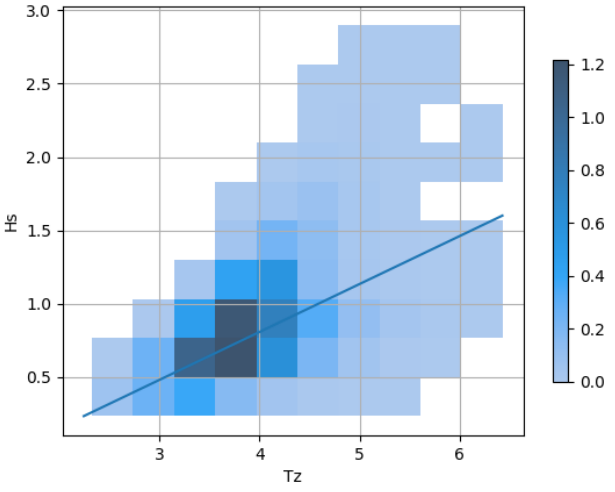

Figure B.6: Scatterplot of H_s and T_z from a 10-year time series at Puerto Morelos[1].

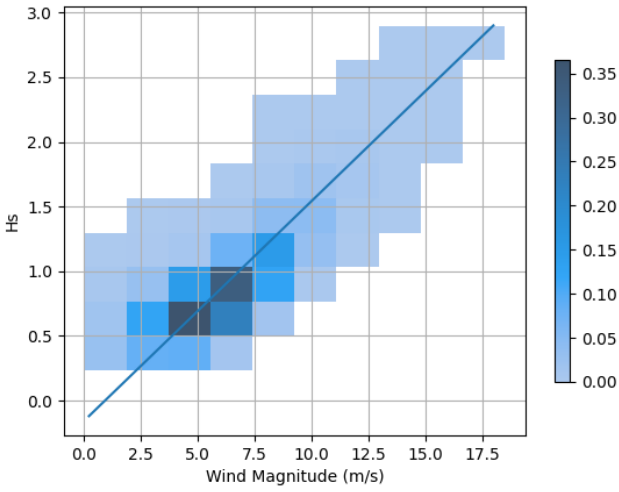

Figure B.7: Scatterplot of H_s and wind magnitude from a 10-year time series at Puerto Morelos[1]

For the directions of the incoming wind and wave, the average of all peaks is used as input. The results of the roses are shown in Figure B.8 and Figure B.9 respectively. This gives a wind direction of 50.6° (northeast) and an incoming wave direction of 86.3° (east).

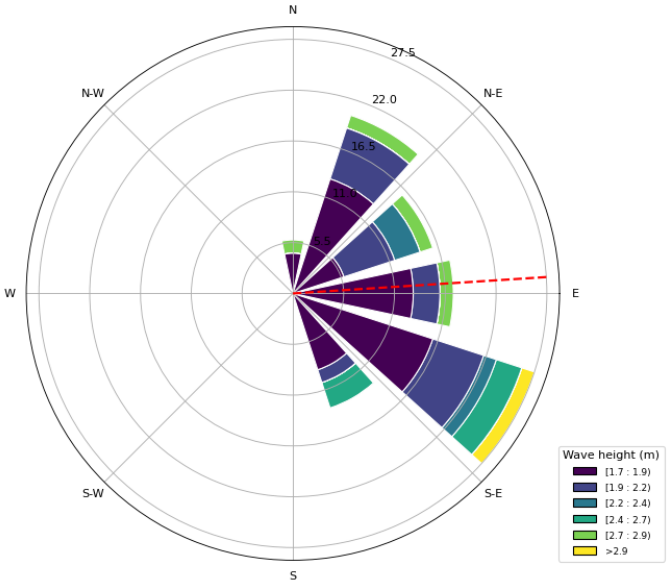

Figure B.8: Wave rose: hurricane conditions excluded (H_s < 3 m).

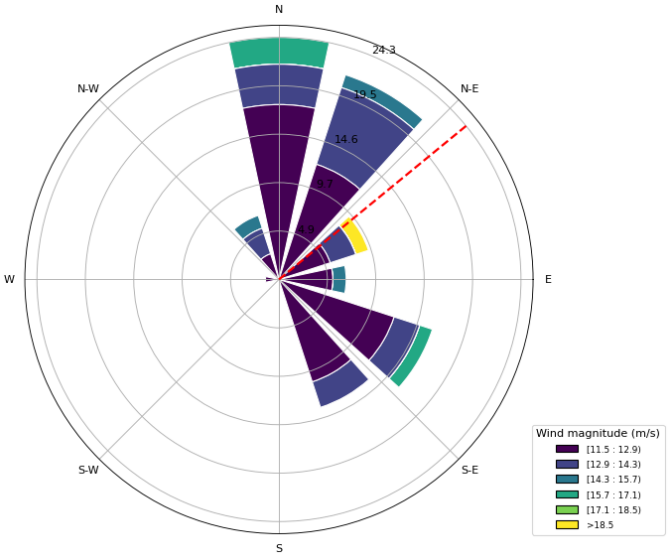

Figure B.9: Wind rose: hurricane conditions excluded (H_s < 3 m).

C
Figures flow analysis

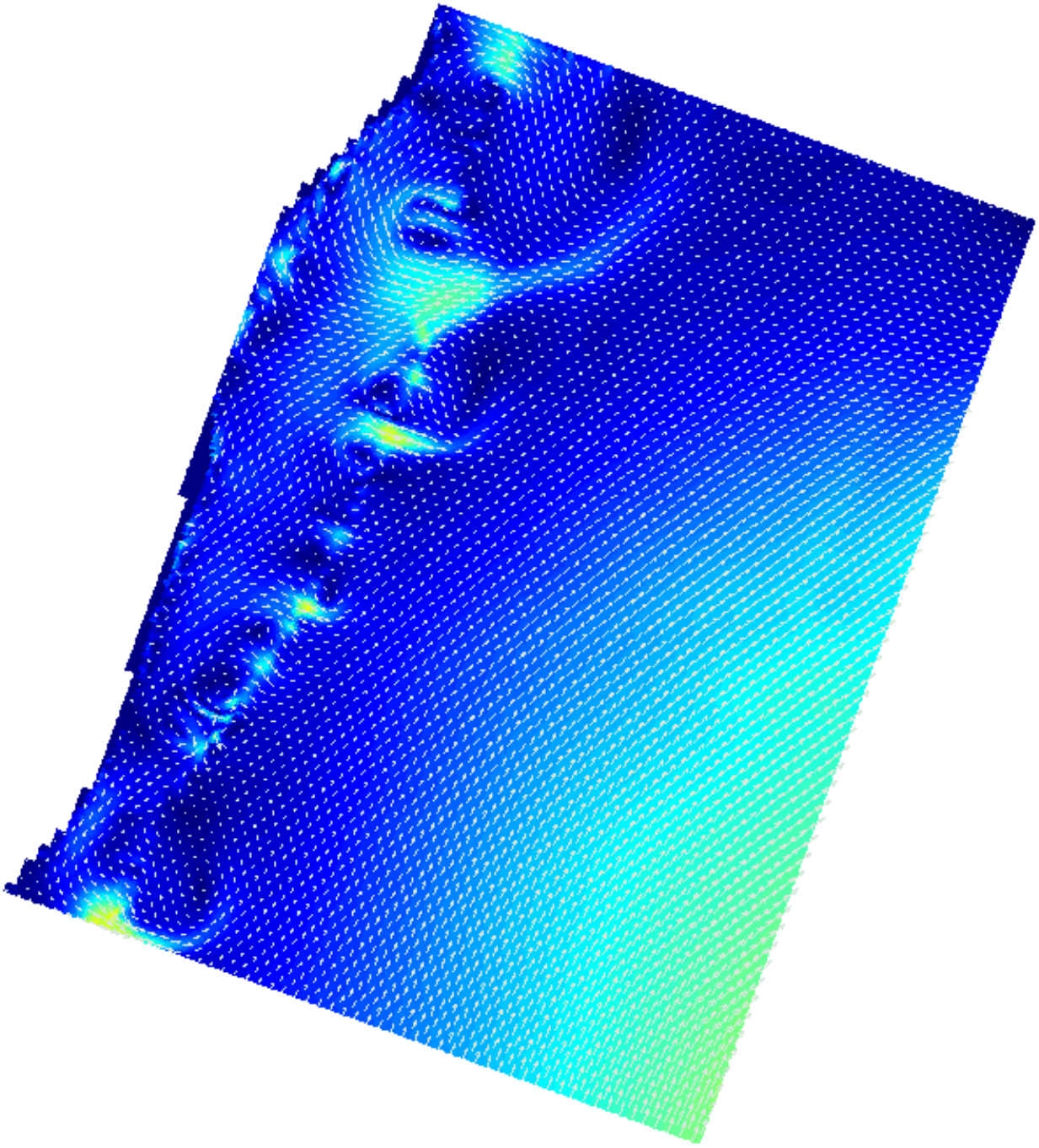

Figure C.1: Flow on TOI of condition 1.

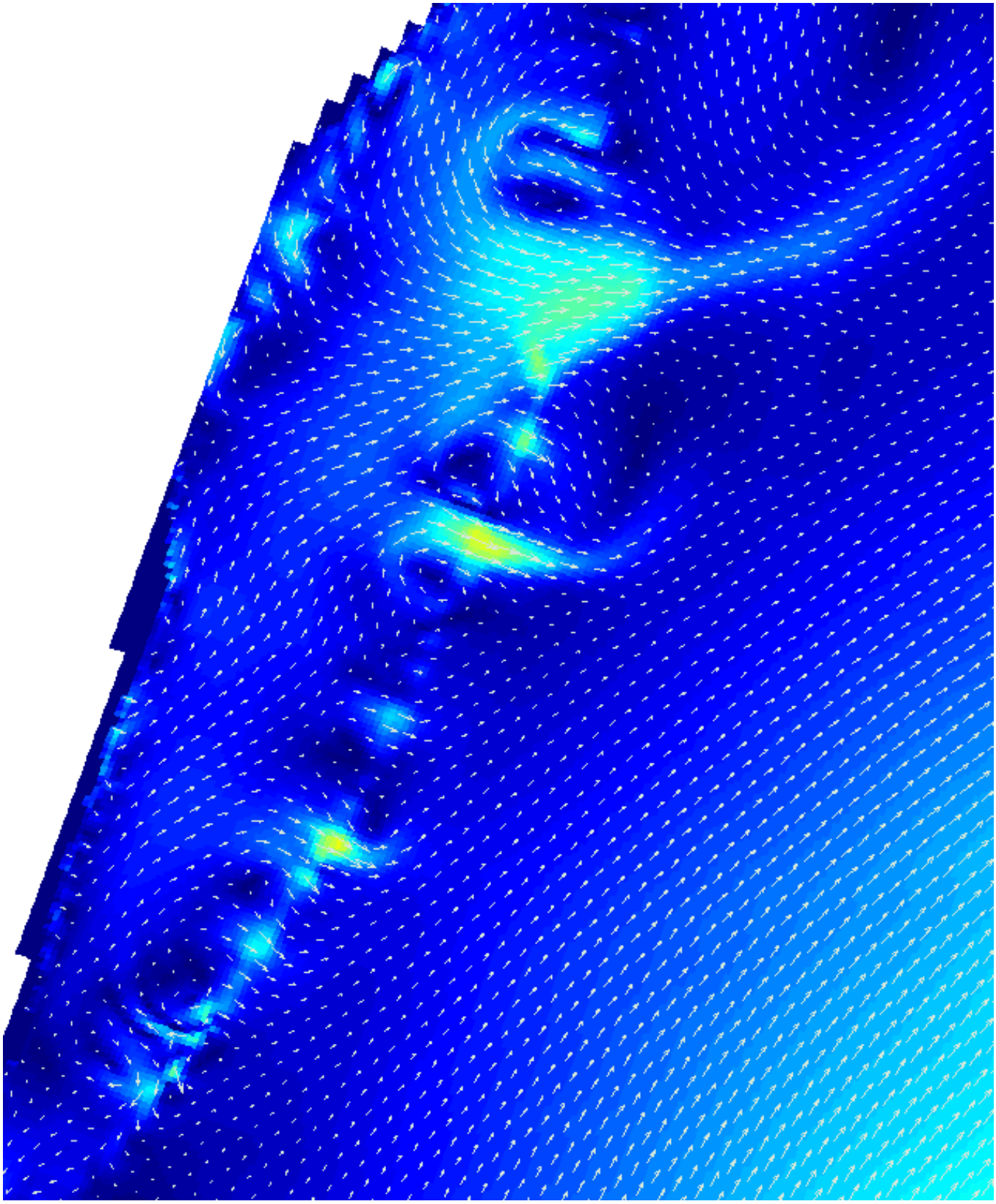

Figure C.2: Zoomed in flow on TOI of condition 1.

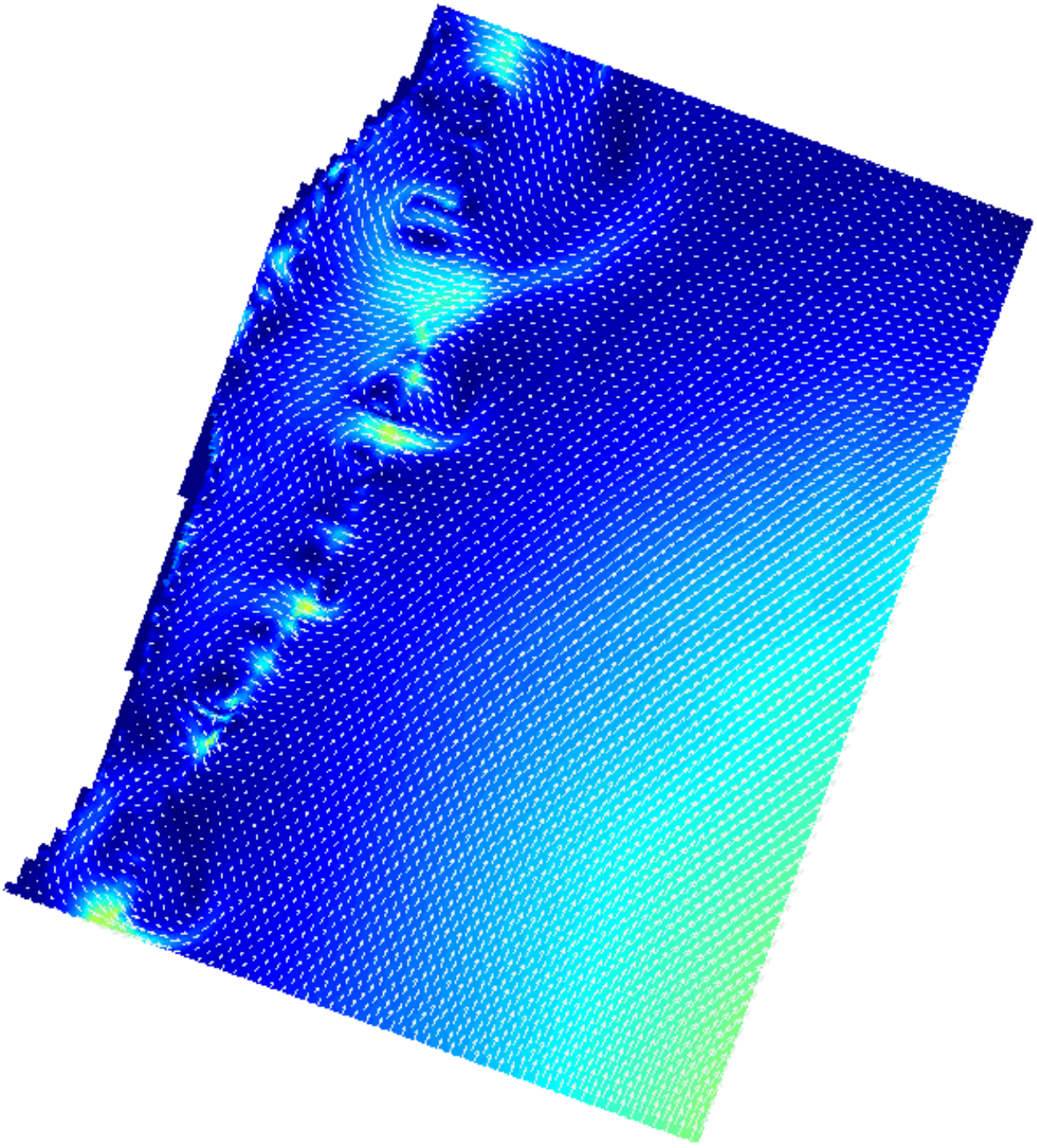

Figure C.3: Flow on TOI of condition 2.

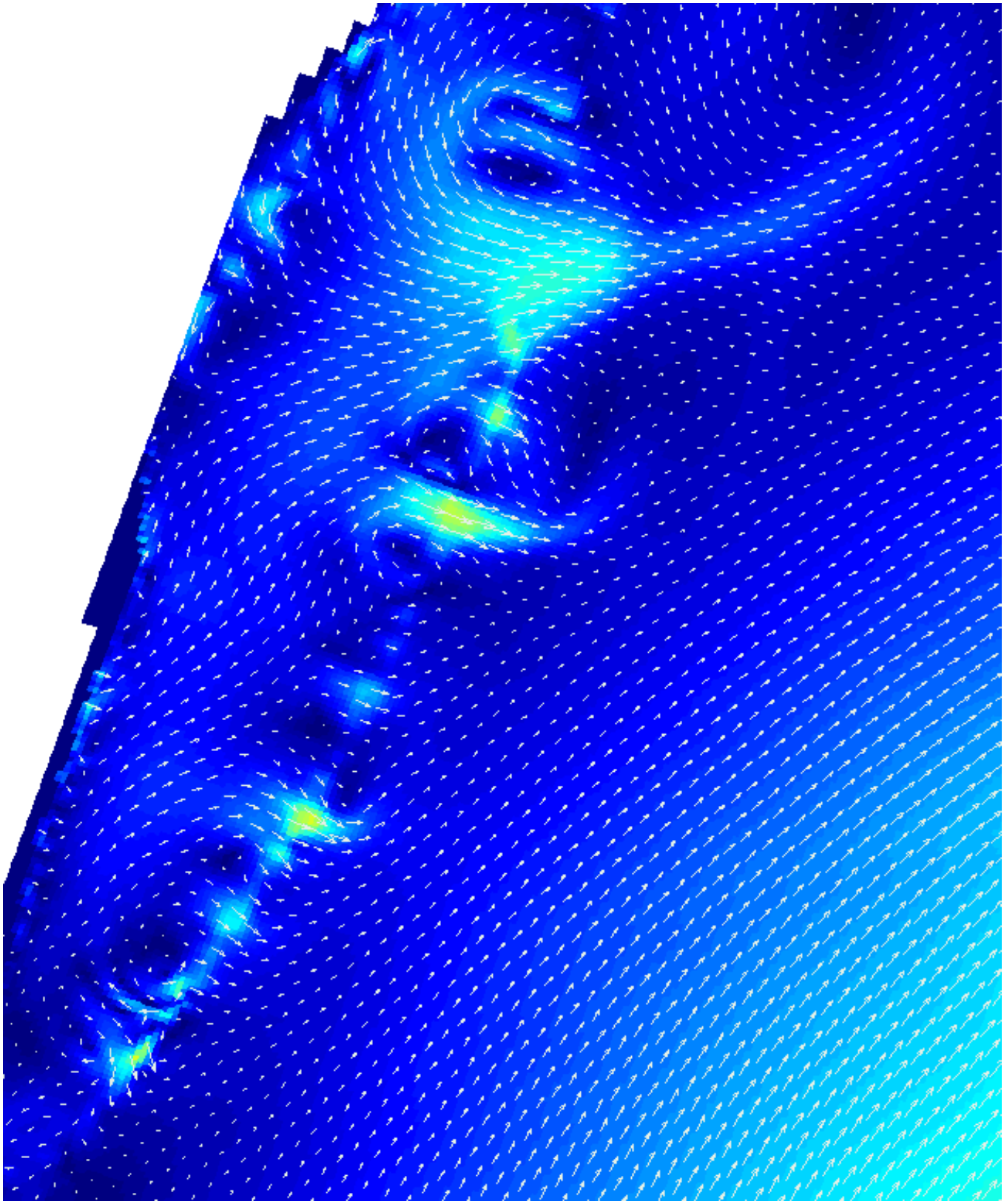

Figure C.4: Zoomed in flow on TOI of condition 2.

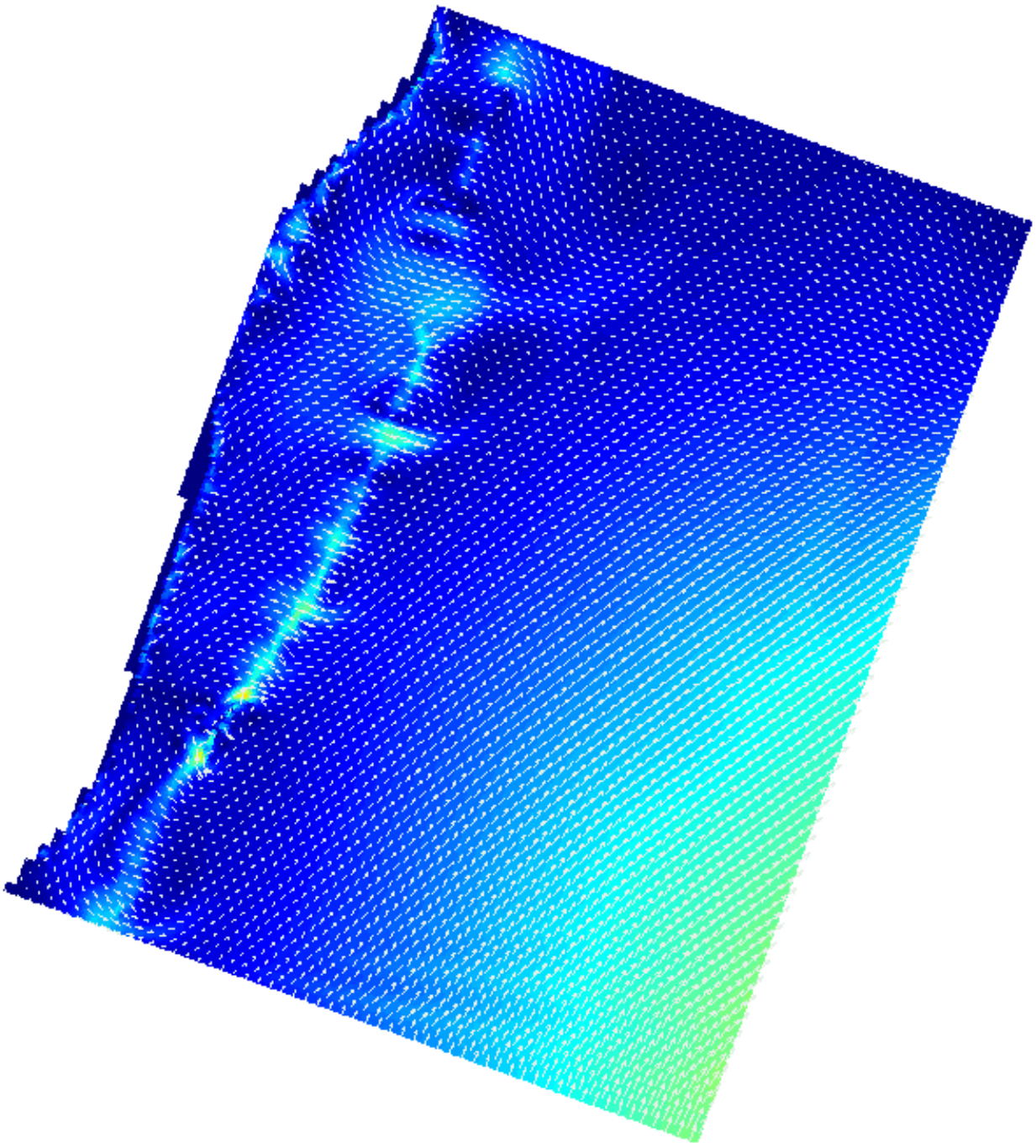

Figure C.5: Flow on TOI of condition 3.

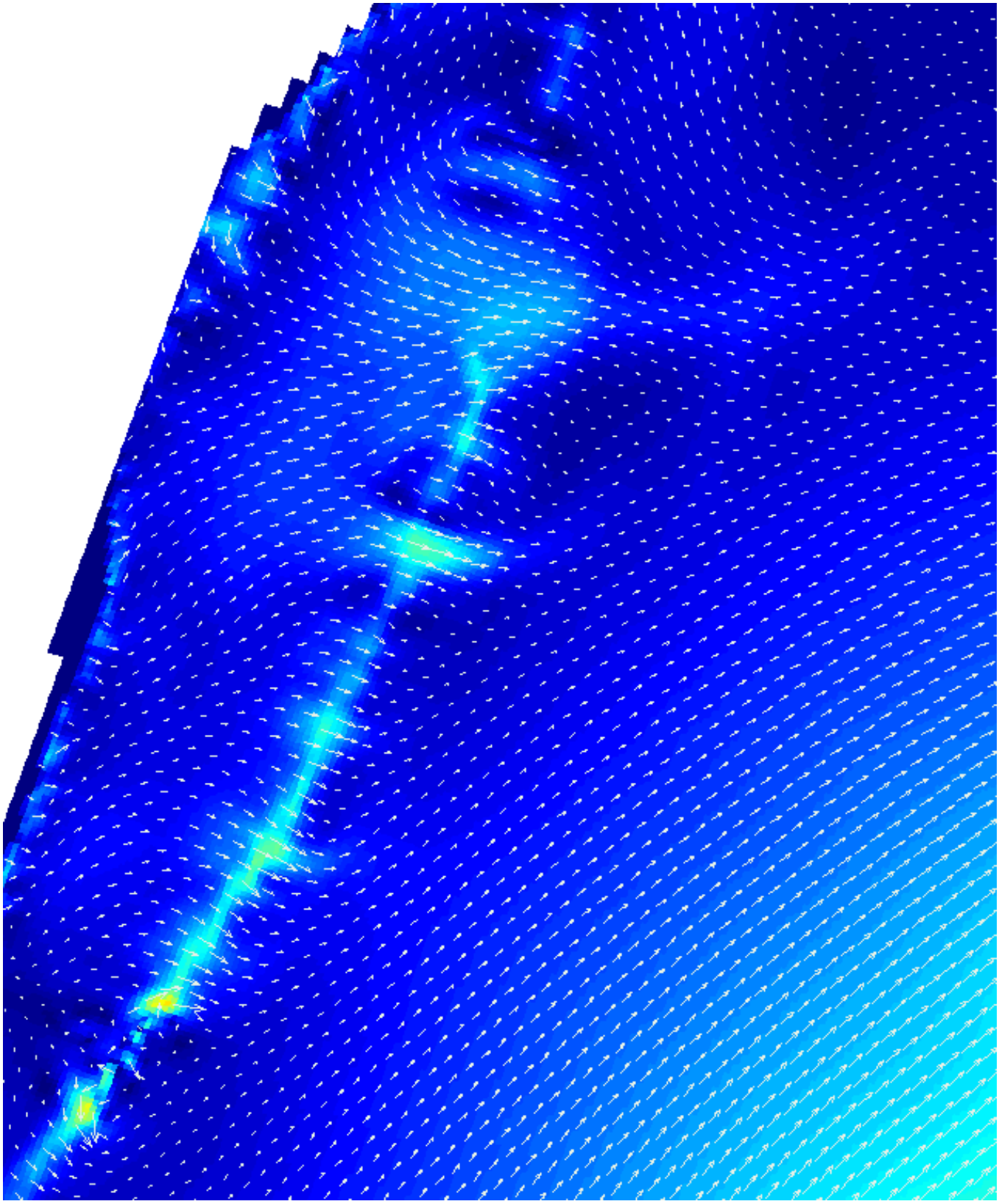

Figure C.6: Zoomed in flow on TOI of condition 3.

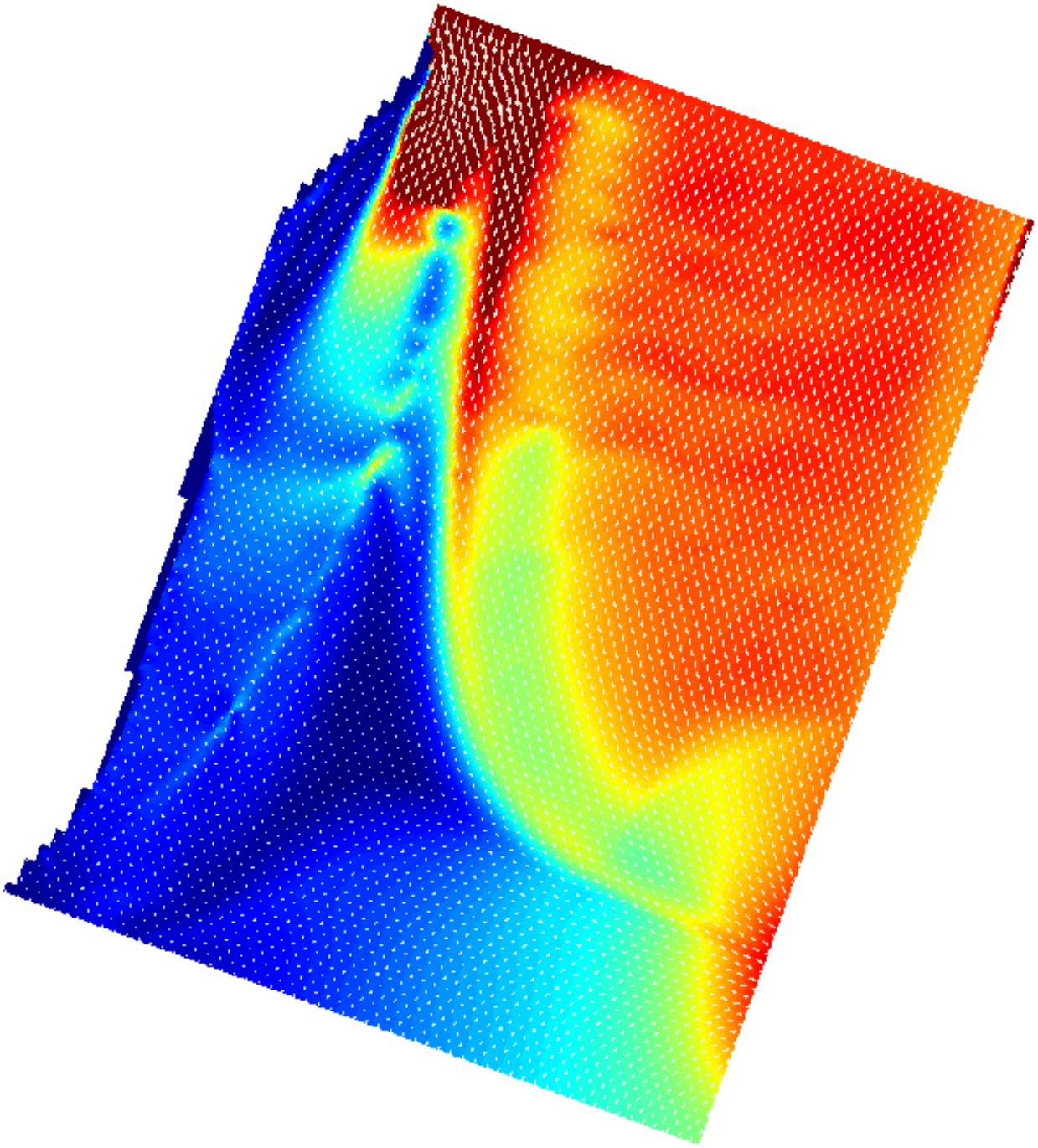

Figure C.7: Flow on TOI of condition 4.

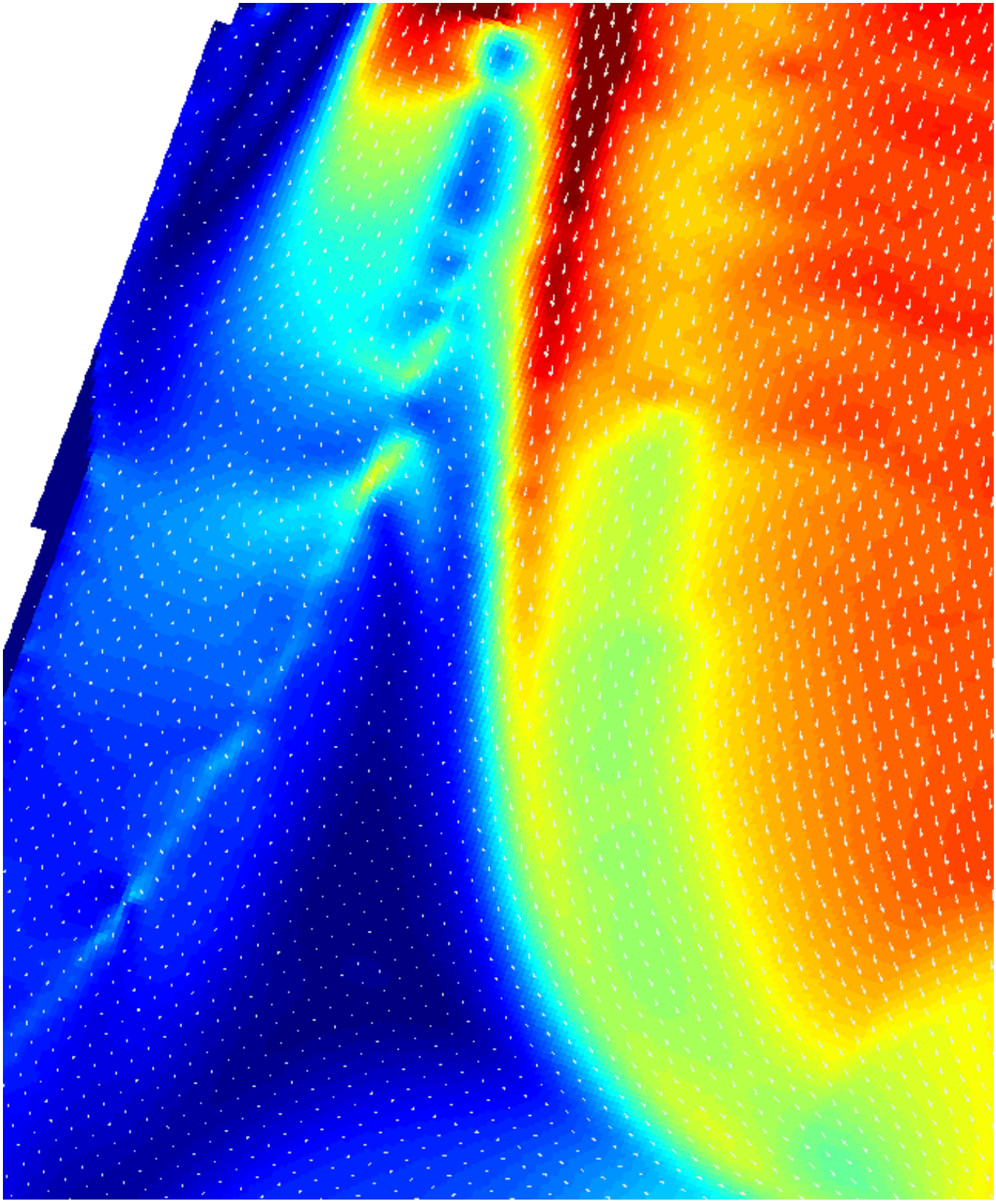

Figure C.8: Zoomed in flow on TOI of condition 4.

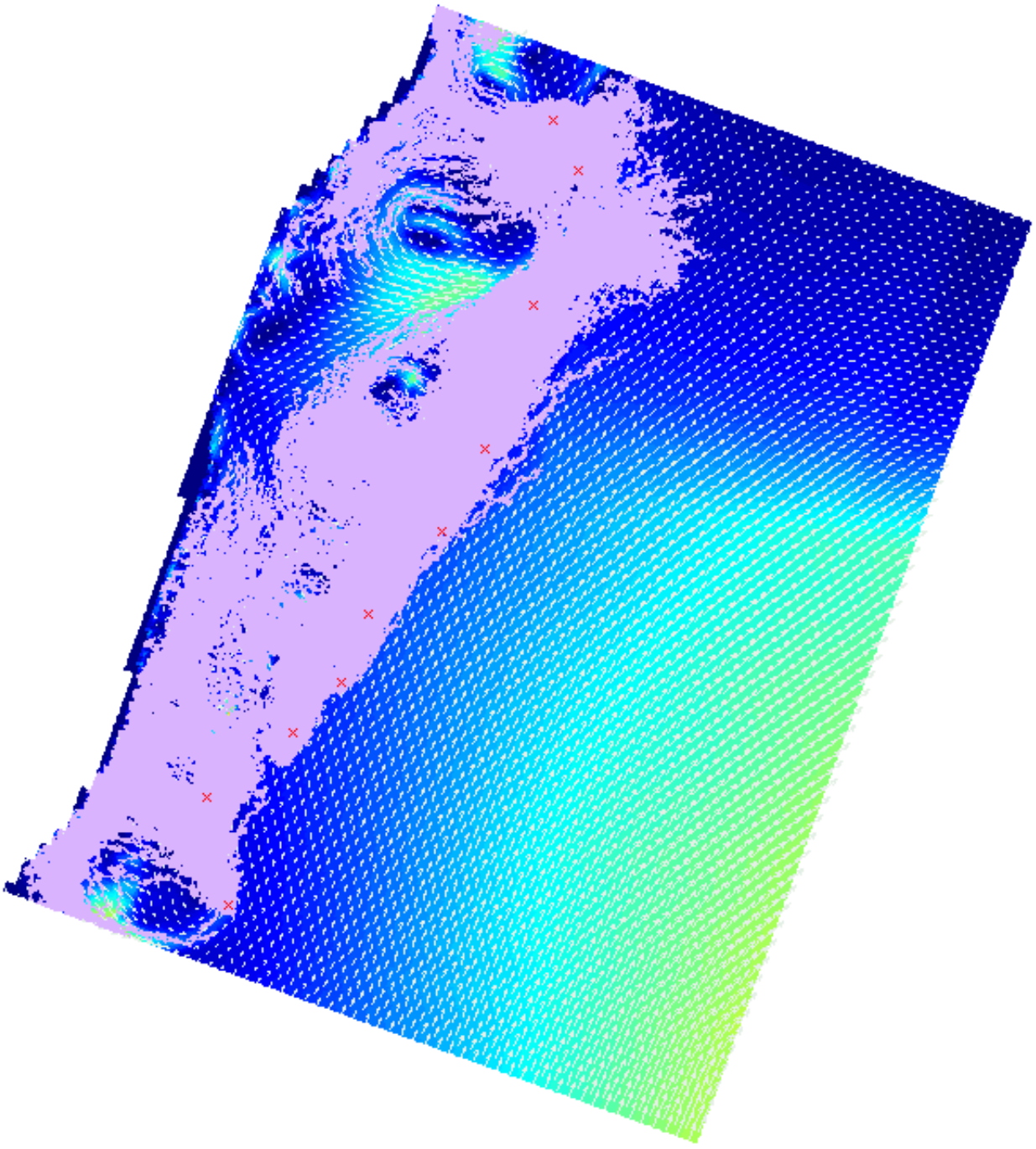

Figure C.9: 6hr particle tracking for condition 1 with 3 layers, red markers indicate release points.

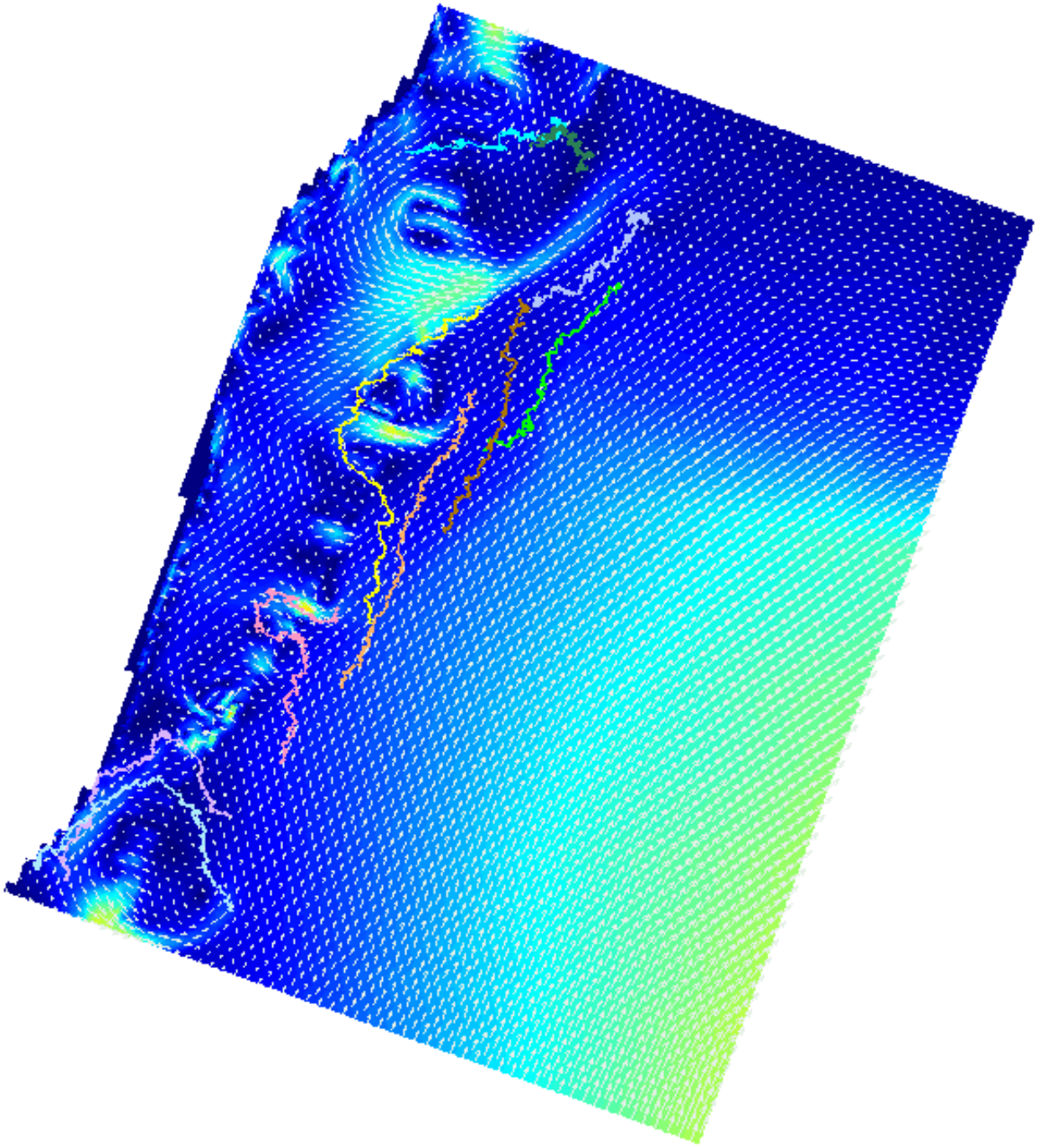

Figure C.10: 6hr single particles for condition 1 with 3 layers.

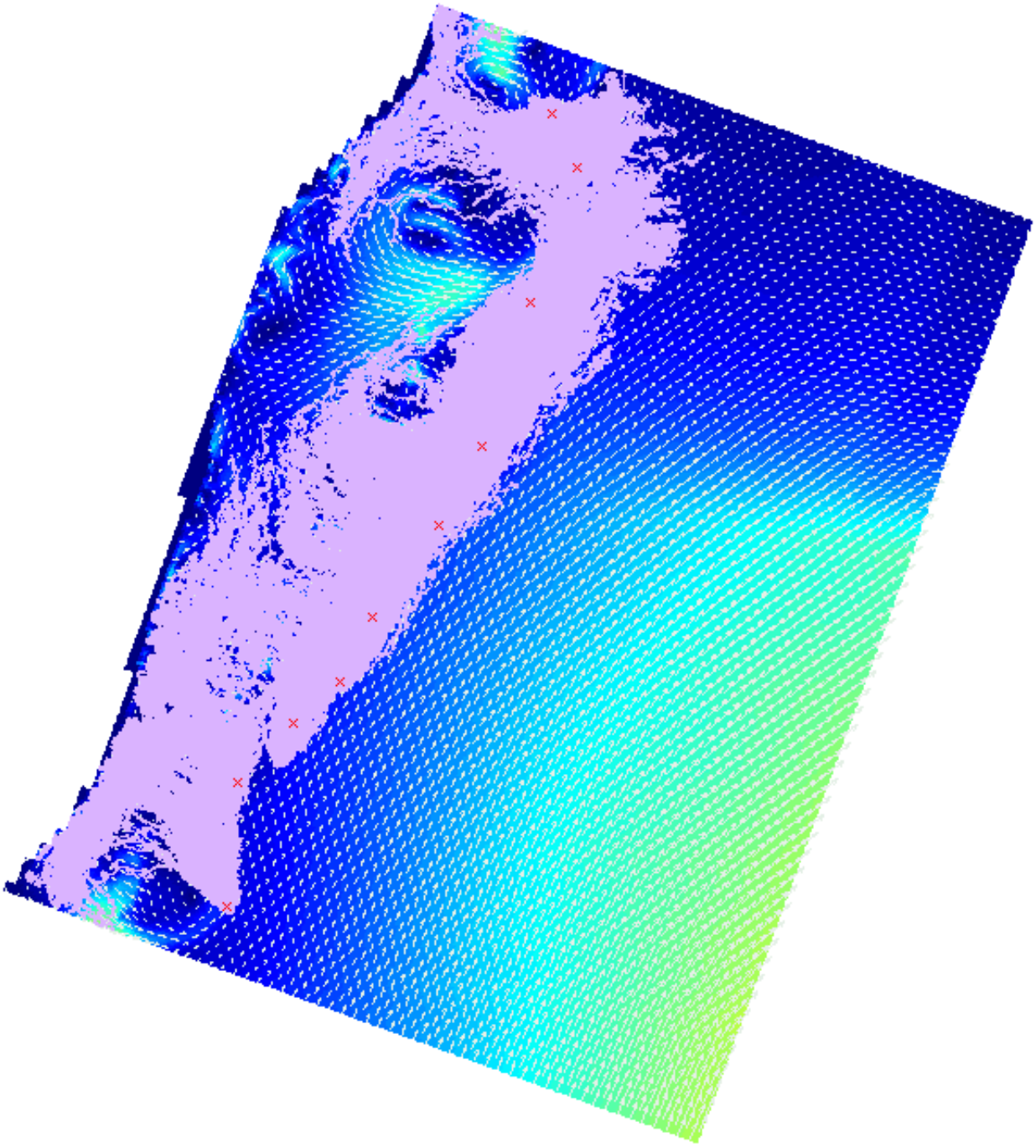

Figure C.11: 6hr particle tracking for condition 2 with 3 layers, red markers indicate release points.

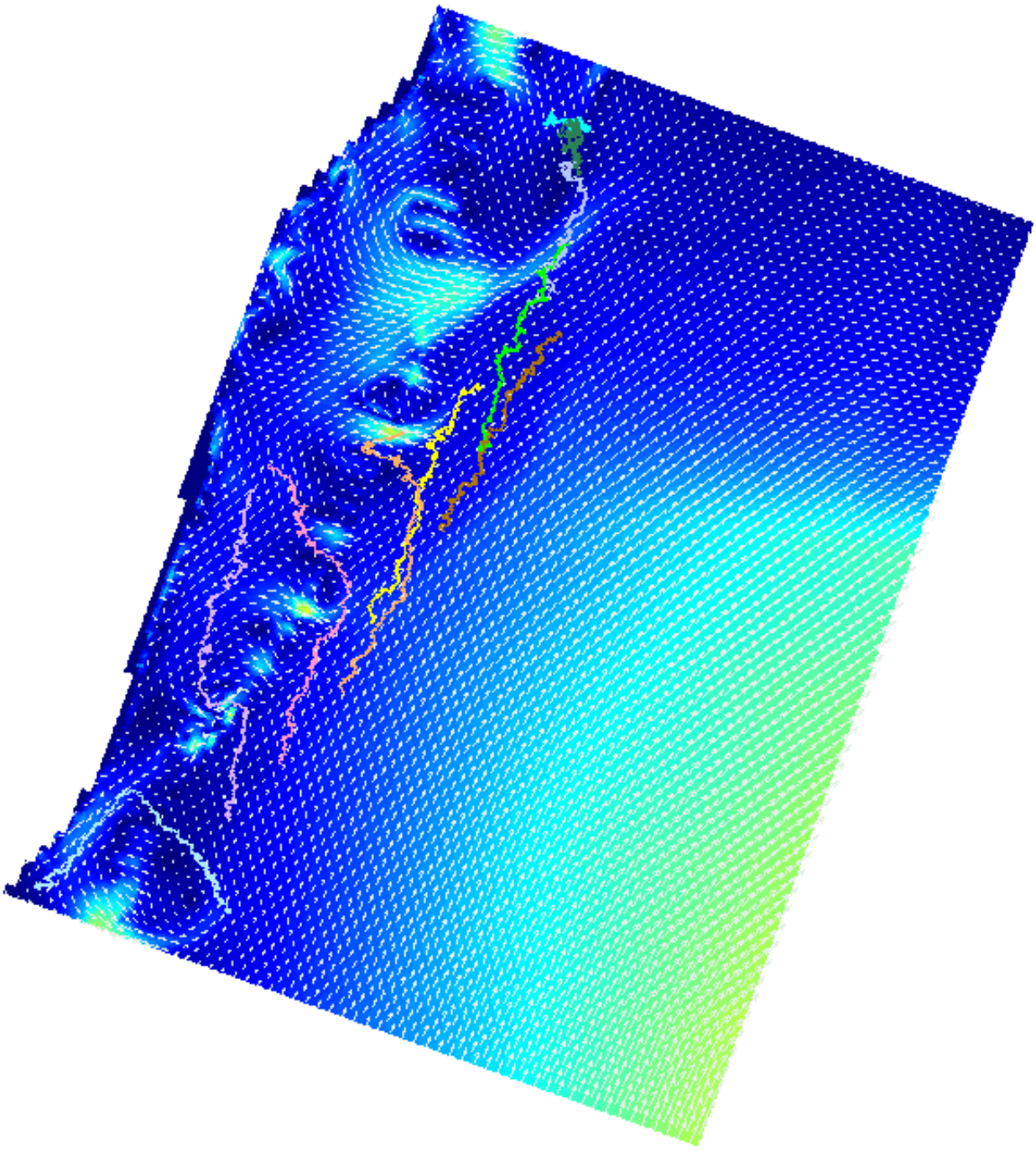

Figure C.12: 6hr single particles for condition 2 with 3 layers

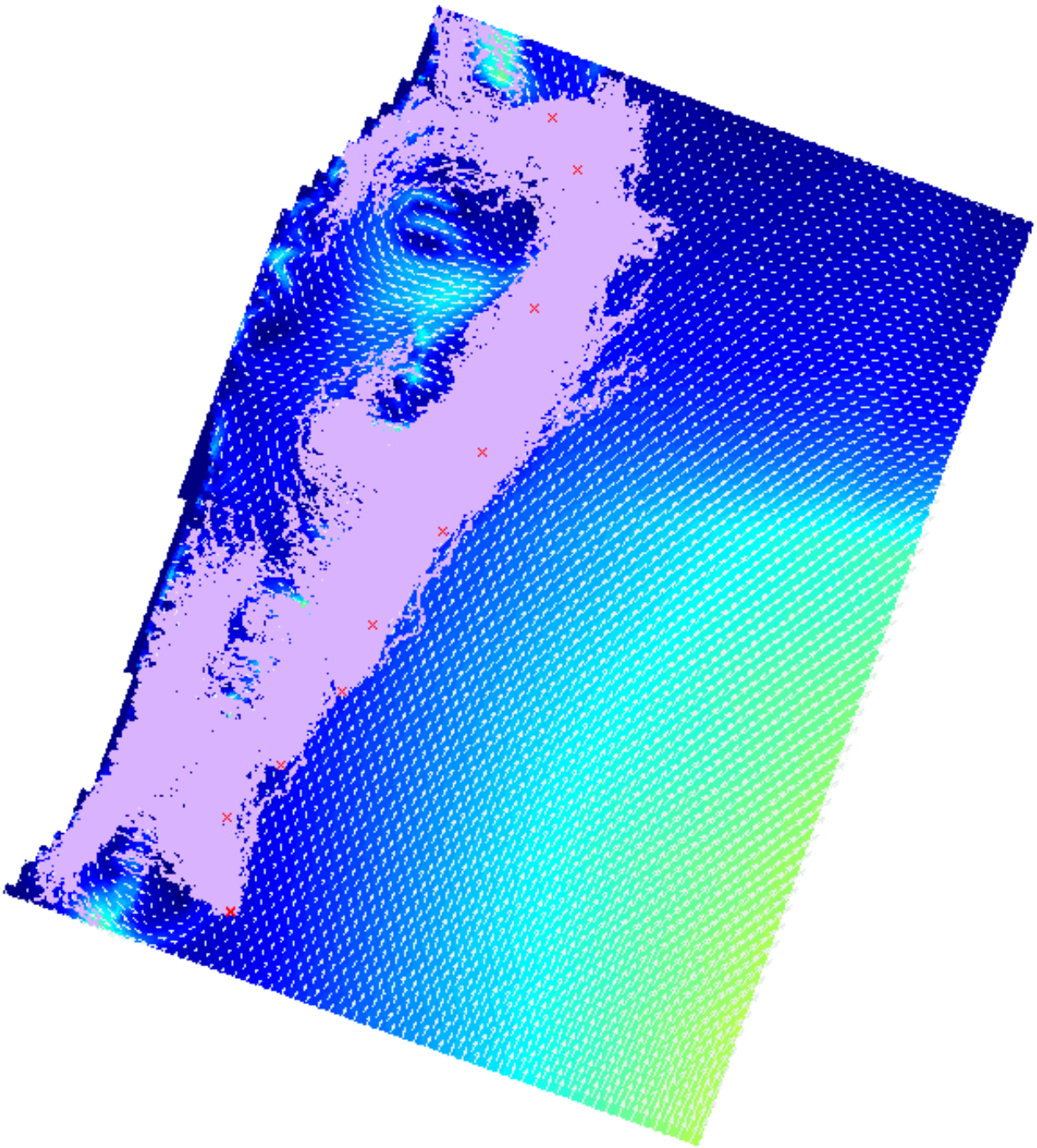

Figure C.13: 6hr particle tracking for condition 3 with 3 layers, red markers indicate release points.

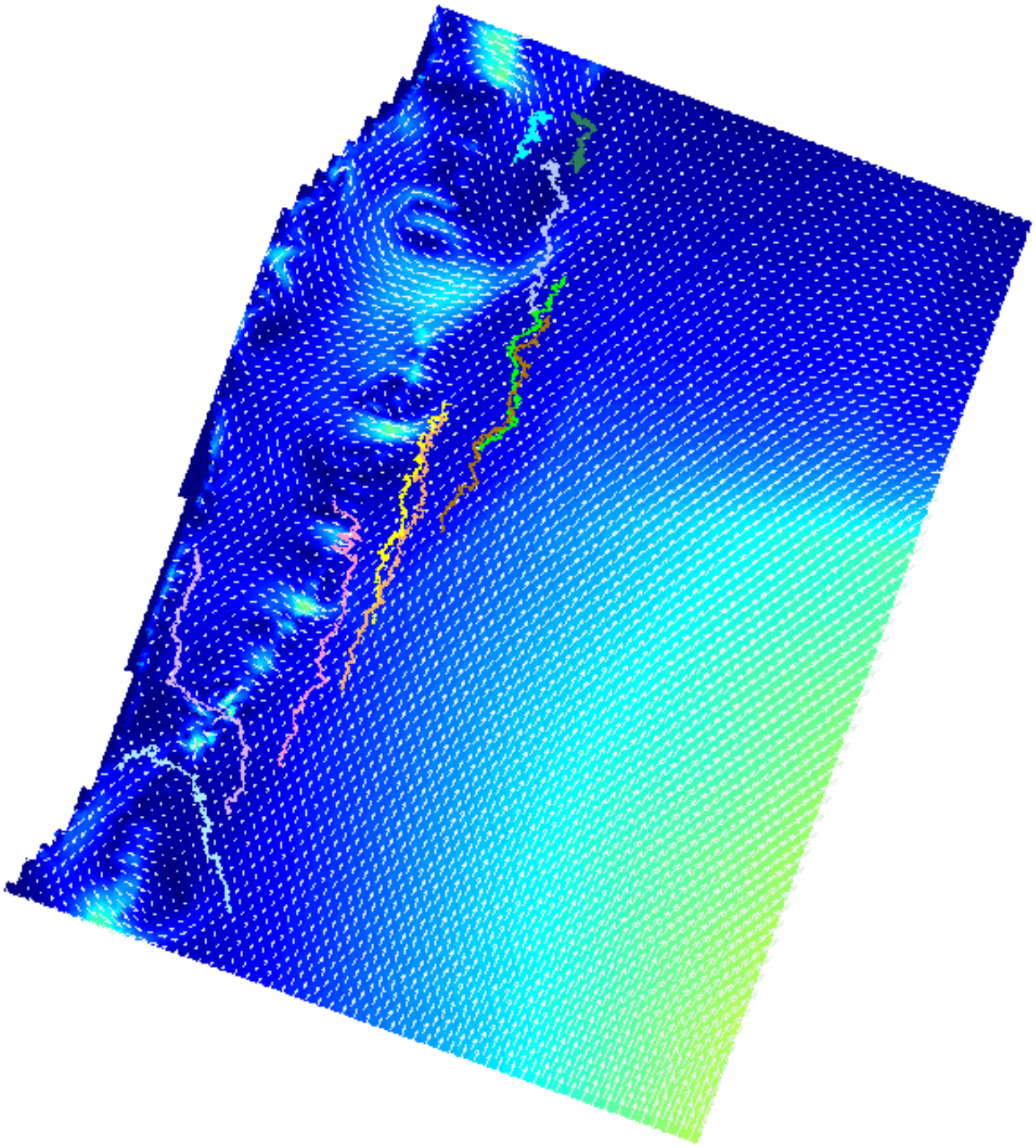

Figure C.14: 6hr single particles for condition 3 with 3 layers.

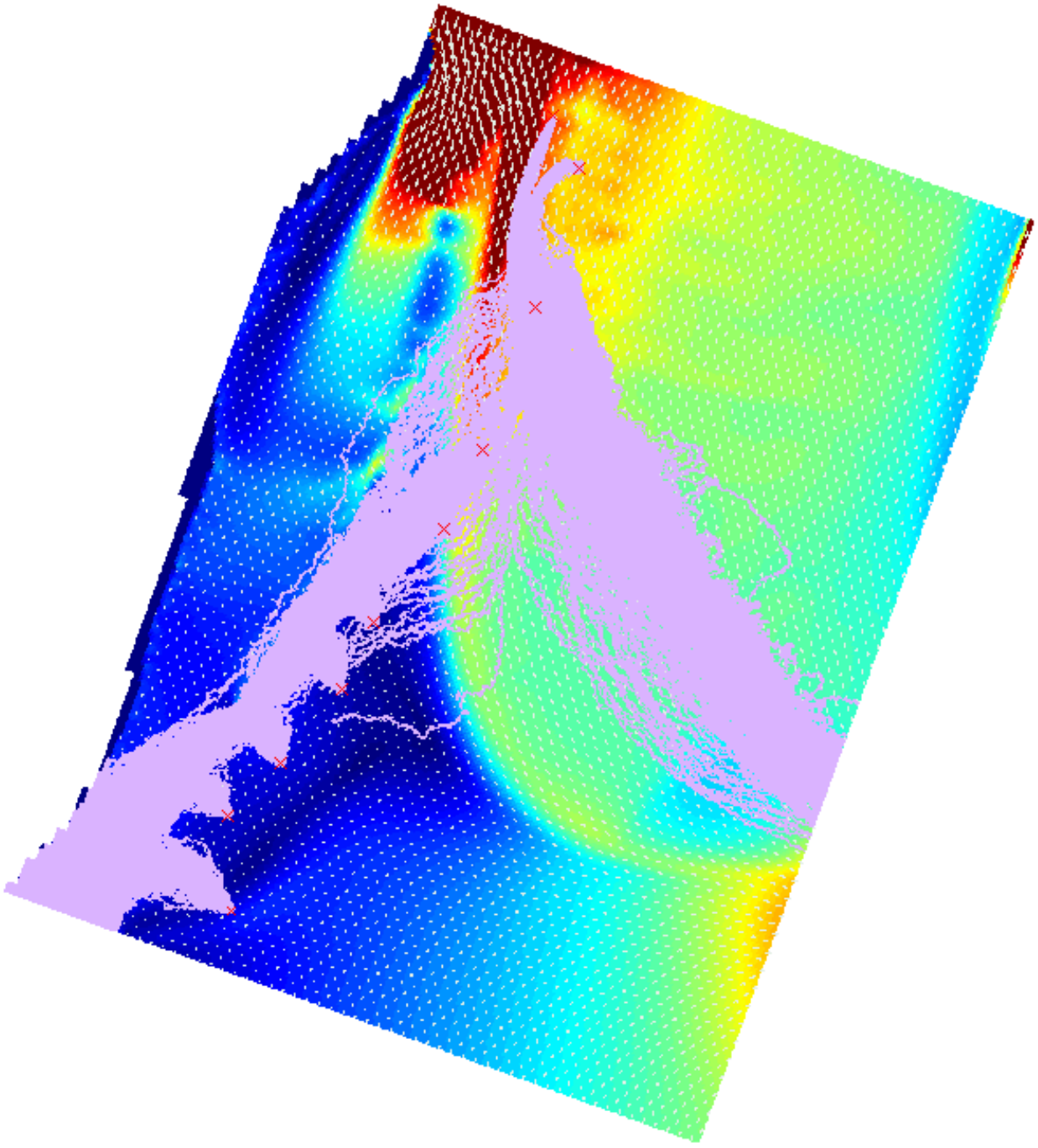

Figure C.15: 8hr particle tracking for condition 4, red markers indicate release points.

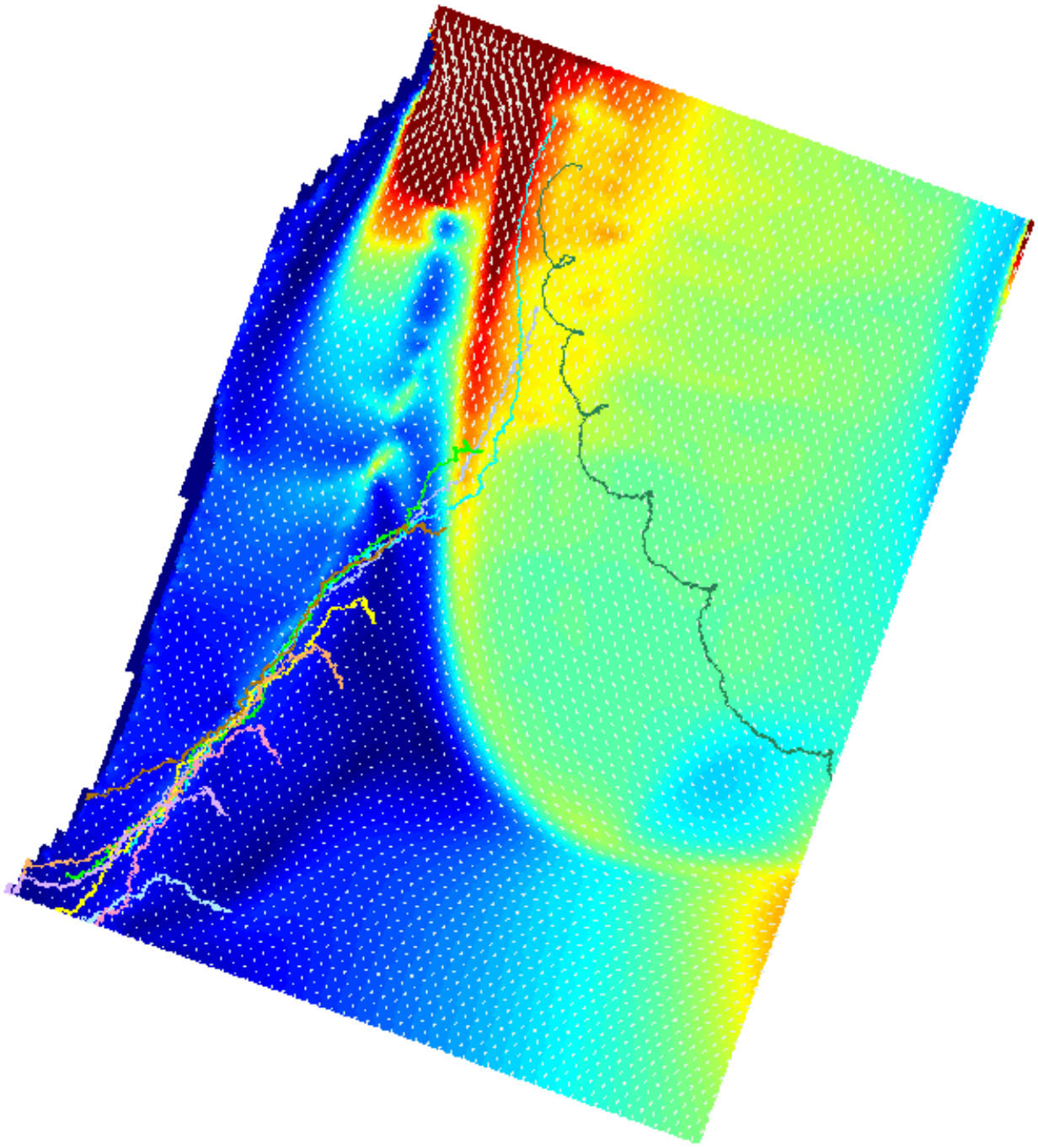

Figure C.16: 8hr particle tracking for condition 4.

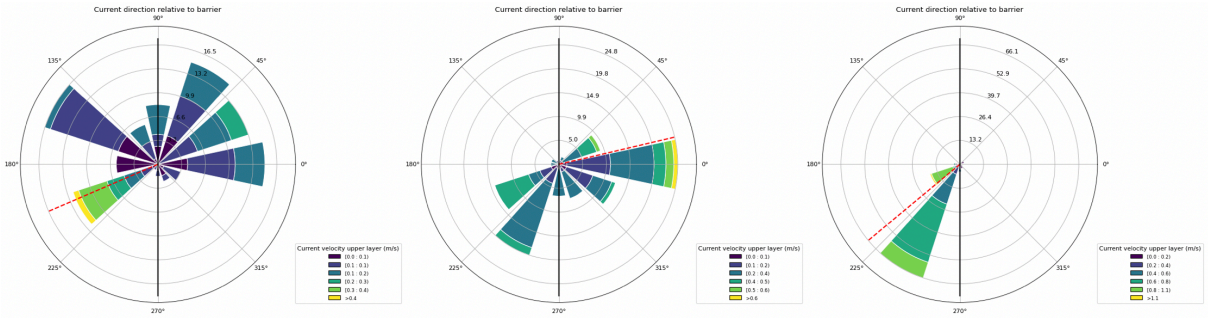

Figure C.17: Currents of the upper layer and directions relative to the barrier (black line) at locations (46,110), (57,259) and (58,289) respectively. The red line shows the direction of the incoming highest current magnitude.

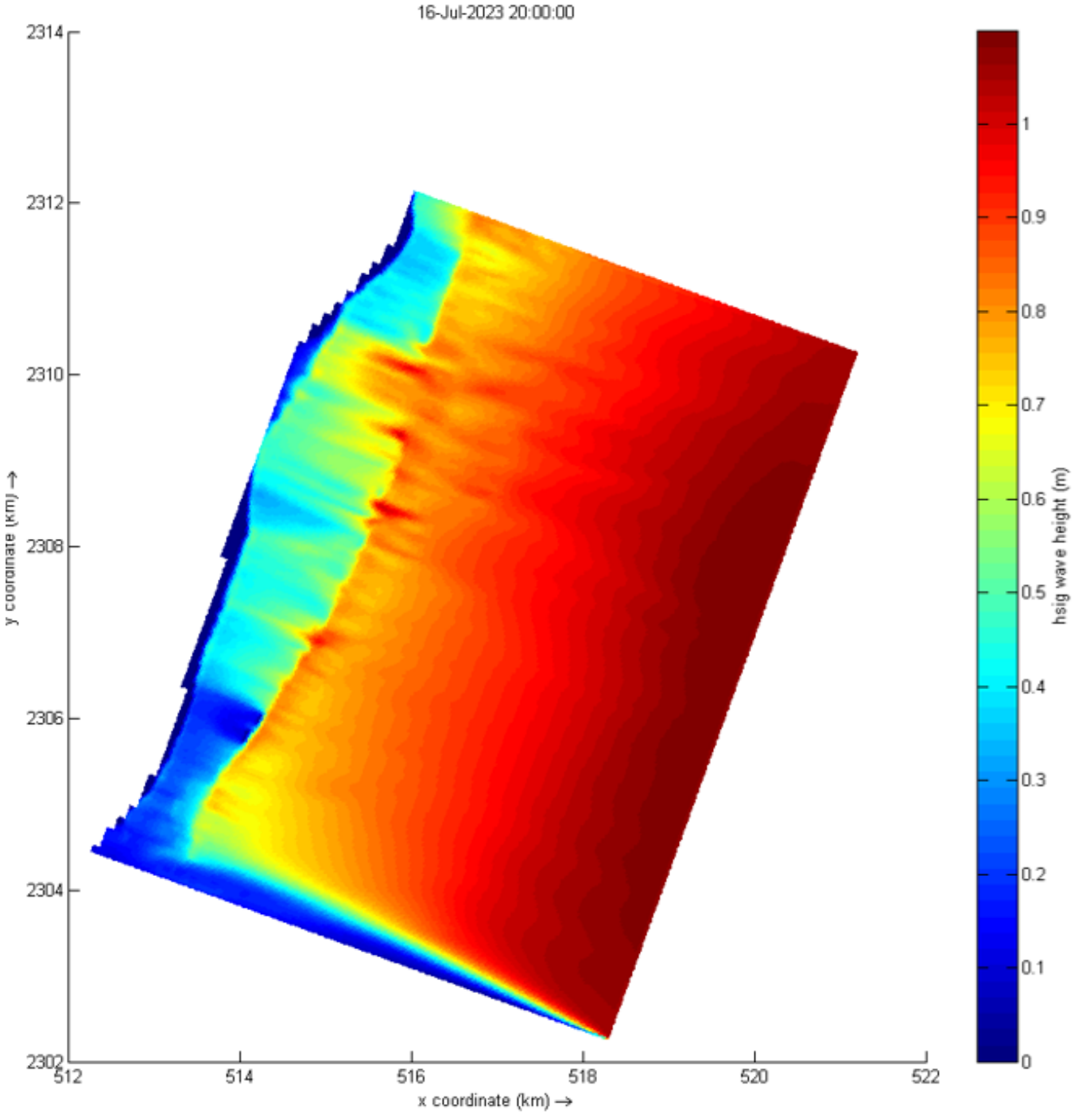

Figure C.18: Significant wave height condition 1.

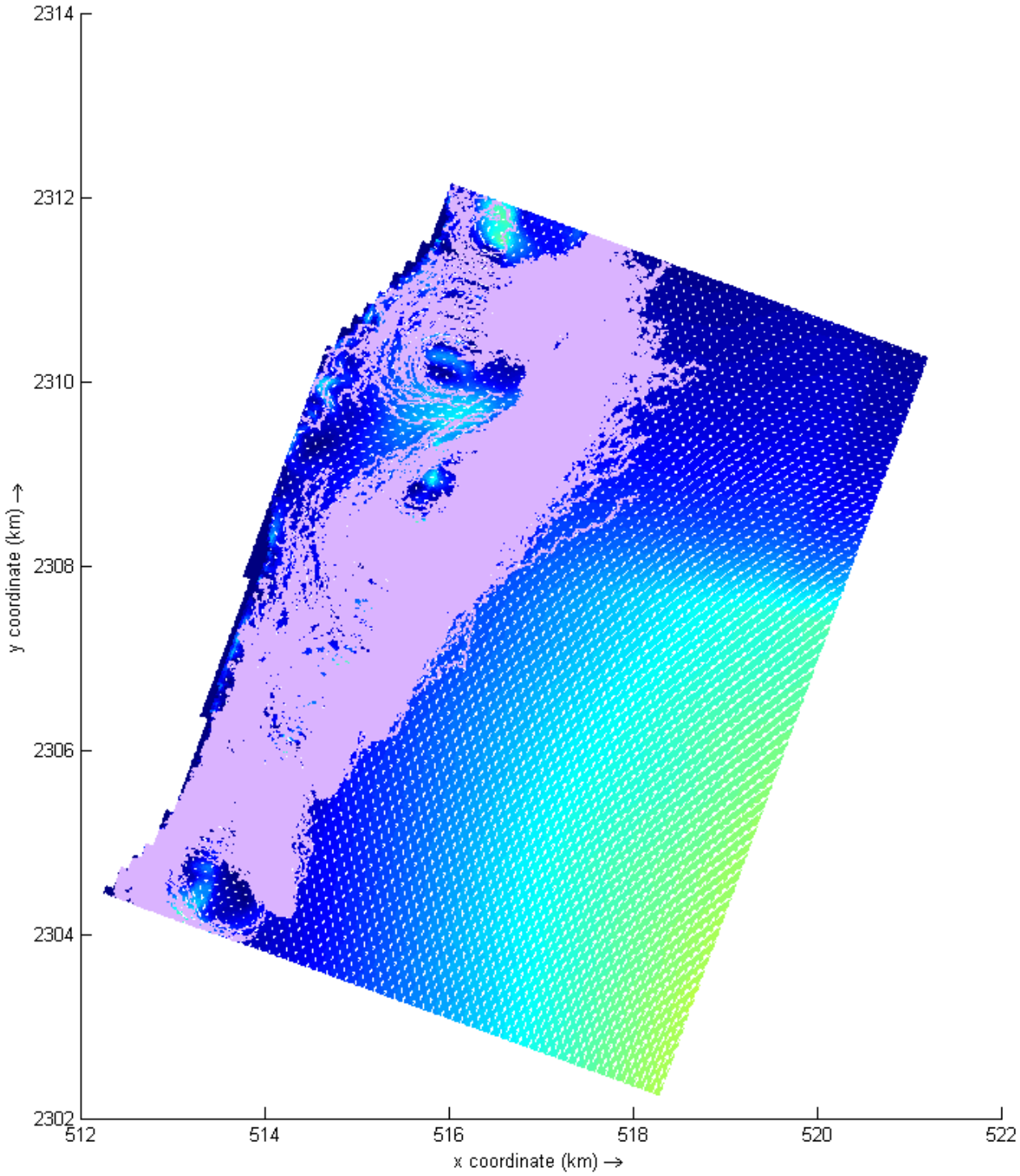

Figure C.19: Sargassum tracking all particles condition 3, with 10 release locations of 100 particles.

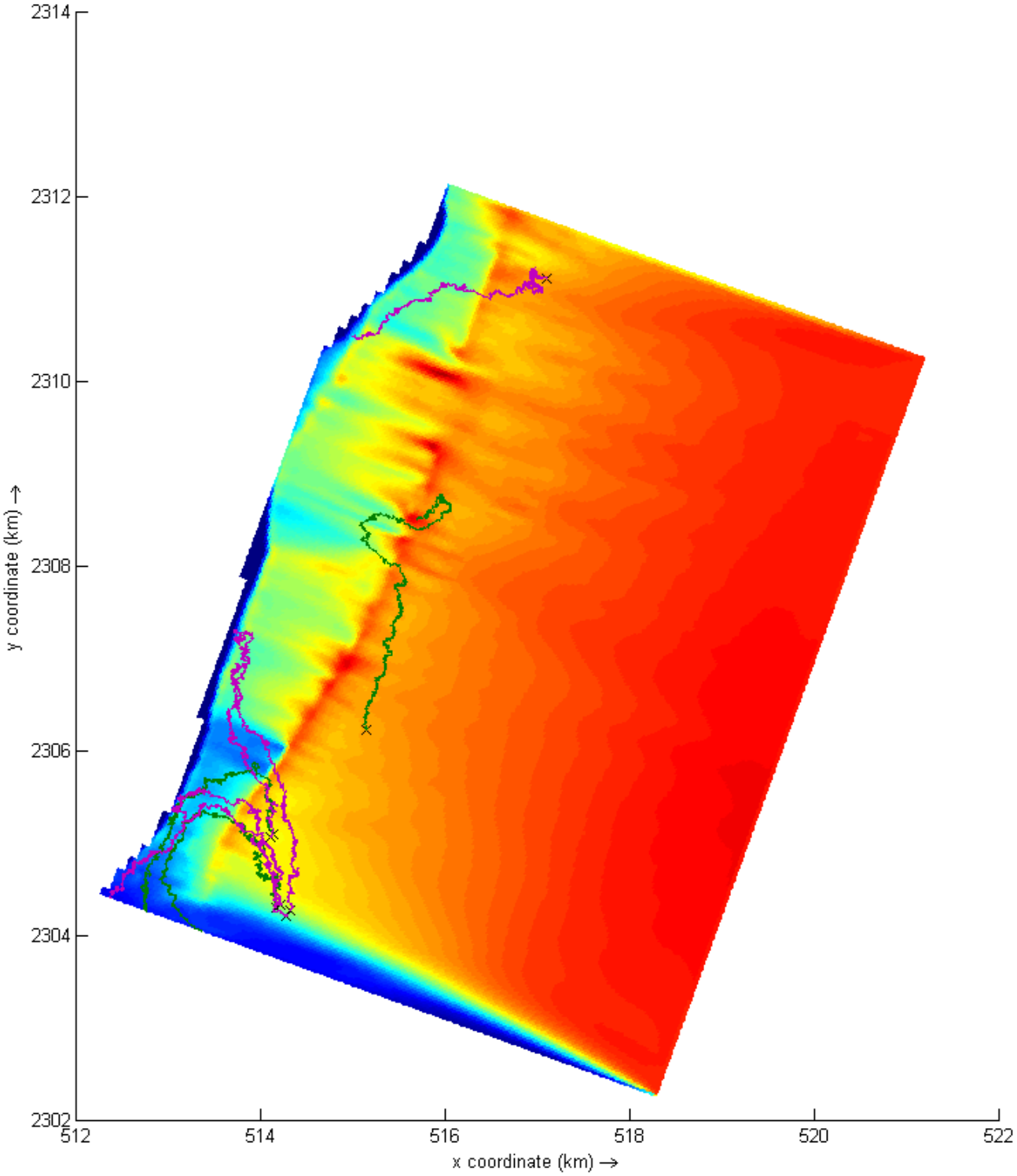

Figure C.20: Example particle tracking condition 3, indication flushing particles (green) and non-flushing particles (red).

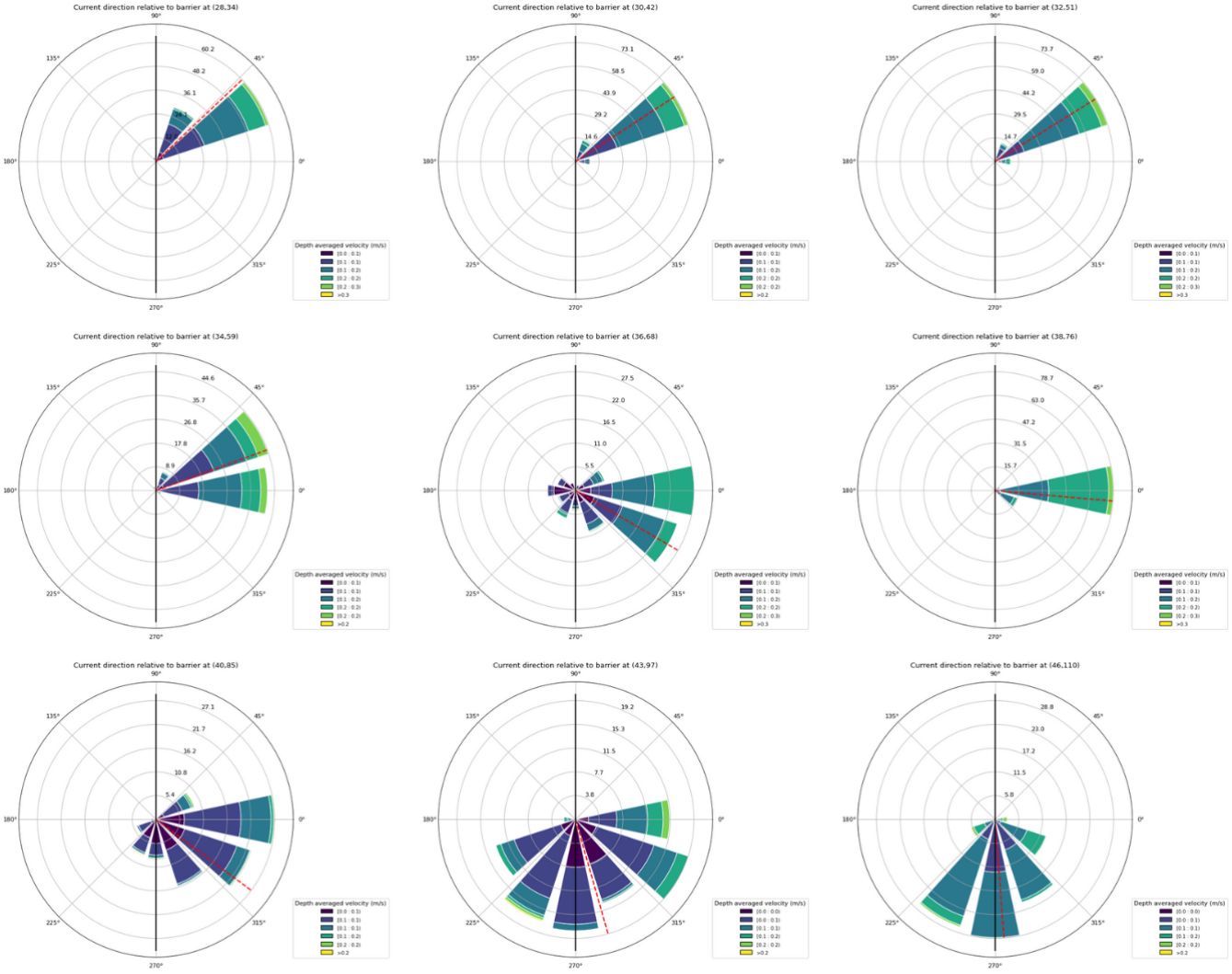

Figure C.21: Depth-averaged velocities and directions relative to the barrier (black line) at 9 different observation points along barrier 1. The red line shows the average direction of the current.

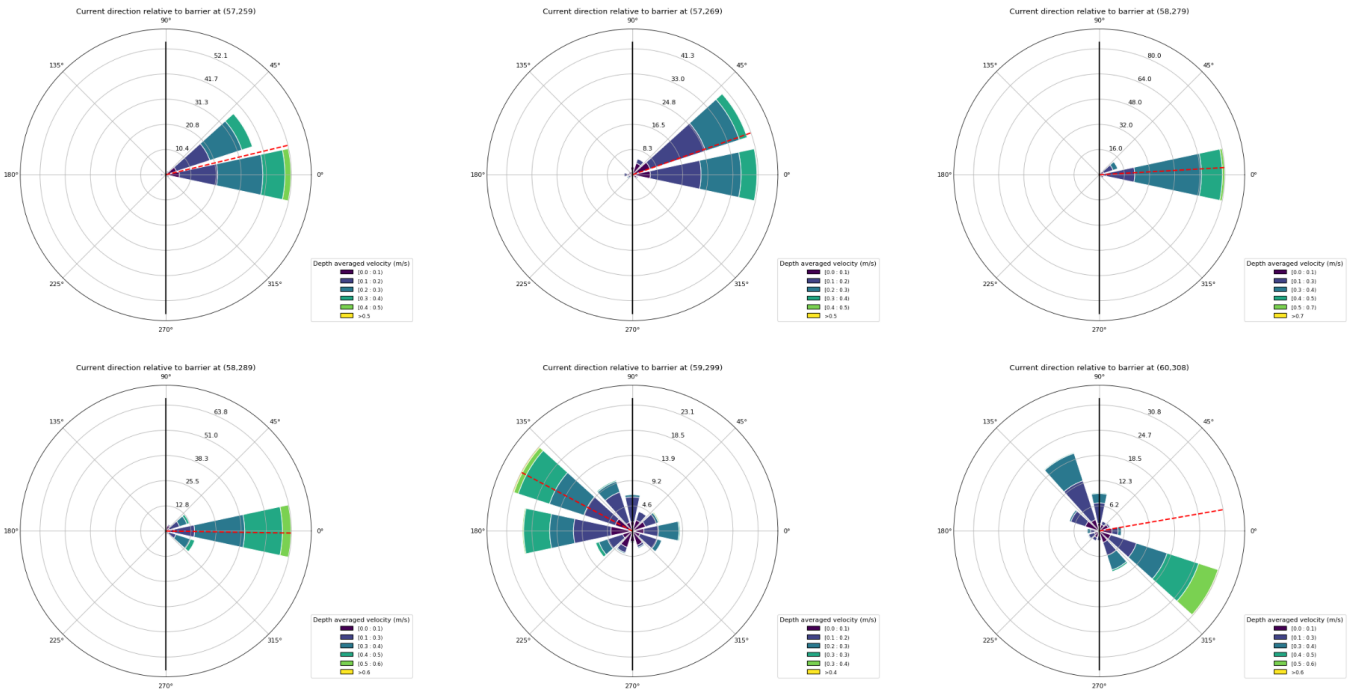

Figure C.22: Depth-averaged velocities and directions relative to the barrier (black line) at 6 different observation points along barrier 2 during the first test. The red line shows the average direction of the current.

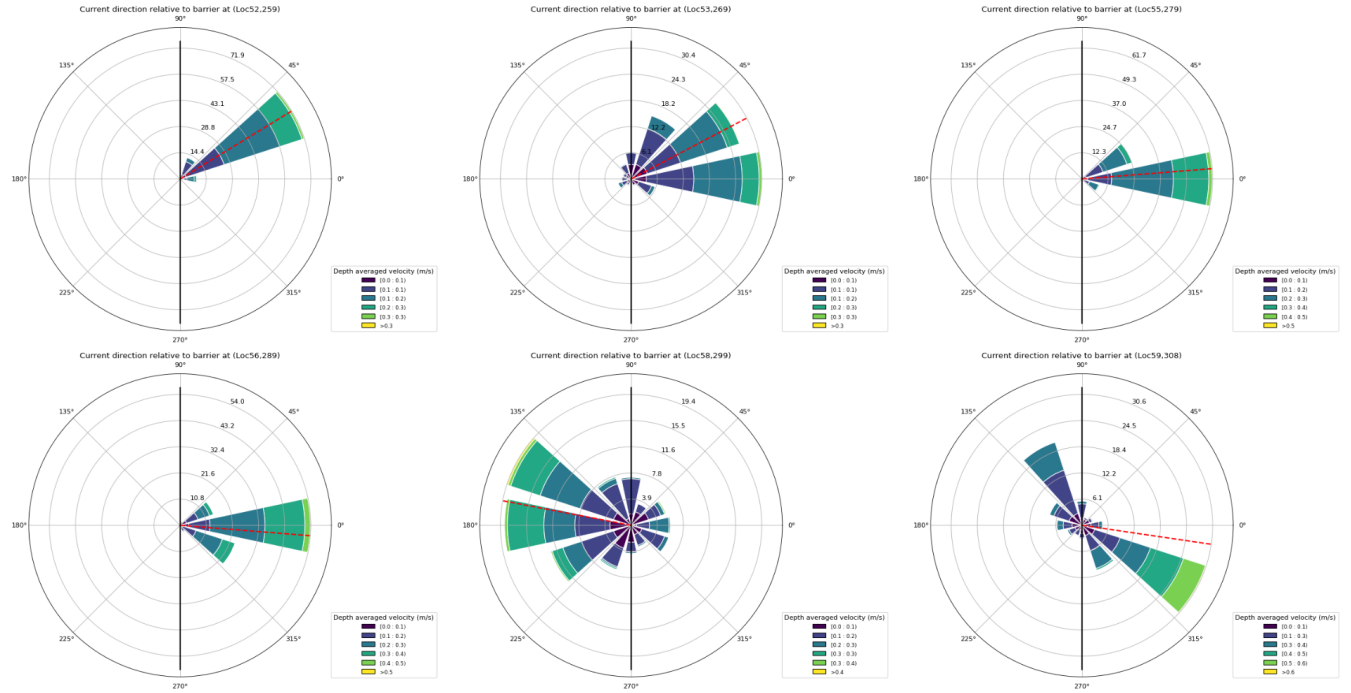

Figure C.23: Depth-averaged velocities and directions relative to the barrier (black line) at 6 different observation points along barrier 2 during the second test. The red line shows the average direction of the current.

D
Delft3D floating barrier methodology

For the implementation of a floating barrier, three different methods are used. In this section the three methods are discussed. Figure D.1, Figure D.2 and Figure D.3, illustrate how the structures are implemented within the grid [20].

In Figure 3.7 I, an example is shown of the interaction between modelled sargassum and a floating structure. In this test the barrier is modelled with a width of (1 grid cell) 25 meters and a draft of 2 meters. The floating structure is modelled as a locally applied surface pressure. The friction exerted by the structure on the flow is not taken into account.

In Figure 3.7 II, a rigid sheet is used with a vertical plate positioned over 3 grid cells in M-direction and 20 in N-direction. The flow blocked by rigid sheets is directed both in the u- and v-directions (x, y). A rigid sheet is a plate that extends into the flow over k-layers along the grid lines. In Figure 3.7 the first two layers are blocked. The difference between this method and the 3D-gate is the addition of linear friction exerted by the plate on the flow. For this case a maximum value of 1000 for friction is chosen. However, this method does not accurately reflect the behaviour of sargassum as it passes through the sheet within the model.
In Figure 3.7 III a 3D-gate is implemented with a vertical plate positioned over 3 grid cells in M-direction and 20 in N-direction as well. There is no momentum exchange across the gate and friction exerted on the flow is not taken into account. The direction in which the flow is blocked is both in u- and v-directions (x, y). Defining the 3D-gate with 3 grid cells thickness is done to demonstrate that under no flow conditions in layer 1 and 2, sargassum still transports itself through the barrier.

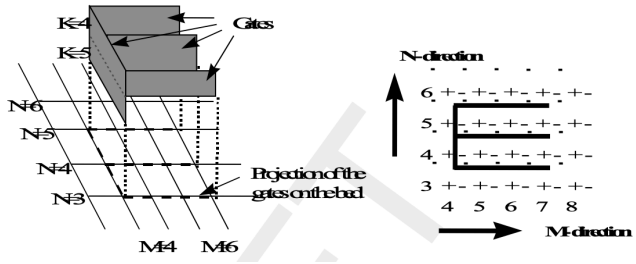

Figure D.1: Example of 3D gates in perspective view (left) and top view (right).

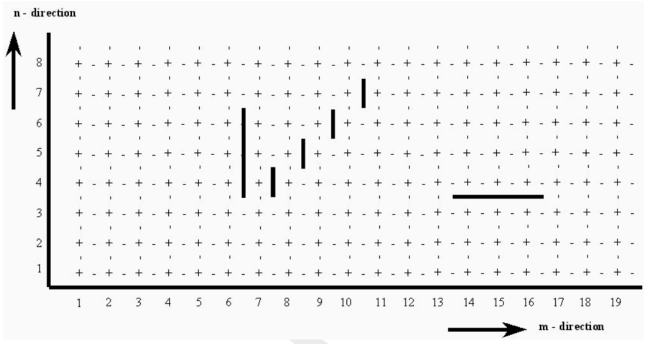

Figure D.2: Example of rigid sheet in perspective of top view.

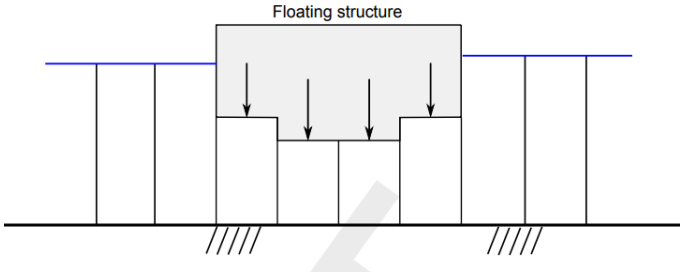

Figure D.3: Example of cross-sectional view of a floating structure.

E
Barrier design and materials

Table E.1: Detailed comparison of barrier types.

	Type I[4][23][33]	**Type II**[63][23][48]	**Type III**[23]	**Type IV**[27]
Application	Protected waters	Protected waters	Calm waters	Protected waters
Unit length (m)	-	-	3.0-6.0	8.0
Section length (m)	30	25-50	-	-
Draft (m)	0.3-1.5	0.7-0.8	0.9	1.5
Freeboard (m)	0.1-0.5	0.3	0.4-0.6	0.4
Floating material	PVC coated closed cell foam logs	PE/HDPE with PU foam	Double walled foam filled HDPE	Inflatable air-filled PVC sacs
Skirt (y/n)	Yes	Yes	Yes	No
Skirt material	Woven PVC Permeable Fabric	PVC coated PE	Woven PVC Permeable Fabric	Kevlar nets
Tensile strength (kg)	2268-20412	4780-7017	27216	-
Ballast	0.6-1.6 cm cable/1.2 cm galvanised steel chain	1.2 cm galvanised steel chain	1.2 cm galvanised steel chain	-
Connectors	Stainless steel shackles	Dynamic Response Connector	Shackles with 4309 kg working load	PVC covered PP ropes
Anchor intervals (m)	7.5	8.0	3.0-6.0	2.0
Anchor points	Reinforced metal plates	Reinforced metal plates	Reinforced metal rings	PVC covered PP ropes
Flexibility (p/s/g)	Sufficient	Good	Poor	Poor
Maintenance (p/s/g)	Good	Sufficient	Sufficient	Good
Shipping Volume $(\mathrm{m}^3/\mathrm{m})$	0.16	0.1	0.45	0.01

E.1. Human Complications

E.1.1. Barrier design

Human factors significantly impact the longevity and performance of sargassum barriers. Negligence in maintenance is the most common cause of failure, along with vandalism and accidents. Barriers must be removed before storms, as they cannot withstand hurricane-level forces. Failure to do so often leads to irreparable damage. Accidents involving vessels are another issue, as poorly visible barriers can be damaged when ships pass over them.[10][51] Secure installations and trained personnel are vital to mitigate these human-related risks.

E.1.2. Anchoring stratagy

In areas prone to theft or vandalism, concrete block anchors are preferred over Danforth-style fluke anchors which can be more easily removed or stolen. Secondly, vessel activity poses a threat to the anchoring of the barriers. Anchors from boats and fishing nets can damage the moorings. These human-related factors underscore the need for secure installations and well-trained personnel to manage the deployment and maintenance of the barriers.[10]

E.2. Mooring Line Materials

Mooring lines are important for floating barriers, as they ensure the stability and positioning of the structure by distributing forces across the system. In modern maritime engineering, Polyethylene (PE), Polypropylene (PP), and Nylon mooring lines are widely applied. Their tensile strengths are compared in Figure E.1.

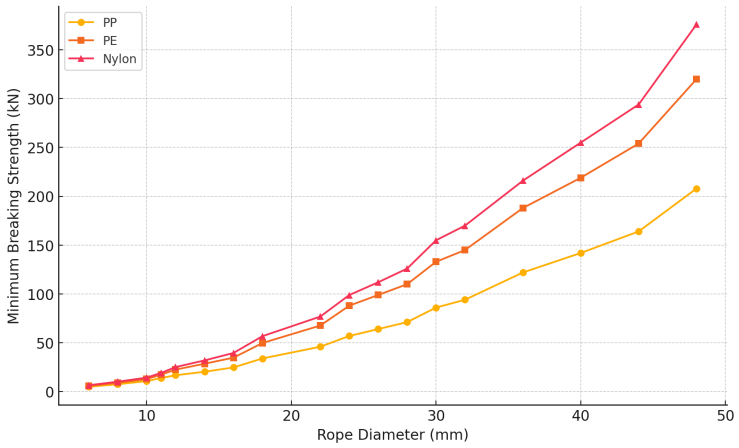

Figure E.1: Minimum breaking strength of PP, PE, and Nylon for marine ropes across varying diameters.[24]

Polyethylene

PE is known for its affordability. It provides moderate tensile strength and is more UV-resistant than PP and Nylon, making it a good option for long-term exposure in marine environments. PE floats on water, which can help avoid entanglement with underwater objects. However, its tensile strength is moderate compared to Nylon.

Polypropylene

PP ropes are lightweight and, like PE, their low density makes them float naturally, which is beneficial for floating barrier systems. Despite its affordability, PP has relatively low tensile strength compared to other materials, and it is more susceptible to UV degradation, requiring more frequent replacement in high-exposure environments.

Nylon

Nylon is regarded as one of the strongest and most durable materials for mooring lines. It offers excellent shock absorption due to its elasticity, which allows it to handle the dynamic forces caused by waves and currents. Additionally, Nylon has the highest tensile strength and resistance to abrasion and UV rays, making it the most suitable material for mooring lines in high-stress environments.

Overall, Nylon is the best material for mooring lines in floating barriers due to its superior tensile strength, durability, and elasticity. Unlike PE and PP, Nylon provides excellent shock absorption and withstands UV exposure, which is crucial for marine environments. While PE and PP are cost-effective and buoyant, their lower tensile strength and durability make them less suitable for long-term applications in dynamic marine conditions.

E.3. Polyethylene

PE is a widely used material with applications in various industries. As seen in the polymer structure in Figure E.2, the simple carbon-hydrogen of PE structure gives it flexibility, chemical resistance and excellent processability. This structural simplicity also contributes to its cost-effectiveness and wide availability, making it a popular choice for industrial applications.

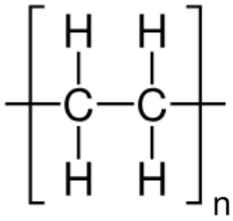

Figure E.2: Molecule structure of PE.

LDPE and HDPE

Since the 1950s, various production processes have been developed to meet the specific requirements of different applications. PE can be categorised into different grades based on its molecular structure, which influences its properties. The main categories include Low-Density Polyethylene (LDPE), Linear Low-Density Polyethylene (LLDPE), and HDPE. The key difference in quality arises from the degree of branching in the PE molecules, as shown in Figure E.3. The more branched the molecule, the lower the material quality. During the production process, PE molecules polymerize, forming long chains. When the plastic cools and crystallises, highly branched molecules fit together less efficiently than linear ones. As a result, more branched structures like LDPE have lower strength and durability compared to the linear structure of HDPE. The lower crystallinity and strength of LDPE make it less suitable for high-impact or heavy-duty uses compared to HDPE. Therefore, this section focuses on the properties of HDPE, which is more suitable for the demanding requirements of floating barriers.[31][15][73]

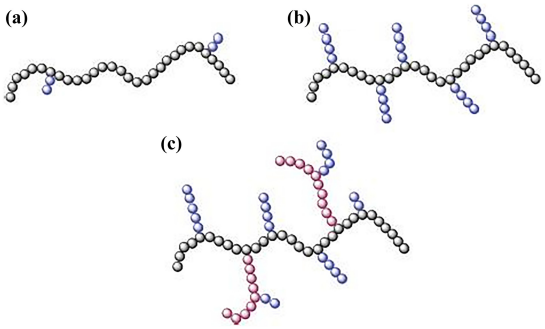

Figure E.3: Schematics of HDPE (a), LLDPE (b), and LDPE (c).[31]

Application of HDPP on floating barriers

The low density (0.94–0.97 $\mathrm{g/cm^3}$) of HDPE ensures buoyancy, a critical feature for floating barriers. This is particularly important in marine environments where the barrier must stay afloat while withstanding various forces from

waves and currents. It is used for the buoys in Type II barriers and for the floating tubes in Type III barriers.

The higher crystallinity of HDPE provides excellent tensile strength (27.04 MPa for new HDPE and 16.058 MPa for recycled HDPE)[78], making it robust enough to endure the physical challenges encountered in marine settings. Its impact resistance (20 J/m for stabilised HDPE)[47] also ensures that the material can handle collisions with debris or high water forces without cracking or breaking.

UV-resistance

While HDPE can be UV stabilised, untreated PE degrades when exposed to high UV levels. This degradation leads to brittleness and potential failure in environments with a high UV index, such as Puerto Morelos. To mitigate this, UV stabilizers or coatings must be added during production. This process typically involves integrating additives such as carbon black or UV inhibitors, which can significantly prolong the material's lifespan.[6][76][62] Despite the increased initial cost, incorporating UV stabilizers is essential for ensuring the long-term durability of HDPE in outdoor marine applications.

E.4. Polyvinyl Chloride

Polyvinyl Chloride (PVC) is a versatile, widely-used thermoplastic with applications in various industries. As seen in Figure E.4, the polymer is composed of repeating vinyl groups, with one hydrogen atom replaced by chlorine on alternate carbon atoms. This addition of chlorine grants PVC its unique properties, including durability, chemical resistance, and cost-effectiveness, making it especially suitable for construction and industrial uses. PVC is available in both rigid and flexible forms, which allows it to be tailored to specific applications, including the construction of floating barriers.

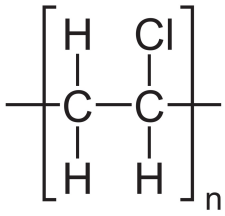

Figure E.4: Molecule structure of PVC.

PVC is often divided into two main categories: unmodified PVC (uPVC) and plasticised PVC, (pPVC). uPVC is used in structural applications due to its strength and resistance to deformation, while pPVC is more elastic and suited for uses requiring flexibility, such as hoses, cable installation and nets.

Application of PVC on floating barriers

PVC has a density range of 1.3–1.7 g/cm^3, making it heavier than water, and unlike materials like HDPE, discussed in Section E.3, it requires additional design considerations to float. Its ability to resist chemical degradation is important for its uses in floating barriers.[7] PVC is mainly used for the mesh grids, but also for the cushions in barrier types I and IV.

uPVC

PVC exhibits excellent tensile strength and rigidity, particularly in its unplasticised (uPVC) form, making it suitable for applications requiring structural integrity under stress. Its impact resistance is comparable to HDPE, and its hardness makes it more resistant to wear and abrasion.[7] However, its higher density compared to HDPE necessitates additional design considerations to ensure flotation. In marine conditions, both materials require additional foam logs to remain afloat, as neither can maintain buoyancy solely on their own.

pPVC

In mesh grids, ropes and rope protection tubes, the flexibility of pPVC makes it an ideal choice of material. pPVC is able to bend and adapt to dynamic wave forces without breaking or losing its integrity, where rigid materials might crack or fail under constant stress. Due to its chemical resistance, the pPVC does not degrade in the presence of saltwater and maintains its chemical properties. Even in the event of a rupture of the mesh grid, pPVC can be easily repaired on-site through thermal welding. which allows damaged sections of the mesh grid to be fused back together. This repair method is both time-efficient and cost-effective.

Using pPVC is an excellent choice for the construction of buoyant cushions used in barriers Type I. Its flexibility is a key advantage, allowing the cushions to be formed around foam logs and bend and adapt to the wave movements. This elasticity also provides easy handling during deployment and maintenance. For Type IV barriers, air-filled pPVC is recommended, as it can conform to the barrier's shape when inflated while being easily compacted for storage when not in use.

UV resistance

While PVC is more resistant to UV degradation than untreated PE, it can still discolour and become brittle over time when exposed to prolonged UV radiation. UV absorbers and stabilizers are strongly recommended in the PVC compound formulations.[72] UV stabilizers, such as the incorporation of certain additives, are necessary to enhance PVC's longevity in outdoor applications. Examples are Cadmium stabilizers (forbidden in the EU), Lead stabilizers, Orgotin stabilizers and Calcium/zinc stabilizers. When properly treated, PVC can perform well in high-UV environments of Puerto Morelos.[7][14]

E.5. Galvanised steel

In barrier types I, II, and III, galvanised steel components such as cables, chains, and shackles are used as ballast and connection points. These metal parts play a critical role in determining the overall strength and load-bearing capacity of the barrier. While the polymeric materials used in the barriers are resistant to seawater corrosion, the metals are not. Therefore, the long-term durability of the barrier depends heavily on the corrosion protection of these metallic components

Although the steel cables, chains, and shackles are encased in flexible PVC hoses to reduce exposure to seawater, they are not completely isolated from the marine environment. This incomplete isolation necessitates additional protective measures, as corrosion can significantly weaken the steel, reducing the strength and lifespan of the barrier. Without adequate corrosion protection, the mechanical integrity of the barrier is compromised, leading to potential failure under the heavy marine conditions

Saltwater corrosion

Carbon-steel is the most common used steel, consisting of Iron (Fe) alloyed with up to 1% carbon. Other metals can be added to improve certain properties, however, particulary, accelerates the oxidation process.[29]

The electrochemical nature of seawater corrosion is driven by redox reactions, where iron undergoes oxidation in the presence of oxygen and water. The half-reactions Equation E.1 and Equation E.2 combine to form the overall oxidation reaction in Equation E.3. [77] These reactions lead to the formation of rust, which is the hydrated form of iron oxide, as shown in Equation E.4 and Equation E.5.

$$\text{Fe (s)} \rightarrow \text{Fe}^{2+}(aq) + 2e^- \tag{E.1}$$

$$\text{O}_2(g) + 2\text{H}_2\text{O}(l) + 4e^- \rightarrow 4\text{OH}^-(aq) \tag{E.2}$$

$$2\text{Fe (s)} + \text{O}_2(g) + 2\text{H}_2\text{O}(l) \rightarrow 2\text{Fe(OH)}_2(s) \tag{E.3}$$

$$4\text{Fe(OH)}_2(s) + \text{O}_2(g) + 2\text{H}_2\text{O}(l) \rightarrow 4\text{Fe(OH)}_3(s) \tag{E.4}$$

$$\text{Fe(OH)}_3(s) \rightarrow \text{Fe}_2\text{O}_3 \cdot n\text{H}_2\text{O} \tag{E.5}$$

The resulting corrosion products, mainly rust, not only degrade the surface of the material, but also weaken the structural integrity of the barrier over time. As corrosion progresses, the material loses its ability to bear mechanical loads, increasing the risk of failure in critical marine applications. Therefore, protecting these steel components from continuous exposure to the harsh marine environment is essential.

Corrosion prevention strategies

To prevent corrosion and ensure the longevity of steel components in saltwater, three primary strategies can be employed:

1. Stainless steel is an alloy that contains at least 10.5% chromium (Cr), which forms a passive oxide layer on the surface, providing protection against corrosion. This material is highly resistant to saltwater corrosion but is typically more expensive due to the high cost of raw materials and the complex manufacturing process.[28]
2. Other metals, such as titanium or aluminium, can offer corrosion resistance in marine environments. However, like stainless steel, these metals tend to be expensive, making them less viable for cost-effective solutions in large-scale applications.
3. The most widely used solution for protecting steel in marine environments is galvanisation. By coating steel with a layer of zinc, the material becomes resistant to corrosion while maintaining a reasonable cost. Galvanisation is a cost-effective solution for protecting the material while preserving the strength of the material.

Galvanisation

Galvanised steel is steel that has been coated with a layer of zinc to protect it from corrosion. The process of galvanisation typically involves covering the steel with zinc. This zinc layer serves as a barrier to prevent moisture, oxygen, and other environmental factors from causing rust and corrosion. Even if the surface of the galvanised steel gets scratched, the zinc can still provide protection through a process called ”galvanic protection,” where the zinc corrodes in place of the steel.[75] There are two primary methods of galvanizing steel. First, Hot-Dip Galvanisation is the most common and cost-effective galvanisation process, where steel is submerged in molten zinc. The zinc bonds with the steel to form a thick, durable coating. Hot-dip galvanisation provides excellent protection in harsh environments.[65] the second method is called electrogalvanisation. In this method, an electrochemical process is used to apply a thin layer of zinc to the steel. While electrogalvanisation results in a more uniform and thin finish, it is more expensive and offers less protection compared to hot-dip galvanisation. This makes it it less suitable usage in barrier heavily exposed to seawater.[43]

Closed rusty seawater (CRS)

In sargassum barrier designs, the galvanised steel cables and chains are often enclosed in PVC to reduce direct exposure to seawater. However, it is not completely isolated from its surroundings, allowing seawater to penetrate and create a closed rusty seawater (CRS) environment around the steel as shown in Figure E.5. This is particularly concerning, as the CRS environment accelerates corrosion due to the presence of chloride ions and limited oxygen. In a CRS environment, this rust layer can significantly accelerate the pitting corrosion of galvanised steel. The zinc coating, designed to protect the steel, is compromised by rust, and pitting corrosion occurs under the influence of chloride ions. The accelerated corrosion in CRS can compromise the strength and durability of the cables and chains, making it critical to consider additional protective measures to maintain barrier integrity in long-term marine applications.[44]

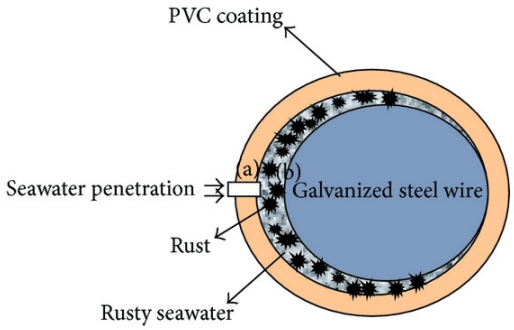

Figure E.5: Schematic diagram of a galvanised steel cable coated by PVC.[44]

E.6. Contact angle

The contact angle, denoted by α, β, and γ in Figure E.6, is a measure of the wettability of a surface. The contact angle is determined by the balance of cohesive forces (within the liquid) and adhesive forces (between the liquid and the solid surface).

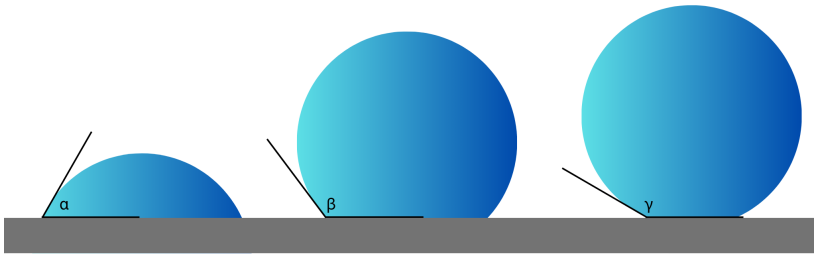

Figure E.6: Contact angle for hydrophilic surface (contact angle <90°) (left), hydrophobic surface (contact angle >90°) (middle) and superhydrophobic surface (contact angle >150°) (right).

- Hydrophilic surface: When the contact angle is lower than 90°), the surface is considered hydrophilic. This means that the liquid spreads out over the surface, indicating strong adhesive forces between the liquid and the surface.
- Hydrophobic surface: A contact angle of 90° indicates a hydrophobic surface. Here, the water forms a more defined droplet shape, as the adhesive forces between the surface and the liquid are weaker than the cohesive forces within the liquid.

- Superhydrophobic surface: When the contact angle exceeds 150°, the surface is considered superhydrophobic. In this case, the water droplet beads up into nearly a perfect sphere and easily rolls off the surface. Superhydrophobicity is achieved through nanoscale surface structures combined with low surface energy and is

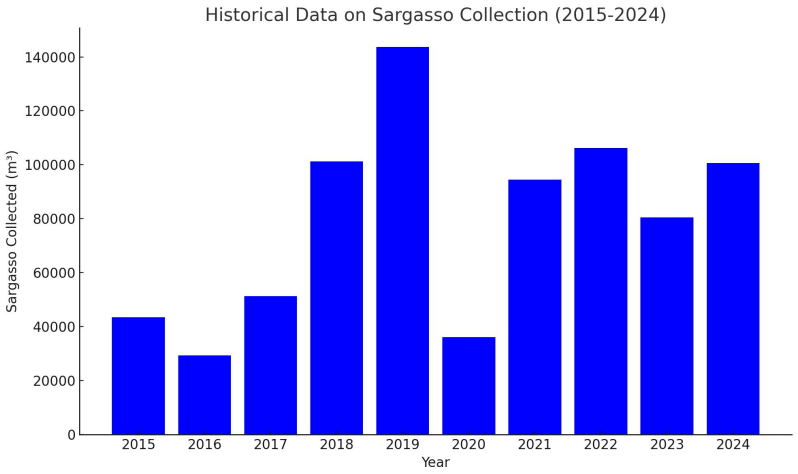

Figure E.7: Annual sargasso arrivals of sargassum at Moon Palace (until 01-08-2024).[50]

F
Wave and amplitude spectrum

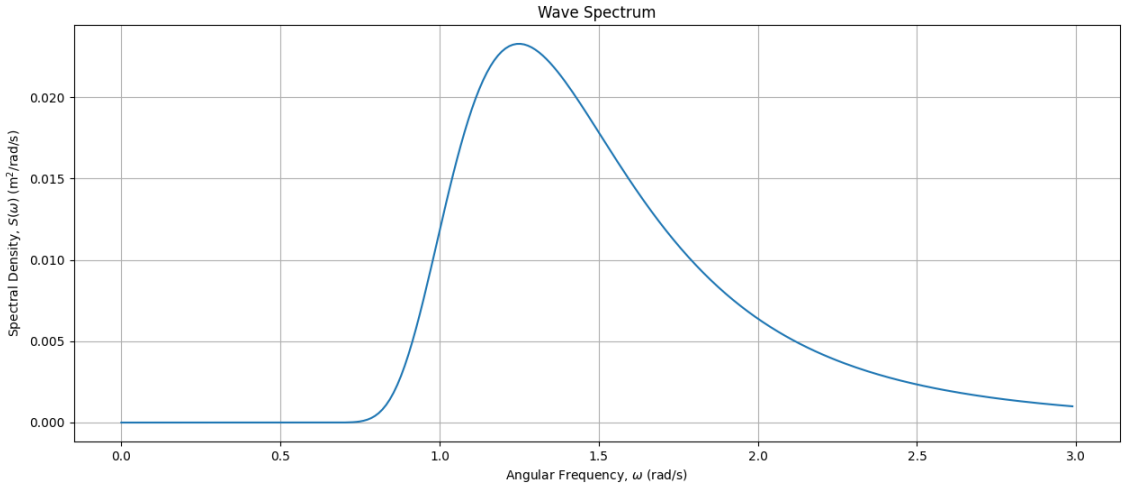

Figure F.1: Wave spectrum; input parameters: $H_s = 0.57$ m, $T_p = 5.03$ s.

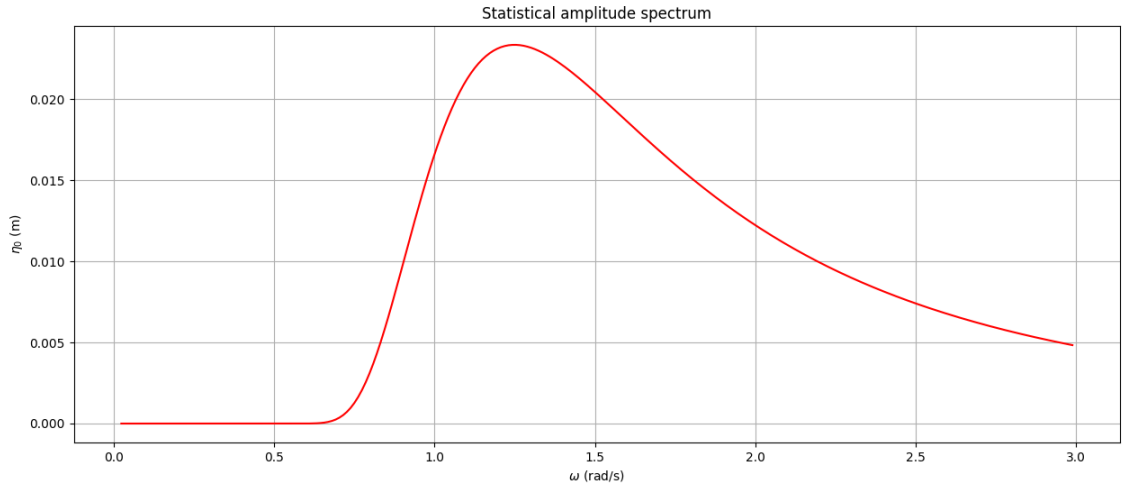

Figure F.2: Statistical amplitude spectrum, iseed used for randomness = 123.

G
Force determination

G.1. Wave elevation time series

Based on the wave spectrum generated from T_p and H_s, and the equations presented in Chapter 5, a time series of the wave velocity can be constructed. This is illustrated in Figure G.1.

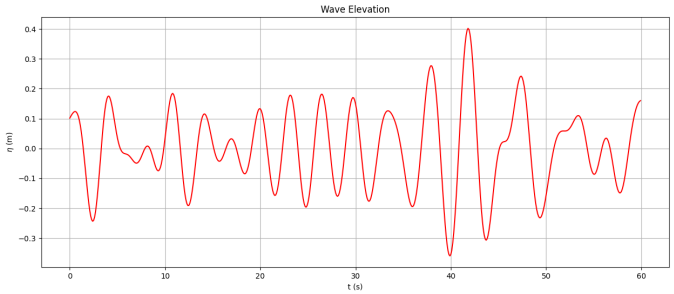

Figure G.1: Wave elevation η based on Appendix F.

G.2. Wave speed time series

Using the equations for particle velocity as described in Chapter 5, a time series for the wave particle velocity can be generated as well. As stated earlier, it is important that only the horizontal direction will be considered. Therefore, only the u_x is plotted. This is shown in Figure G.2.

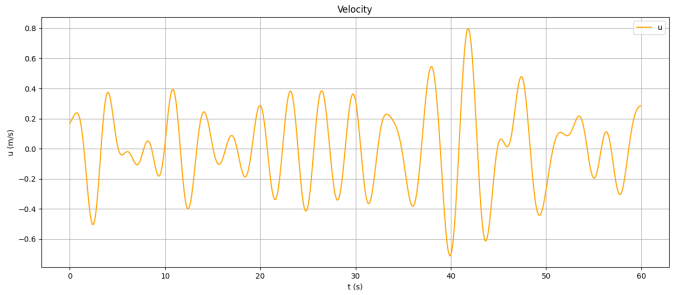

Figure G.2: Wave velocity u_x based on Appendix F.

G.3. Wave acceleration time series

The wave particle accelerations can be generated by taking the derivative of the velocity of the particles. This results in a wave particle accelerations time series as depicted in Figure G.3. Again, only the horizontal accelerations are plotted.

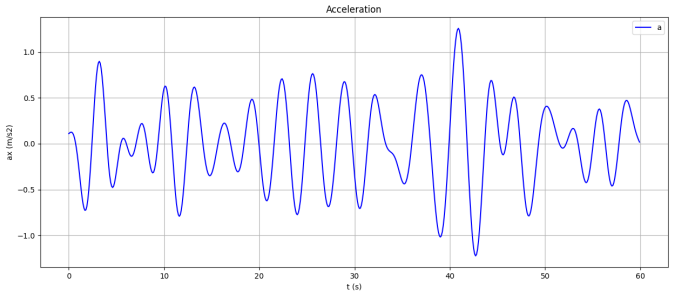

Figure G.3: Wave accelerations a_x based on Appendix F.

H
Mass matrix derivation

Here the derivation of the mass matrix is given for an element. The element has two degrees of freedom (DOFs) per node: one in the longitudinal direction (u) and one in the transverse direction (v).

H.1. Governing Equations

First, the governing equations are repeated that describe the behaviour of the string.

H.1.1. Longitudinal behaviour

The equation governing the axial deformation of a rod is given by:

$$\rho A \frac{\partial^2 u}{\partial t^2} + C_u \frac{\partial u}{\partial t} - \frac{\partial}{\partial x}\left(EA \frac{\partial u}{\partial x}\right) = f_u(x,t) \tag{H.1}$$

H.1.2. Transverse behaviour

The transverse motion of the element is governed by:

$$\rho A \frac{\partial^2 v}{\partial t^2} + C_v \frac{\partial u}{\partial t} - T \frac{\partial^2 v}{\partial x^2} = f_v(x,t) \tag{H.2}$$

H.2. Weak Form of the Governing Equations

The governing equations are then rewritten in their weak form by multiplying by test functions $w_u(x)$ and $w_v(x)$ and integrating over the element.

H.2.1. Longitudinal weak form

$$\int_0^{L_e} \rho A \frac{\partial^2 u}{\partial t^2} w_u(x)\, dx + \int_0^{L_e} C_u \frac{\partial u}{\partial t} w_u(x)\, dx + \int_0^{L_e} EA \frac{\partial u}{\partial x}\frac{\partial w_u}{\partial x}\, dx = \int_0^{L_e} f_u(x,t) w_u(x)\, dx \tag{H.3}$$

H.2.2. Transverse weak form

$$\int_0^{L_e} \rho A \frac{\partial^2 v}{\partial t^2} w_v(x)\, dx + \int_0^{L_e} C_v \frac{\partial v}{\partial t} w_v(x)\, dx + \int_0^{L_e} T \frac{\partial v}{\partial x}\frac{\partial w_v}{\partial x}\, dx = \int_0^{L_e} f_v(x,t) w_v(x)\, dx \tag{H.4}$$

H.3. Finite Element Discretization

Next, with the use of linear shape functions both the longitudinal and transverse displacement fields are discretized. For the 1D elements, the longitudinal and transverse displacements $u(x,t)$ and $v(x,t)$ at any point within the element are interpolated using shape functions $N_1(x)$ and $N_2(x)$, where each shape function corresponds to a specific node in the element. $u(x,t)$ and $v(x,t)$ are in this way discretized as:

$$u(x,t) = N_1(x)u_i(t) + N_2(x)u_{i+1}(t) \tag{H.5}$$

$$v(x,t) = N_1(x)v_i(t) + N_2(x)v_{i+1}(t) \tag{H.6}$$

with:

$$N_1(x) = \frac{x_{i+1} - x}{x_{i+1} - x_i} \tag{H.7}$$

$$N_2(x) = \frac{x - x_i}{x_{i+1} - x_i} \tag{H.8}$$

Here $N_1(x)$ and $N_2(x)$ are the linear shape functions corresponding to node i and $i+1$ respectively, and $u_i(t), v_i(t)$ and $u_{i+1}(t), v_{i+1}(t)$ are the longitudinal and transverse displacements at these nodes.

H.4. Element Matrices

H.4.1. Longitudinal Mass Matrix

The mass matrix for the longitudinal behavior, accounting for the inertia, is derived as follows:

$$m_u^{(e)} = \int_{x_i}^{x_{i+1}} \rho A N^T N \, dx \tag{H.9}$$

This yields the elemental longitudinal mass matrix:

$$m_u^{(e)} = \frac{\rho A \Delta x}{6} \begin{bmatrix} 2 & 1 \\ 1 & 2 \end{bmatrix} \tag{H.10}$$

H.4.2. Transverse Mass Matrix

Similarly, the mass matrix for the transverse behaviour is given by:

$$m_v^{(e)} = \int_{x_i}^{x_{i+1}} \rho A N^T N \, dx \tag{H.11}$$

This results in the elemental transverse mass matrix:

$$m_v^{(e)} = \frac{\rho A \Delta x}{6} \begin{bmatrix} 2 & 1 \\ 1 & 2 \end{bmatrix} \tag{H.12}$$

H.5. Combined Element Matrices

Finally, the longitudinal and transverse matrix are combined into a single element matrix by accounting for the two degrees of freedom per node (longitudinal u and transverse v).
The degrees of freedom vector for each element is:

$$\mathbf{U}_e = \begin{bmatrix} u_i \\ v_i \\ u_{i+1} \\ v_{i+1} \end{bmatrix} \tag{H.13}$$

H.5.1. Combined Element Mass Matrix

The combined mass matrix for the element is written as:

$$M_e = \begin{bmatrix} m_u^{(e)} & 0 \\ 0 & m_v^{(e)} \end{bmatrix} \tag{H.14}$$

Substituting the individual mass matrices gives:

$$M_e = \frac{\Delta x}{6} \begin{bmatrix} 2\rho A & 0 & \rho A & 0 \\ 0 & 2\rho A & 0 & \rho A \\ \rho A & 0 & 2\rho A & 0 \\ 0 & \rho A & 0 & 2\rho A \end{bmatrix} \tag{H.15}$$

Eventually, this derived mass matrix is ready to be assembled into the global system of equations for further analysis.